

UCLA

UCLA Electronic Theses and Dissertations

Title

Development of Validated Omni-directional Models for Triple Friction Pendulum Bearings in Support of Performance-Based Seismic Engineering

Permalink

<https://escholarship.org/uc/item/5qf057d1>

Author

Mao, Henan

Publication Date

2021

Peer reviewed|Thesis/dissertation

UNIVERSITY OF CALIFORNIA

Los Angeles

Development of Validated Omni-directional Models for
Triple Friction Pendulum Bearings in Support of
Performance-Based Seismic Engineering

A dissertation submitted in partial satisfaction
of the requirements for the degree
Doctor of Philosophy in Civil and Environmental Engineering

by

Henan Mao

2021

© Copyright by

Henan Mao

2021

ABSTRACT OF THE DISSERTATION

Development of Validated Omni-directional Models for
Triple Friction Pendulum Bearings in Support of
Performance-Based Seismic Engineering

by

Henan Mao

Doctor of Philosophy in Civil and Environmental Engineering

University of California, Los Angeles, 2021

Professor Ertugrul Taciroglu, Chair

Seismic isolation systems are becoming more common in the construction of a variety of critical buildings/facilities, such as hospitals and data centers, that require more stringent seismic performance levels. The Triple Friction Pendulum (TFP) isolation bearing systems offer arguably the highest performance among seismic hazard mitigation devices/solutions. TFP bearings, which exhibit highly nonlinear and history-dependent responses, dissipate the seismic energy through friction. While there are numerous models available to simulate the cyclic responses of TFP bearings, most either lack several key features, such as coupled biaxial or triaxial reactions or account for these effects in a phenomenological manner. The present study tackles these issues by implementing a physics-based, extendable, and numerically robust model, which is packaged into a novel macroelement that can be used in nonlinear time-history analyses that are required for performance-based seismic assessment and design.

The aforementioned macroelement model is based on a mechanically consistent multi-

surface plasticity approach that can simulate the triaxial hysteretic responses of TFP bearings. The macroelement model is developed and implemented in ABAQUS as a User-defined Element (UEL). It is validated using experimental data from component-scale laboratory and full-scale shake table tests carried out at the E-Defense facility.

The experimentally validated biaxial and triaxial TFP models are then used in performance-based seismic assessment of a prototypical base-isolated braced frame building to examine the effects of modeling errors on the estimated seismic losses. While the scope of this case study was limited to one building, findings indicated that differences between the basic (i.e., uncoupled biaxial) and the more advanced (i.e., coupled biaxial and triaxial) approaches are non-negligible, warranting their use in practice as well as future studies.

The dissertation of Henan Mao is approved.

Huseyin Tekin Darama

Keri Ryan

Jian Zhang

Scott Joseph Brandenburg

Ertugrul Taciroglu, Committee Chair

University of California, Los Angeles

2021

*To my family ...
who always support me*

TABLE OF CONTENTS

1	Introduction	1
1.1	What is a Base Isolation System?	1
1.2	A Brief History of Base Isolation Systems	1
1.3	Classification of Isolators	2
1.3.1	Elastomeric Rubber Bearings	2
1.3.2	Roller and Ball Bearings	3
1.3.3	Steel Spring Bearings	3
1.3.4	Friction Pendulum Bearings	3
1.4	Contemporary Application Examples of Seismic Base Isolation	5
1.5	Benefits of Base Isolation	7
1.5.1	Reduced Seismic Demand	7
1.5.2	Reduced Damage	7
1.5.3	Improved Life-safety	8
1.5.4	Positive Cost-benefit Outcomes	8
1.6	Basics of Bearing Design	9
1.6.1	Design Process	9
1.6.2	ASCE 7 Equivalent Lateral Force Procedure (ELF)	11
2	Triple Friction Pendulum Bearings	15
2.1	Uniaxial Behavior of a TFP Bearing	15
2.2	Biaxial Behavior of a TFP Bearing	18

3	Three-dimensional Finite Element Modeling of TFP Bearing Devices . . .	22
3.1	Modeling the Geometry of TFP Bearings	22
3.2	Meshing Process and Element Types	23
3.3	Contact Modeling, Boundary and Loading Conditions	26
3.4	The Solution Methods	27
3.5	Validating the Continuum Finite Element Model	27
4	An Omnidirectional Modeling Approach for Hysteretic Response of TFP Bearings	32
4.1	Implicit Algorithm for Multi-surface Plasticity	33
4.2	Mroz’s Translation Rule	34
4.3	ABAQUS User-defined Element (UEL) Implementation	41
4.4	ABAQUS User-defined Element (UEL) Validation	41
4.4.1	Unidirectional Sine Wave Displacement Orbit	45
4.4.2	Circular Displacement Orbit	45
4.4.3	Eight-Shaped Displacement Orbit	45
4.4.4	Square-Shaped Displacement Orbit	45
4.4.5	Uncontrolled Displacement Orbit	49
4.5	An Application of the Omnidirectional Model: Dynamic Analysis of a Prototype Base-Isolated Building.	49
4.5.1	The Prototype Building Geometry and Loads	52
4.5.2	Ground Motion Selection	53
4.5.3	Design of the TFP Bearings	53
4.5.4	Dynamic Analysis Results	54

5 A Pressure-dependent Macroelement Modeling Approach for Hysteretic Response of TFP Bearings	62
5.1 The Methodology of the Pressure-dependent Macroelement Model	62
5.2 Validation of the Pressure-dependent Macroelement model	63
5.2.1 Single Element Test	67
5.2.2 E-Defense Building Test	76
6 Fragility-based Seismic Performance Assessment of the E-Defense Building	90
6.1 Ground Motion Selection	93
6.2 The Effect of Earthquake Orientation	93
6.3 Intensity Measure (IM) Selection & Damage Fragility Curves	95
7 Conclusions & Future Work	104
7.1 Chapter-by-chapter Summaries and Conclusions	104
7.2 Recommended Future Work	106
A The TFP Bearing Response under Earthquakes Described in Table 4.3	107
B The Vertical Response Spectra of the Building under 3D Earthquake Excitations	114
C The Hysteresis of TFP Bearings, the Peak Inter-story Drift Ratio and the Maximum Floor Acceleration of E-Defense Building under Earthquakes. .	125
D The Distribution of the Peak Floor Accelerations and the Inter-story Drift Ratio for Three Models.	135

E Regression Analyses of PSDM	140
References	149

LIST OF FIGURES

1.1	Elastomeric rubber bearings [17]	3
1.2	Roller and ball bearings [90]	4
1.3	Steel spring bearings [18]	4
1.4	Friction pendulum bearings [89]	5
1.5	Apple Park, Cupertino, California [101].	6
1.6	Sabiha Gokcen International Airport, Turkey [88].	6
1.7	Pasadena City Hall, California [101].	7
1.8	Keck Hospital of USC, Los Angeles, California, sits on 149 base isolators. Almost no damage was found on the main structure or the nonstructural components during the 1994 Northridge Earthquake [65].	9
2.1	Single Friction Pendulum [30]	16
2.2	Triple Friction Pendulum Bearing section view and basic parameters.	16
2.3	Uniaxial behavior of the TFP bearing ($\mu_1 = \mu_2, L_1 = L_2$)	18
2.4	Series spring model for multi-stage behavior of TFP bearing [23].	19
2.5	Modified series spring model for multi-stage behavior of a TFP bearing [23].	20
2.6	Flow chart for solving TFP bearing element [23].	21
3.1	The ABAQUS TFP bearing model geometry.	23
3.2	Eight-node brick element.	24
3.3	Partition (a) and meshing (b) of the TFP bearing.	25
3.4	Boundary and loading conditions.	26
3.5	Rigid block setup at the UC Berkeley PEER earthquake simulator laboratory [5].	28

3.6	Isolator displacement time-history under sine waves (a), hysteresis of the isolator in experiment results (b) [5] and ABAQUS finite element analysis results (c).	29
3.7	Isolator circular displacement orbit (a), hysteresis of the isolator in experiment results (b)(c) [5], and ABAQUS finite element analysis results (d)(e).	31
4.1	The Mroz's translation rules for multisurface plasticity	34
4.2	Flowchart of multi-surface plasticity model	40
4.3	The uniaxial behavior of multisurface plasticity models under sine wave (a) using Mroz's translation rule (b).	42
4.4	The simplified omnidirectional model.	44
4.5	Isolator displacement time-history (a), hysteresis (b), and energy dissipation (c).	46
4.6	TFP bearings hysteresis for the circular displacement orbit.	47
4.7	TFP bearings hysteresis for the eight-shaped displacement orbit.	48
4.8	TFP bearings hysteresis for the square-shaped displacement orbit.	50
4.9	TFP bearings displacement history, orbit and hysteresis from response to the Kobe @ JMA earthquake record.	51
4.10	3D view of the ABAQUS model.	52
4.11	Acceleration response spectrum curves for MCE scenario earthquake records: Fault Normal (a), Fault Parallel (b).	54
4.12	The TFP backbone curve and the omnidirectional model.	55
4.13	Displacement orbit of Chi-Chi @ TCU076 earthquake (a), energy dissipation (b) and hysteresis of the TFP bearings (c)(d).	57
4.14	Max. normalized base shear under Chi-Chi @ TCU076 earthquakes with different orientations of the unidirectional model and the omnidirectional model.	60
5.1	The pressure-dependent macroelement model.	64

5.2	The cone shape yielding surfaces of the pressure-dependent macroelement model.	65
5.3	The hysteresis of TFP bearings under sine wave.	68
5.4	The hysteresis of TFP bearings under Imperial Valley @ Westmorland earthquake.	69
5.5	The hysteresis of TFP bearings under Northridge @ Sylmar earthquake.	70
5.6	The hysteresis of TFP bearings under Loma Prieta @ Los Gatos Pres. Ctr. earthquake.	71
5.7	The hysteresis of TFP bearings under Tohoku @ Iwanuma earthquake.	72
5.8	The hysteresis of TFP bearings under Kobe @ Takatori earthquake.	73
5.9	The hysteresis of TFP bearings under Chi-Chi @ TCU065 earthquake.	74
5.10	The hysteresis of TFP bearings under Tabas @ Tabas earthquake.	75
5.11	The finite element model of E-Defense building.	77
5.12	The first 3 modes shape and period of the E-Defense building.	78
5.13	The hysteresis of TFP bearings under sine wave.	79
5.14	The peak inner-story drift ratio of E-Defense building under sine wave.	80
5.15	The peak floor acceleration of E-Defense building under sine wave.	81
5.16	The hysteresis of TFP bearings under Kobe @ Takatori earthquake.	82
5.17	The peak inner-story drift ratio of E-Defense building under Kobe @ Takatori earthquake.	82
5.18	The peak floor acceleration of E-Defense building under Kobe @ Takatori earth- quake.	83
5.19	The southwest TFP bearings normalized base shear v.s. displacement under Kobe @ Takatori earthquake in E-Defense experiment.	84
5.20	The horizontal response spectra of the building under Kobe @ Takatori earth- quake (Northwest).	85

5.21	The horizontal response spectra of the building under Kobe @ Takatori earthquake (Southeast).	85
5.22	The vertical response spectra of the building under Kobe @ Takatori earthquake (Northwest).	86
5.23	The vertical response spectra of the building under Kobe @ Takatori earthquake (Northeast).	87
5.24	The vertical response spectra of the building under Kobe @ Takatori earthquake (Southeast).	88
6.1	5% damped acceleration response spectra of the selected records (2475 years) [105].	94
6.2	The distribution of the peak floor accelerations (a), and inter-story drift ratio (b) for three models under the Chuetsu-Oki @ Kashiwazaki City Center earthquake with different earthquake orientations.	95
6.3	The distribution of the peak floor accelerations (a) and inter-story drift ratio (b) for three models under Landers @ North Palm Springs Fire Sta #36 earthquake with different earthquake orientations.	96
6.4	The average and standard deviation of the peak floor accelerations (a), and inter-story drift ratio (b) for three models.	98
6.5	Fragility functions for slight, moderate, extensive, and complete damage (EDP=FPA).	99
6.6	Fragility functions for slight, moderate, extensive, and complete damage (EDP=IDR).	100
6.7	Fragility functions for slight, moderate, extensive, and complete damage (EDP=FPA).	101
6.8	Fragility functions for slight, moderate, extensive, and complete damage (EDP=PFA).	102
6.9	Expected total repair cost (%).	103
A.1	Displacement orbit of Darfield @ GDLC earthquake (a), energy dissipation (b) and hysteresis of the TFP bearings (c)(d).	108

A.2	Displacement orbit of Duzce @ Duzce earthquake (a), energy dissipation (b) and hysteresis of the TFP bearings (c)(d).	109
A.3	Displacement orbit of Imperial Valley @ Delta earthquake (a), energy dissipation (b) and hysteresis of the TFP bearings (c)(d).	110
A.4	Displacement orbit of Kobe @ Abeno earthquake (a), energy dissipation (b) and hysteresis of the TFP bearings (c)(d).	111
A.5	Displacement orbit of Landers @ Yermo Fire Station earthquake (a), energy dissipation (b) and hysteresis of the TFP bearings (c)(d).	112
A.6	Displacement orbit of Superstition Hills @ EI Centro earthquake (a), energy dissipation (b) and hysteresis of the TFP bearings (c)(d).	113
B.1	The horizontal response spectra of the building under Loma Prieta @ Los Gatos Pres. Ctr. earthquake (Northwest).	115
B.2	The horizontal response spectra of the building under Loma Prieta @ Los Gatos Pres. Ctr. earthquake (Southeast).	115
B.3	The vertical response spectra of the building under Loma Prieta @ Los Gatos Pres. Ctr. earthquake (Northwest).	116
B.4	The vertical response spectra of the building under Loma Prieta @ Los Gatos Pres. Ctr. earthquake (Northeast).	117
B.5	The vertical response spectra of the building under Loma Prieta @ Los Gatos Pres. Ctr. earthquake (Southeast).	118
B.6	The horizontal response spectra of the building under Imperial Valley @ Westmorland earthquake (Northwest).	118
B.7	The horizontal response spectra of the building under Imperial Valley @ Westmorland earthquake (Southeast).	119

B.8	The vertical response spectra of the building under Imperial Valley @ Westmorland earthquake (Northwest).	119
B.9	The vertical response spectra of the building under Imperial Valley @ Westmorland earthquake (Northeast).	120
B.10	The vertical response spectra of the building under Imperial Valley @ Westmorland earthquake (Southeast).	121
B.11	The horizontal response spectra of the building under Kobe @ Takatori earthquake (Northwest).	121
B.12	The horizontal response spectra of the building under Kobe @ Takatori earthquake (Southeast).	122
B.13	The vertical response spectra of the building under Kobe @ Takatori earthquake (Northwest).	122
B.14	The vertical response spectra of the building under Kobe @ Takatori earthquake (Northeast).	123
B.15	The vertical response spectra of the building under Kobe @ Takatori earthquake (Southeast).	124
C.1	The hysteresis of TFP bearings under Imperial Valley @ Westmorland earthquake.	126
C.2	The peak inner-story drift ratio of E-Defense building under Imperial Valley @ Westmorland earthquake.	126
C.3	The peak floor acceleration of E-Defense building under Imperial Valley @ Westmorland earthquake.	127
C.4	The hysteresis of TFP bearings under Northridge @ Sylmar earthquake.	127
C.5	The peak inner-story drift ratio of E-Defense building under Northridge @ Sylmar earthquake.	128

C.6	The peak floor acceleration of E-Defense building under Northridge @ Sylmar earthquake.	128
C.7	The hysteresis of TFP bearings under Loma Prieta @ Los Gatos Pres. Ctr. earthquake.	129
C.8	The peak inner-story drift ratio of E-Defense building under Loma Prieta @ Los Gatos Pres. Ctr. earthquake.	129
C.9	The peak floor acceleration of E-Defense building under Loma Prieta @ Los Gatos Pres. Ctr. earthquake.	130
C.10	The hysteresis of TFP bearings under Tohoku @ Iwanuma earthquake.	130
C.11	The peak inner-story drift ratio of E-Defense building under Tohoku @ Iwanuma earthquake.	131
C.12	The peak floor acceleration of E-Defense building under Tohoku @ Iwanuma earthquake.	131
C.13	The hysteresis of TFP bearings under Tabas @ Tabas earthquake.	132
C.14	The peak inner-story drift ratio of E-Defense building under Tabas @ Tabas earthquake.	132
C.15	The peak floor acceleration of E-Defense building under Tabas @ Tabas earthquake.	133
C.16	The hysteresis of TFP bearings under Chi-Chi @ TCU065 earthquake.	133
C.17	The peak inner-story drift ratio of E-Defense building under Chi-Chi @ TCU065 earthquake.	134
C.18	The peak floor acceleration of E-Defense building under Chi-Chi @ TCU065 earthquake.	134
D.1	The distribution of the peak floor accelerations for three models under Chuetsu-Oki @ Yan Sakuramachi City watershed earthquake with different earthquake orientation.	136

D.2	The distribution of the inter-story drift ratio for three models under Chuetsu-Oki @ Yan Sakuramachi City watershed earthquake with different earthquake orientation.	137
D.3	The distribution of the peak floor accelerations for three models under Landers @ North Palm Springs Fire Sta #36 earthquake with difference earthquake orientation.	137
D.4	The distribution of the inter-story drift ratio for three models under Landers @ North Palm Springs Fire Sta #36 earthquake with difference earthquake orientation.	138
D.5	The distribution of the peak floor accelerations for three models.	138
D.6	The distribution of the inter-story drift ratio for three models.	139
E.1	Regression analyses of SaT1 v.s. PFA	141
E.2	Regression analyses of Sd v.s. PFA	142
E.3	Regression analyses of PGA v.s. PFA	143
E.4	Regression analyses of PGV v.s. PFA	144
E.5	Regression analyses of SaT1 v.s. IDR	145
E.6	Regression analyses of Sd v.s. IDR	146
E.7	Regression analyses of PGA v.s. IDR	147
E.8	Regression analyses of PGV v.s. IDR	148

LIST OF TABLES

3.1	Geometry of the TFP bearing used in the experimental test.	23
4.1	Discretization utilized for the uniaxial test.	42
4.2	Parameters calibrated from the uniaxial sine wave test.	44
4.3	The selected earthquake records.	53
4.4	The geometry parameter of the TFP bearing.	54
4.5	Max. normalized base shear under earthquake.	56
4.6	Max. story drift under earthquake.	58
4.7	Max. acceleration under earthquake.	59
4.8	Max. normalized base shear under earthquakes with different orientations of the uncoupled macroelement model.	61
5.1	Geometry of the TFP bearing used in the E-defense.	65
5.2	Input parameters of the pressure-dependent macroelement model.	66
5.3	Earthquake excitations applied to the E-defense building.	66
5.4	Estimated weight of the specimen by floor level.	76
5.5	modal analysis of the E-Defense building.	78
6.1	The variability in capacity β_C and the uncertainty in modeling β_M	92
6.2	The peak floor accelerations are used to define median values of the damage to non-structural acceleration-sensitive components.	92
6.3	The peak inter-story drifts ratio (%) are used to define median values of the damage to structural drift-sensitive components.	92

6.4	Max. difference of the peak floor accelerations, and inter-story drift ratio under different orientations of the earthquake excitations.	96
6.5	the proficiency ζ of different intensity measures for IDR.	97
6.6	the proficiency ζ of different intensity measures for PFA.	97

ACKNOWLEDGMENTS

I would like to express my sincere gratitude to my advisor, Professor Ertugrul Taciroglu, for his guidance, encouragement, and ingenuity. This dissertation would not have been possible without his steadfast support. I would like to thank Professors Scott J. Brandenburg, Jian Zhang, Keri Ryan, Jeff Eldredge, and Dr. Huseyin Darama for serving on my dissertation committee and their insightful comments. Special thanks to Professor Keri Ryan and Dr. Huseyin Darama for their countless assistance during my Ph.D. study.

I would like to thank Dr. Alp Karakoc, who taught me a lot when I started my Ph.D. research. I want to express my special thanks of gratitude to my colleges at UCLA—Dr. Wenyang Zhang, Prof. Pengyu Chen, Dr. Abdoul Ghotbi—who always provides help during my entire Ph.D. study.

Finally, I would like to thank my friend at UCLA—Prof. Elnaz Esmailzadeh Seylabi, Dr. Arastoo Dasmeh, Dr. Mehrdad Shokrabadi, Dr. Yuan Hu, Dr. Han Sun, Dr. Yu Zhang, Dr. Dong Wang, Dr. Yi Peng, Dr. Hua Kang, Dr. Xingquan Guan, Dr. Zhenxiang Yi, Dr. Jixing Cao, Dr. Peng Guo, Dr. Shiqi Dong, and many others—who have offered valuable help during my Ph.D. studies.

VITA

- 2011–2015 B.S. in Civil Engineering, Anhui Jianzhu University, Hefei, China
- 2015–2017 M.S. in Civil Engineering, University of California, Los Angeles, USA
- 2017–2021 Ph.D. Candidate in Civil Engineering, University of California,
Los Angeles, USA

PUBLICATIONS

Mao, H., H. Darama, and E. Taciroglu (2000). “A consistent omnidirectional nonlinear hysteretic response model for triple friction pendulum bearings.” *17th World Conference on Earthquake Engineering*, Sendai-JAPAN, Paper C000510.

CHAPTER 1

Introduction

1.1 What is a Base Isolation System?

Base isolation systems are among the most broadly employed method for reducing the damage caused by seismic hazards. This class of seismic hazard mitigation method provides better protection of the structure by separating the ground motions from the superstructure [49]. Many types of base isolation systems are widely used in essential facilities, such as hospitals [7], data centers [64], and transportation structures [99]. The following sections provide background material on their use and outline their application principles.

1.2 A Brief History of Base Isolation Systems

In the early 19th century, structural engineers developed a new concept called the “flexible first story” [52, 39, 32, 36]. In this approach, the first story columns are constructed to be more flexible than upper-level columns. However, since the horizontal stiffness of the first floor is too small, the column on the first floor experiences large displacements, which significantly lowers the critical buckling load of the column. As such, the concept was not widely utilized in real-life applications. In 1970, the first building using rubber bearings (a base isolation system) was built in Skopje, Yugoslavia. The rubber bearing concept began gaining recognition from then on, arguably because the requisite design procedure was fairly straightforward, and the construction procedures were not difficult. Compared to their conventional—i.e., fixed-base—counterparts, base-isolated buildings did perform

better under earthquakes. In the decade that followed, many researchers began characterizing and bracketing their behavior, as well as improving their constituent materials' performance [86, 97]. Tests conducted at the University of California, Berkeley, and field observations indicated solidified marketplace acceptance of base isolation devices. Around the 1970s, quite a few researchers were interested in improving the material performance of the rubber bearing. Early examples include experimental studies conducted on base isolation systems for seismically resilient power plants [41], as well as various studies carried out in New Zealand [85, 84, 83]. Eventually, the base isolation concept gained broad acceptance, and its application to high-way and railway bridges and buildings became commonplace.

1.3 Classification of Isolators

Currently, the most widely used isolators/bearings can be characterized into four major types—namely, elastomeric rubber, roller-and-ball, steel spring, and friction pendulum bearings.

1.3.1 Elastomeric Rubber Bearings

Elastomeric rubber bearings (Figure 1.1) are manufactured using horizontal layers of synthetic or natural rubber in thin layers that are bound between steel plates. The horizontal stiffness of this type of bearing is relatively small compared to its vertical stiffness. Thus the vertical deformation under the weight of the superstructure is relatively small. The damping ratio of the plain elastomeric bearings is approximately 5%, and if a lead core is embedded within the elastomeric bearing, the damping ratio increase to approximately 15%, significantly enhancing energy dissipation.

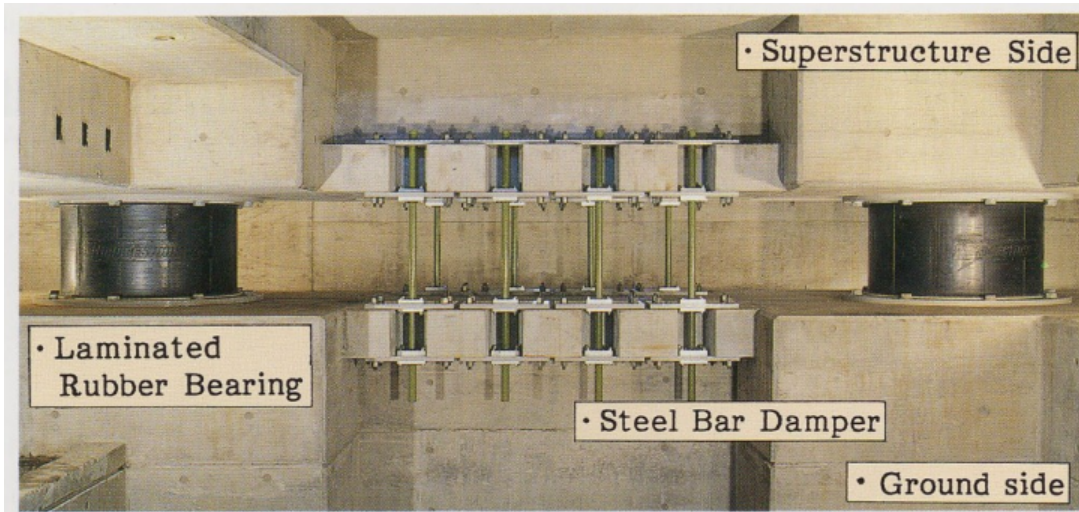


Figure 1.1: Elastomeric rubber bearings [17]

1.3.2 Roller and Ball Bearings

Roller and ball bearings (Figure 1.2) consist of cylindrical rollers and balls and are usually used for isolating the large machines in factories. Few buildings use this device because it is highly flexible in the horizontal direction; therefore, it cannot bear the large shear forces due to an entire building's inertia.

1.3.3 Steel Spring Bearings

Steel spring bearings (Figure 1.3) are widely used in mechanical engineering applications, e.g., in automobiles and industrial machines. They are flexible in the vertical direction and cannot restrict horizontal deformations, which renders them nominally unsuitable for civil engineering applications.

1.3.4 Friction Pendulum Bearings

Friction pendulum bearings (Figure 1.4) rely on friction to dissipate energy and are used in buildings as well as bridges. This type of device exhibits different tangent stiffness at different



Figure 1.2: Roller and ball bearings [90]



Figure 1.3: Steel spring bearings [18]

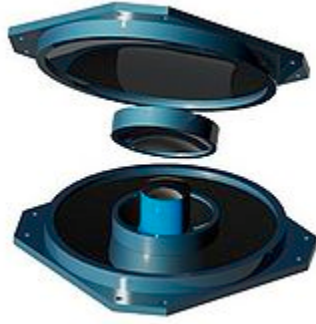


Figure 1.4: Friction pendulum bearings [89]

stages of loading. As it is the core subject matter of the present study, their attributes and behavior will be discussed in detail in the following chapter.

1.4 Contemporary Application Examples of Seismic Base Isolation

Base isolation systems have become a common solution in seismic design when higher performance requirements (e.g., continued functionality, immediate occupancy, etc.) need to be met. In such applications, isolators can significantly reduce the seismic demands and protect both the structure and its contents [50]. One of the well-known examples is the “Apple Park” shown in Figure 1.5. This ring-shaped building was design by Arup Inc, and rests on 700 friction pendulum bearings. The Sabiha Gokcen International Airport (Figure 1.6) completed in 2009, and the Pasadena City Hall (Figure 1.7) retrofitted in 2006 are recent examples of major based isolation applications, which respectively utilized 296 and 242 friction pendulum bearings in their construction.



Figure 1.5: Apple Park, Cupertino, California [101].



Figure 1.6: Sabiha Gokcen International Airport, Turkey [88].



Figure 1.7: Pasadena City Hall, California [101].

1.5 Benefits of Base Isolation

A base-isolated building offers numerous advantages over a conventional, fixed-based structure. These benefits are briefly reviewed in what follows.

1.5.1 Reduced Seismic Demand

The first period of a base-isolated structure is typically much longer than the corresponding fixed-base structure. Thus, it should be subject to smaller peak accelerations, if one uses a typical design spectrum to draw this conclusion. As a result, maximum shear forces that the superstructure will experience—and consequently, the peak drift ratios—will be reduced.

1.5.2 Reduced Damage

The peak acceleration transferred to a base-isolated superstructure is smaller than that to a fixed based one. Therefore, lower inertial forces will be induced in the superstructure. By

properly designing base isolators, the seismic demands on structural components can be completely confined to their linear elastic response ranges, or at least, the plastic deformations can be significantly reduced. This will enable achieving immediate occupancy performance objectives even for maximum considered earthquakes. The same effect will also reduce or completely eliminate nonstructural damage, ensuring continued functionality.

1.5.3 Improved Life-safety

Most of the injuries to the occupants are caused by nonstructural components. With base isolation, seismic demands on most nonstructural systems will be reduced, which, in turn, will improve the chances of the building's occupants during a major event. More importantly, base isolation will reduce the probability of structural collapse.

1.5.4 Positive Cost-benefit Outcomes

Base isolation systems bring additional costs, and if one only considers these initial costs, then base isolation systems may be deemed as being very expensive. However, there are many other factors that need to be taken into consideration. First, the insurance costs of a base-isolated building are (should be) nominally cheaper than a conventional building. Second, severe earthquakes can cause damage that a base-isolated building would avoid, and thus, repair, retrofit, and downtime-related costs will be avoided. Given these factors, the lifetime cost of a base-isolated building could actually be *significantly* lower than a conventional one.

As a historical example, the Keck Hospital of USC (Figure 1.8) remained fully functional and did not require any repairs after the 1994 Northridge Earthquake.



Figure 1.8: Keck Hospital of USC, Los Angeles, California, sits on 149 base isolators. Almost no damage was found on the main structure or the nonstructural components during the 1994 Northridge Earthquake [65].

1.6 Basics of Bearing Design

This section presents a brief introduction to the current typical engineering practice, which is based on ASCE provisions, for seismic analysis of base-isolated structures and basic steps for bearing design.

1.6.1 Design Process

- (1) Determine the building performance objectives for design:
 - a) Design of the superstructure for forces associated with the design earthquake, reduced by only a fraction of the factor permitted for the design of conventional, fixed-base buildings ($1 < R_I = 3/8R \leq 2.0$). The value of R_I (numerical coefficient related to the type of seismic force-resisting system above the isolation

system – similar to response modification factor) is permitted to be taken as greater than 2.0, provided the strength of the structure above the base level in the direction of interest, as determined by nonlinear static analysis at a roof displacement corresponding to a maximum story drift the lesser of the MCE_R drift or $0.015h_{sx}$, is not less than 1.1 times V_b . Where, V_b is total lateral seismic design force or shear on elements of the isolation system or elements below isolation system as prescribed ASCE 7-16 [2] Equation 17.5-5.

- b) Design of the isolation system and elements of the structure below the isolation system (i.e., the foundation) for unreduced design earthquake forces ($R_I = 1.0$).
 - c) Design and prototype testing of isolator units for forces (including effects of overturning) and displacements associated with the MCE_R .
 - d) Provision of sufficient separation between the isolated structure and surrounding retaining walls and other fixed obstructions to allow unrestricted movement during the MCE_R where MCE_R is risk targeted maximum considered earthquake (2,475 years return period event).
- (2) Perform Seismic Hazard Assessment by developing site-specific design response spectrum and spectrally matched earthquake records to be used in performance verification (nonlinear time history analysis).
- (3) Determine isolator type and properties.
- (4) Isolator procurement and prototype testing.
- (5) Analysis and performance verification.
- a) Equivalent Lateral Force Procedure: Preliminary analysis and basic building response parameters.
 - b) Response Spectrum Method: Form the basis of structural design and compliance with ASCE 7.

c) Nonlinear Time-History Procedure: Performance verification over and beyond ASCE 7.

(6) Design and detail the superstructure, isolation plane and substructure.

1.6.2 ASCE 7 Equivalent Lateral Force Procedure (ELF)

The ELF procedure is a displacement-based method that uses simple equations to determine isolated structure response. It is often used in preliminary design and basic isolated building response parameters for comparison purposes and determining target isolator properties. Although the ELF procedure is considered a linear method of analysis, the equations incorporate amplitude-dependent values of effective stiffness and damping to account implicitly for the nonlinear properties of the isolation system. The equations are consistent with the nonlinear static procedure of ASCE 41, assuming the superstructure is rigid and lateral displacements occur primarily in the isolation system. The equivalent lateral force procedure of ASCE 7-16 [2] Section 17.5 is permitted to be used for the design of a seismically isolated structure provided that all of the ASCE 7-16 [2] Section 17.4.1 requirements items are satisfied. These requirements shall be evaluated separately for upper bound and lower bound isolation system properties, and the more restrictive requirement shall govern. This method can efficiently estimate the total base shear, effective isolator period, effective damping, and maximum isolator displacements. The steps in the ELF procedure for friction pendulum isolators are indicated below.

(1) Determine isolator yielding displacements (D_Y)

$$D_Y = (u_2 - u_1) R_1 \quad (1.1)$$

(2) Select an initial isolator displacement (seed), (D_M) This can be roughly estimated per target isolator period using SDOF approach.

(3) Restoring Force (F_M).

$$F_M = \left[u_2 + \frac{D_M - D_Y}{R_2} \right] W \quad (1.2)$$

(4) Determine effective stiffness (k_M).

$$k_M = \frac{F_M}{D_M} \quad (1.3)$$

(5) Determine effective period (T_M).

$$T_M = 2\pi \sqrt{\frac{W}{k_M g}} \quad (1.4)$$

(6) Determine effective damping (β_M).

$$\beta_M = \frac{E_M}{2\pi k_M D_M^2} \quad (1.5)$$

(7) Determine damping coefficient (B_M) from ASCE 7-16 [2] Table 17.5-1

(8) Isolator Displacement (D'_M)

$$D'_M = \frac{g S_{M1} T_M}{4\pi^2 B_M} \quad (1.6)$$

(9) Check if (D'_M) \approx (D_M) otherwise return to step 2

(10) Resultant total base shear (V_b).

For isolators and substructure:

$$V_b = \frac{S_{M1} W}{B_M T_M} = k_M D_M \quad (1.7)$$

For superstructure:

$$V_s = \frac{S_{M1} W}{R_I B_M T_M} = \frac{k_M D_M}{R_I} \quad (1.8)$$

(11) Estimate total isolator displacement D_{TM} , including accidental torsion.

$$D_{TM} = D_M \left[1 + \frac{y}{P_T^2} \frac{12e}{b^2 + d^2} \right] \quad (1.9)$$

$$P_T = \frac{1}{r_1} \sqrt{\frac{\sum_{i=1}^N (x_1^2 + y_1^2)}{N}} \quad (1.10)$$

$$r_1 = \sqrt{\frac{b^2 + d^2}{12}} \quad (1.11)$$

Where

D_M : Displacement at the center of rigidity of the isolation system in the direction under consideration as prescribed by ASCE 7-16 [2] Equation (17.5-1).

D_{TM} : The total isolator maximum displacement, which shall not be taken as less than $1.15D_M$.

V_b : Base shear at isolation level determined using both upper bound and lower bound isolation system properties.

V_s : Total reduced lateral seismic design force or shear on elements above the base level.

W : Effective seismic weight of the structure above the isolation interface as defined in ASCE 7-16 [2] Section 12.7.2.

k_M : Effective stiffness [kip/in. (kN/mm)] of the isolation system at the maximum displacement, D_M , as prescribed by ASCE 7-16 [2] Equation (17.2-3).

T_M : Effective period of the seismically isolated structure [s] at the displacement D_M in the direction under consideration, as prescribed by ASCE 7-16 [2] Equation (17.5-2).

B_M : Numerical coefficient as set forth in ASCE 7-16 [2] Table 17.5-1 for the effective damping of the isolation system β_M at the displacement D_M .

β_M : Effective damping of the isolation system at the displacement D_M , as prescribed by Equation(17.2-4).

E_D : Energy dissipated per cycle of design displacement response.

g : Acceleration due to gravity acceleration caused by gravity [in/s² (mm/s²)] if the units of k_M are in kip/in. (kN/mm).

R_I : Numerical coefficient related to the type of seismic force-resisting system above the isolation system.

S_{M1} : MCE_R , 5% damped spectral acceleration parameter at 1-s period, in units of g-s, as

determined in ASCE 7-16 [2] Section 11.4.4 or 11.4.8.

x_i, y_i : Horizontal distances [ft (mm)] from the center of mass to the i^{th} isolator unit in the two horizontal axes of the isolation system.

N : Number of isolator units.

$u1$ and $u2$: coefficient of friction for concave surfaces.

$R1, R2$: radius of curvature for concave plates.

y : the distance between the centers of rigidity of the isolation system and the element of interest measured perpendicular to the direction of seismic loading under consideration.

e : the actual eccentricity measured in plan between the center of mass of the structure above the isolation interface and the center of rigidity of the isolation system, plus accidental eccentricity, in ft (mm), taken as 5% of the longest plan dimension of the structure perpendicular to the direction of force under consideration.

P_T : Ratio of the effective translational period of the isolation system to the effective torsional period of the isolation system, as calculated by dynamic analysis or as prescribed by ASCE 7-16 [2] Equation (17.5-4) but need not be taken as less than 1.0.

r_I : Radius of gyration of the isolation system [ft (mm)].

b : The shortest plan dimension of the structure [ft (mm)] measured perpendicular to d .

d : the longest plan dimension of the structure.

CHAPTER 2

Triple Friction Pendulum Bearings

The friction pendulum concept was proposed by Penkuhn [69], Zayas et al. [102] presented a specific friction pendulum design—namely, the “single friction pendulum (SFP Figure 2.1)”, which includes an inner friction slider that sits on a spherical concave surface. The motion of the slider and the constant friction produces a bilinear backbone curve that defines the envelope of the lateral movement and the lateral resultant force relationship. The primary/initial stiffness of the friction pendulum is much larger than the secondary one, and in order to make the transition smoother, Earthquake Protective Systems Corporation (EPS) developed the “Triple Friction Pendulum (TFP)” device. As shown in Figure 2.2, this device has 4 stacked sliding surfaces, with R_n ($n = 1 : 4$) and μ_n ($n = 1 : 4$) denoting the radius and friction coefficient of each sliding surface. Typically, the inner 2 surfaces have identical properties (i.e., $R_1 = R_2$, $\mu_1 = \mu_2$).

2.1 Uniaxial Behavior of a TFP Bearing

Fenz and Constantinou [20, 27], and Morgan and Mahin [59] obtained the unidirectional behavior of TFP bearings by taking the equilibrium of each stage to find the force-deformation relationship. The uniaxial behavior of TFP bearings can be separated into five stages:

Stage I: Sliding begins at the inner sliding surface, wherein the friction coefficient is the smallest, $F \geq \mu_1 W$.

$$F = u \frac{W}{L_1 + L_2} + \frac{\mu_1 L_1 + \mu_2 L_2}{L_1 + L_2} W. \quad (2.1)$$

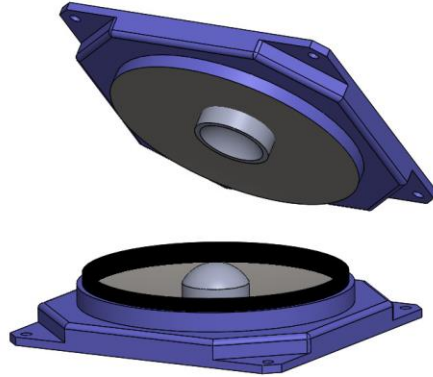


Figure 2.1: Single Friction Pendulum [30]

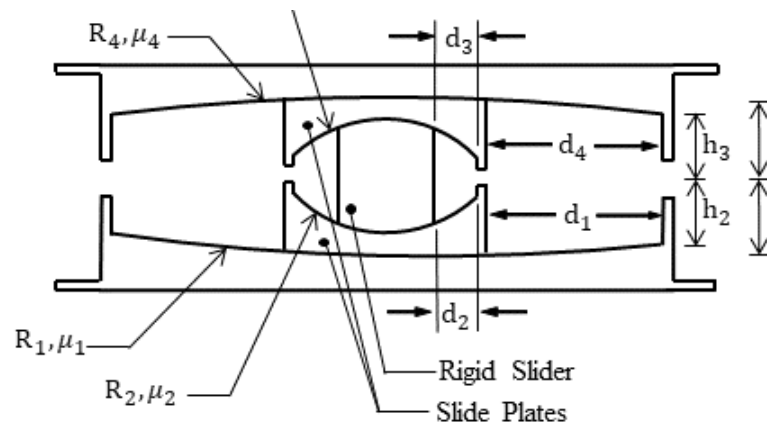


Figure 2.2: Triple Friction Pendulum Bearing section view and basic parameters.

Where W is the normal pressure and L_n ($n = 1 : 4$) is the effective pendulum length, which equals the radius of each surface subtracted by the distance from the sliding surface to the mid-height of the bearing. When the shear force reaches the friction force on the outer-bottom sliding surface, the second stage will activate. This transition happens when the displacement is equal to

$$u^* = 2L_1 (\mu_3 - \mu_1). \quad (2.2)$$

Stage II: When u^* is reached, the sliding occurs at the bottom sliding surface and the inner-upper sliding surface. The force-displacement relationship then is

$$F = u \frac{W}{L_2 + L_3} + \frac{\mu_2 L_2 + \mu_3 L_3 - (\mu_3 - \mu_1) L_1}{L_2 + L_3} W. \quad (2.3)$$

When the shear force reaches the friction force of the upper sliding surface, the third stage will activate, the corresponding displacement is

$$u^{**} = u^* + (\mu_4 - \mu_3) (L_2 + L_3). \quad (2.4)$$

Stage III: When $u \geq u^{**}$, sliding will initiate on the top-outer surface, and continue on the outer-bottom sliding surface, but stop on the inner two surfaces. The force-displacement relationship is given by

$$F = u \frac{W}{L_3 + L_4} + \frac{\mu_3 L_3 + \mu_4 L_4 - (\mu_3 - \mu_1) L_1 - (\mu_4 - \mu_2) L_2}{L_3 + L_4} W. \quad (2.5)$$

This stage stops when the inner-bottom slider contacts the outer bottom restrainer. The corresponding displacement is

$$u^{*3} = u^{**} + u_{3 \max} \left(1 + \frac{L_4}{L_3} \right) - (\mu_4 - \mu_3) (L_3 + L_4). \quad (2.6)$$

Stage IV: In this stage, the motion continues on the outer-upper sliding surface and the inner-bottom surface, until the outer-top slider contacts its restrainer. The bearing force will increase with a slope of $\frac{1}{L_1 + L_3}$. As one can see, this slope is larger than the previous stage. The final displacement of this stage is

$$u^{*4} = u^{*3} + \left[\left(\frac{u_{4 \max}}{L_4} + \mu_4 \right) - \left(\frac{u_{3 \max}}{L_3} + \mu_3 \right) \right] (L_2 + L_4). \quad (2.7)$$

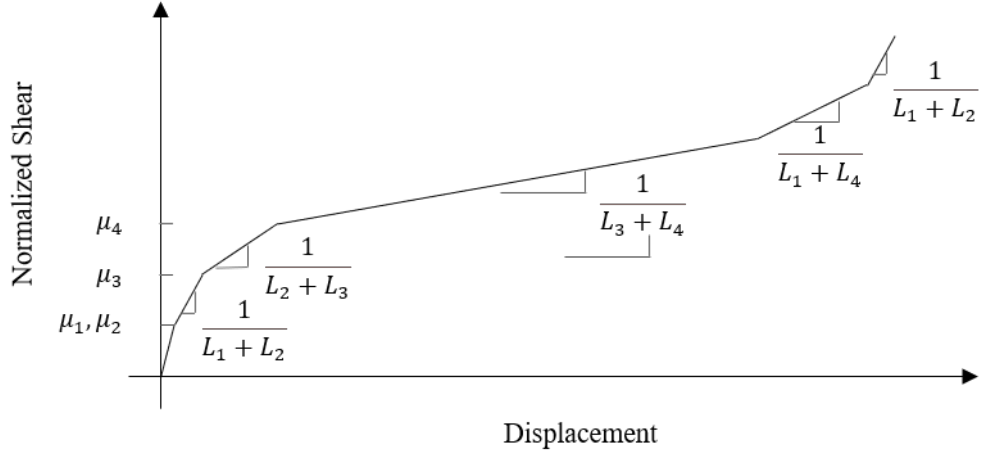


Figure 2.3: Uniaxial behavior of the TFP bearing ($\mu_1 = \mu_2, L_1 = L_2$)

Stage V: The motion happens on the two inner surfaces and the bearing force increases with a slope of $\frac{1}{L_1+L_2}$, which is greater than that for Stage IV,

$$U_{\max} = u^{*5} = \sum_{n=1}^4 u_{\max n}. \quad (2.8)$$

The uniaxial response TFP bearings is shown in Figure 2.3

2.2 Biaxial Behavior of a TFP Bearing

Becker and Mahin [5] developed a 2D omnidirectional model based on geometric compatibility and sliding surface constitutive relationship. In this model, the hysteretic behavior of each sliding surface was described by a bi-directional plasticity element proposed by Mosqueda et al. [62]. Through controlled-displacement experiments and unrestrained shake table experiments, this omnidirectional model was validated. Since the motion of each surface is described separately, one advantage of this omnidirectional model is that it can capture the hysteretic response of all sliding surfaces.

Later, based on the idea of a serially connected spring model for TFP bearings, Dao et al. [23] implemented a numerical model in OpenSees [53]. From Figure 2.4, it is seen that

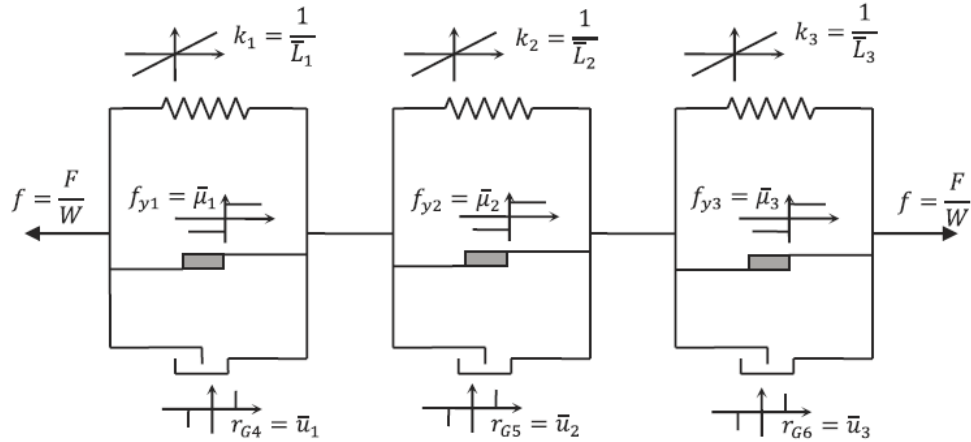


Figure 2.4: Series spring model for multi-stage behavior of TFP bearing [23].

each sliding surface consists a linear spring element, a friction element, and a bi-directional gap element. The linear spring and friction elements were combined into a single bilinear plasticity element for simplification in implementation. The modification is shown in the following Figure 2.5. The modified model will recover the original series spring model if $k_{01}, k_{02}, k_{03}, k_{04}, k_{05}$ and k_{06} go to infinity.

The flow chart of recovering the force-displacement relationship of the TFP bearing model by Dao et al. [23] is shown in Figure 2.6. This algorithm contains two levels of iteration. On the right-hand side, the iteration starts at the three-element groups: given the trial force vector, the local stiffness matrix, and the displacement matrix can be computed by using a return-mapping algorithm proposed by Simo and Hughes [82]. For the TFP bearing element level, the iteration gives back the global stiffness matrix and the force vector. Drazin and Govindjee [25] provides the current most complete single model currently for TFP devices that incorporates the full nonlinear kinetics of the TFP system while allowing for bi-directional motion.

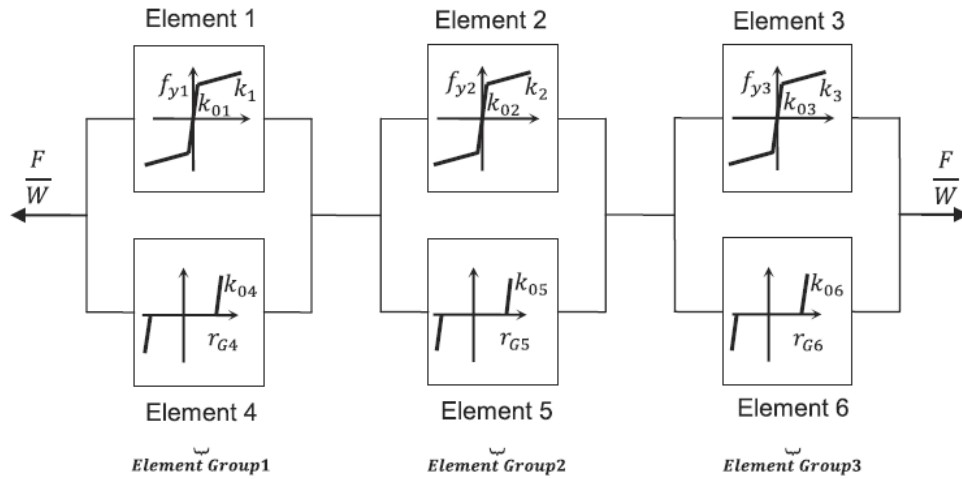


Figure 2.5: Modified series spring model for multi-stage behavior of a TFP bearing [23].

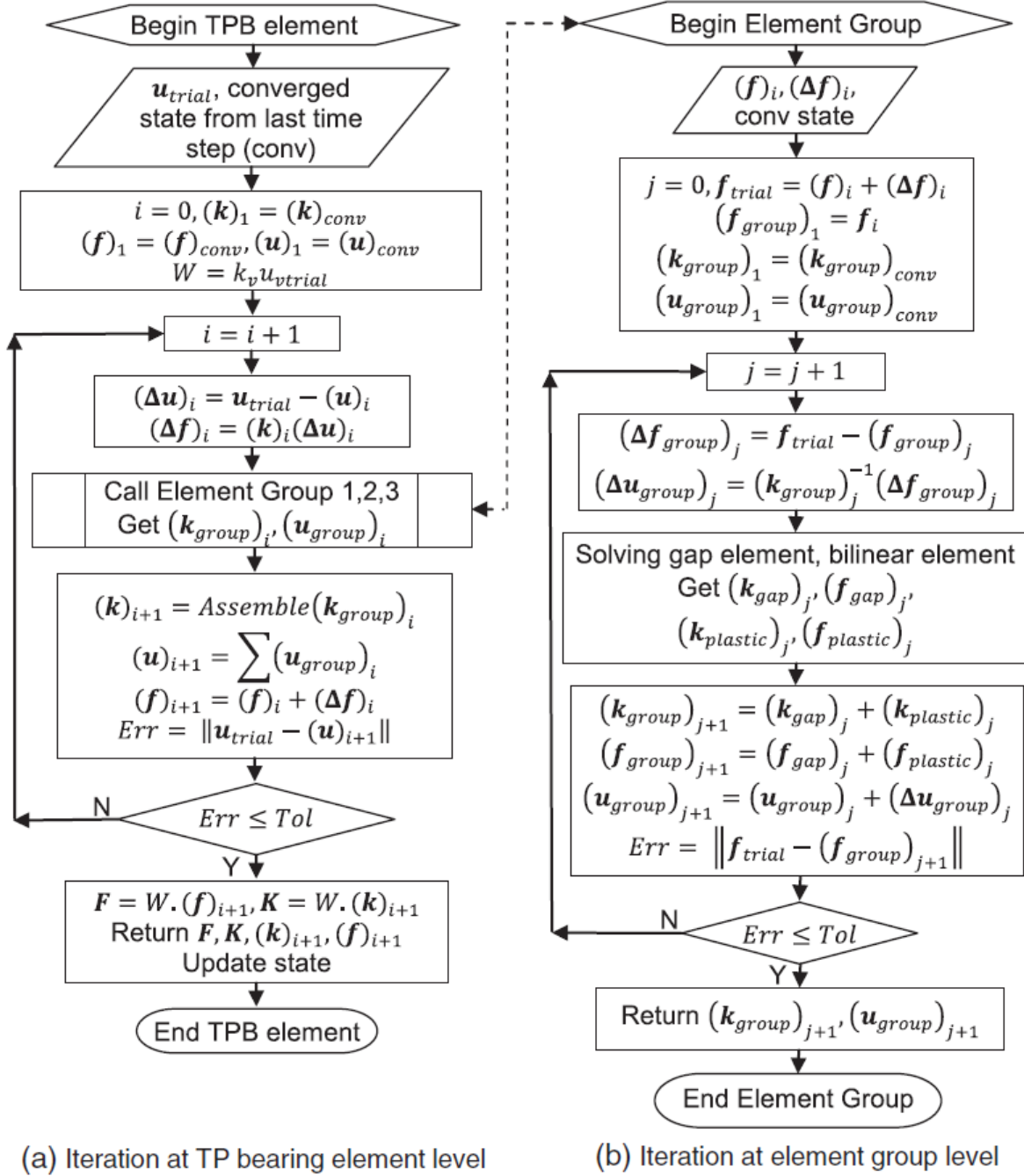


Figure 2.6: Flow chart for solving TFP bearing element [23].

CHAPTER 3

Three-dimensional Finite Element Modeling of TFP Bearing Devices

In this chapter, a high-fidelity 3D finite element modeling procedure for TFP bearings will be introduced. The modeling and analyses presented here were carried out using ABAQUS [87]. The motivation for using such a modeling approach is to use first principles for capturing the coupled thermo-tribo-mechanical behavior of TFP bearings; and (if such a model can be validated using experimental data) then to use this model to parametrically study the range of TFP behavior through numerical simulations beyond what existing experimental data alone can provide.

3.1 Modeling the Geometry of TFP Bearings

In order to compare simulated behavior with experimental results, geometry is selected from the experimental-analytical study by Becker and Mahin [5]. The said geometry is described in Table 3.1.

The inner two sliders share identical mechanical properties. Except for the friction coefficients, mechanical properties of the two outer sliding surfaces are also identical. In Becker and Mahin's paper [5], some important mechanical properties, such as Young's modulus and Poisson's ratio were omitted. Instead, sliders used in the experiment were assumed to be made of steel (i.e., $E = 200$ GPa, $\mu = 0.3$). The friction coefficients of the inner, outer bottom, and outer top sliding surfaces were 3.6%, 11.8%, and 12.8%, respectively.

Table 3.1: Geometry of the TFP bearing used in the experimental test.

	Inner sliding surfaces	Outer sliding surfaces
Dish radius (in)	3.0	39.0
Height (in)	0.5	1.0
Outer diameter (in)	2.5	10.0
Inner diameter (in)	1.5	3.0

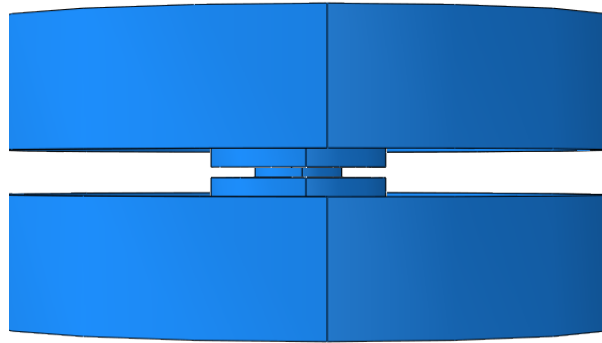


Figure 3.1: The ABAQUS TFP bearing model geometry.

There were five components of the tested TFP bearing: a center slider, two inners, and two outer sliders. Each part was built up separately and was subsequently assembled shown in Figure 3.1.

3.2 Meshing Process and Element Types

In the TFP bearing model, there was no plastic deformation of the metal components, and all the material strains were in the elastic range. Given this, the eight-node brick element with reduced integration (C3D8R, Figure 3.2) was deemed sufficiently accurate. In order to improve the computational efficiency, the reduced integration technique was adopted.

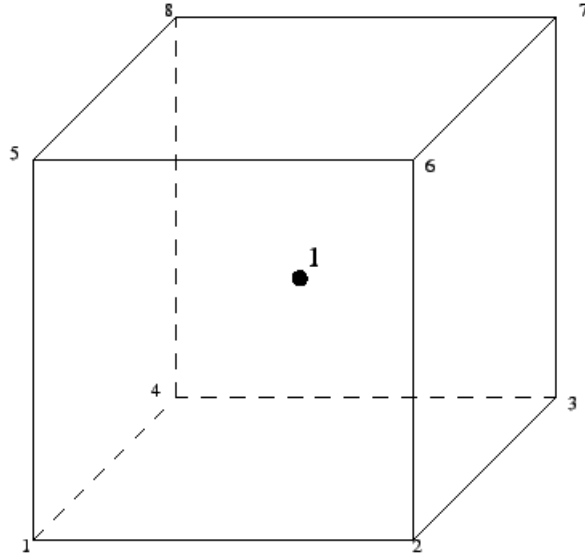
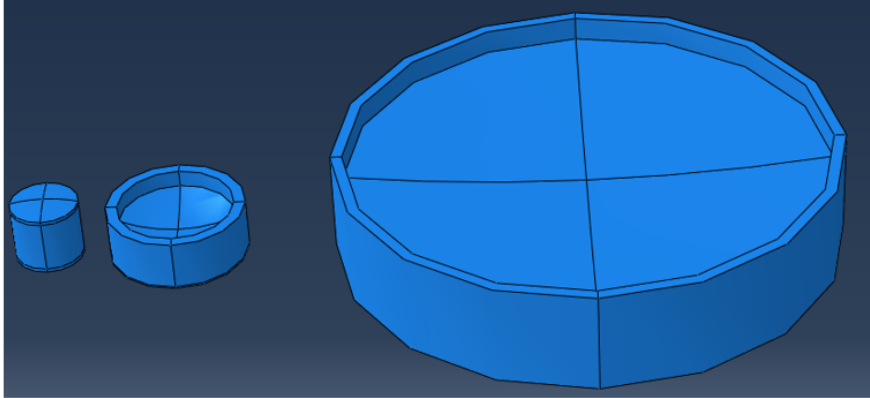


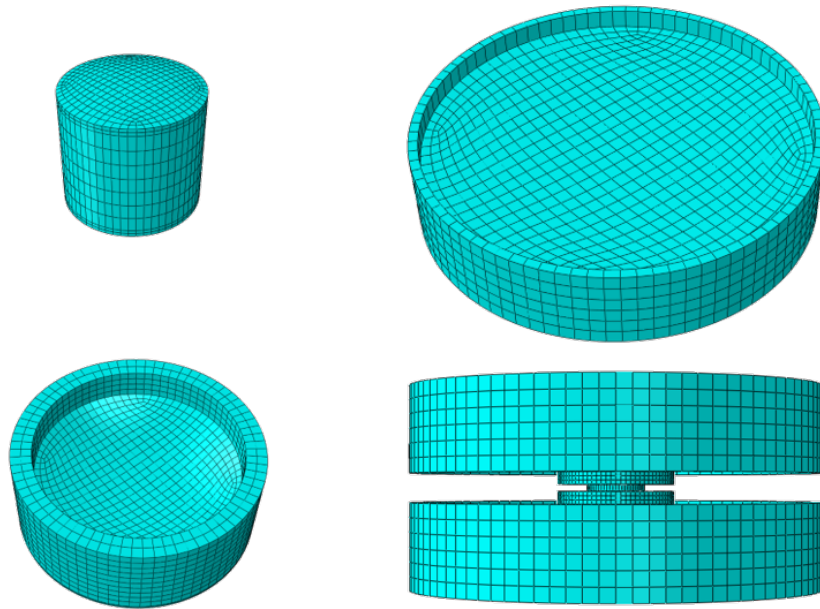
Figure 3.2: Eight-node brick element.

In order to avoid irregular and severely distorted elements, partitioning of each component was necessary. The center slider was split into four parts, but restrainer portions were separated from the main parts for the other sliders. Then the left “cylinder”, which is similar to the center slider, was split into four identical parts. Details of these partitions are shown in Figure 3.3 (a). Thereafter, the structural mesh is shown in Figure 3.3 (b).

The total number of elements has a significant effect on computational efficiency. Thus, one can reduce the number of elements when precisely capturing the stresses and strains relationship is not critical. The size of the center slider is tiny compared to the outer sliders, and the inner slider will experience much more deformation than the outer slider. Thus, the element size for the center slider was the smallest. For simplification, the outer slider was defined as a rigid body.



(a)



(b)

Figure 3.3: Partition (a) and meshing (b) of the TFP bearing.

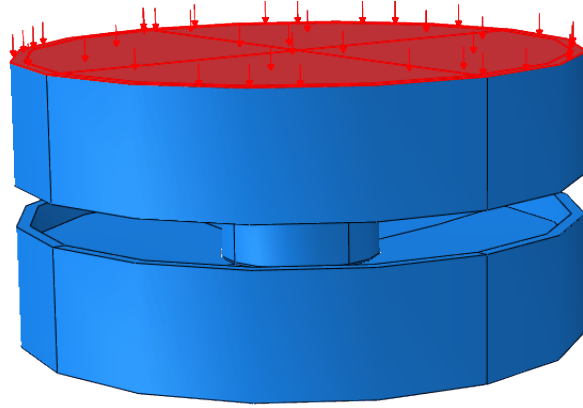


Figure 3.4: Boundary and loading conditions.

3.3 Contact Modeling, Boundary and Loading Conditions

In this TFP bearing model, a “hard contact” law was chosen, wherein the contact constraint is applied when the clearance between two surfaces becomes zero. There was no restriction on the pressure transmitted between the contact surfaces. For each sliding surface, the larger and smaller surfaces were respectively set as master and slave surfaces. Finally, the “finite sliding” option was chosen.

A Cartesian coordinate system is used for modeling. 2.4 kips of normal pressure was applied to the outer-top slider, which was the same conditions in the experimental setup. A biaxial displacement was then prescribed at the bottom-outer slide. Rotations about the global X, Y, Z axes and also the vertical displacement were constrained. No rotation about global X, Y, Z axes were allowed for the outer-top slider, and movements in the X and Z directions were also constrained. However, there was no restriction in the vertical (Y) direction. Since the two outer sliders were set as rigid bodies, all the constraints were applied on the reference points shown in Figure 3.4.

3.4 The Solution Methods

An implicit time-stepping algorithm was chosen for this model. Theoretically, the explicit method should be more efficient; however, the small increment size is required to resolve the contact constraints for explicit time-stepping resulting in an extremely large number of time steps since the maximum time increment governs by the smallest element size. The required time increment size is still too small, although the mass scaling technique is being applied. Furthermore, the results of the explicit method exhibited spurious oscillations. As such, the implicit method was chosen.

3.5 Validating the Continuum Finite Element Model

In 2011, controlled-displacement experiments of the TFP bearing were conducted at the UC, Berkeley, aimed at characterizing the bidirectional behavior of TFP bearings [5]. A simple rigid superstructure sat on four identical TFP bearings. The lateral displacement of the superstructure was constrained, while horizontal displacement histories were imposed at the bottom of the bearing using a shake table (Figure 3.5). The maximum lateral displacement was ± 5 inches.

There are four controlled-displacement orbits in total used for bearing characterization. These are, namely, the sine waves, circular, square-shaped, and eight-shaped. The sine waves loading path of the experiment is shown in Figure 3.6 (a). The experiment and ABAQUS FEM results are shown in Figure 3.6 (b) and (c) separately. For the sine wave test, it can be seen that the finite element model captures the experimental hysteretic response very well, which validates the ABAQUS FEM results. Regarding the circular displacement orbit shown in Figure 3.7, the ABAQUS FEM model capture the trend of the experiment results, which validates the ABAQUS FEM results again. The ABAQUS FEM model exhibits hardening more than the experimental response, but still, it does not deviate from the actual results too far. This difference might be due to an assumed Young's modulus, which was not explicitly

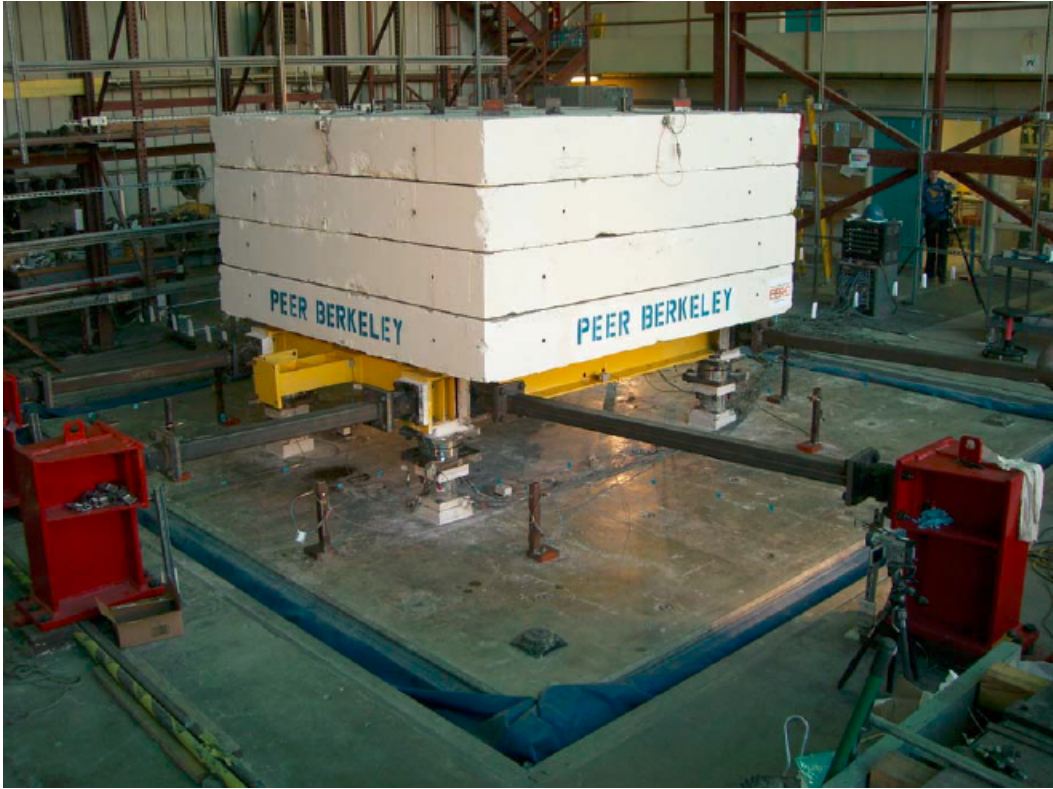
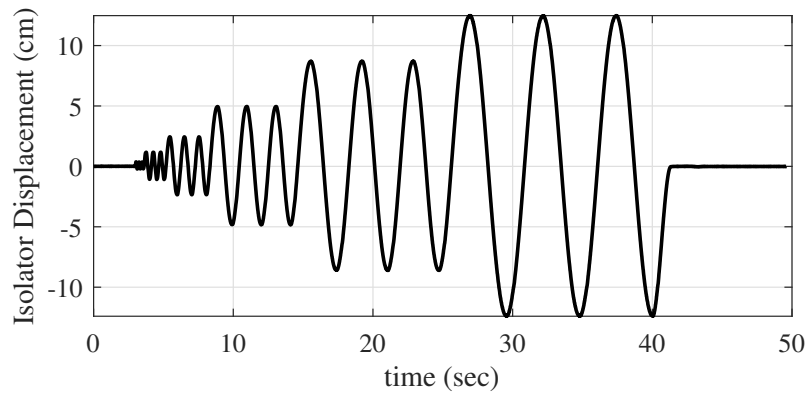
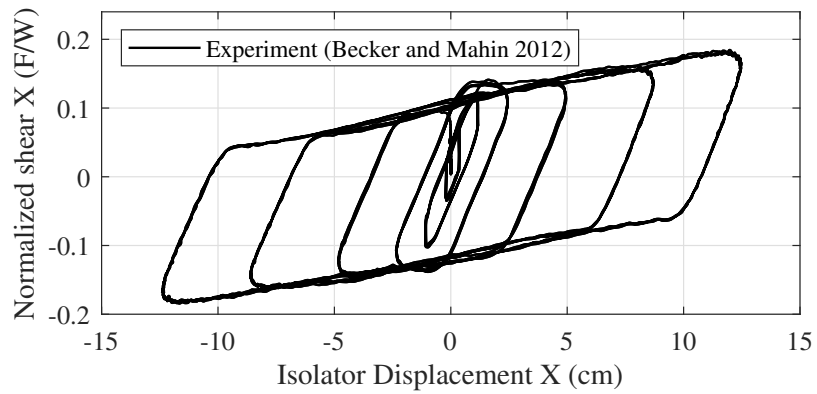


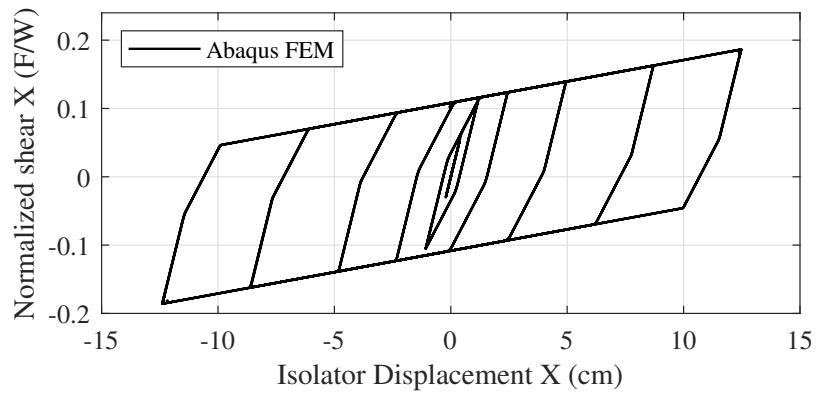
Figure 3.5: Rigid block setup at the UC Berkeley PEER earthquake simulator laboratory [5].



(a)



(b)



(c)

Figure 3.6: Isolator displacement time-history under sine waves (a), hysteresis of the isolator in experiment results (b) [5] and ABAQUS finite element analysis results (c).

provided by Becker and Mahin [5].

For the square-shaped and eight-shaped displacement orbit, there is no ABAQUS FEM model result available because those did not converge. The convergence problem came from the multi-surface contact constraints (as reported by ABAQUS). There are four curved sliding surfaces in total, and no essential boundary condition applies to the center slider and the inner sliders. Even though the total number of finite elements is not very large, computational time to satisfy the contact constraints for this particular case was extremely large. A potential remedy for this issue appears to be to refine the mesh, but these efforts are deferred to a future study.

From these loading cases, the ABAQUS FEM model is seen, in general, to be highly capable of capturing the hysteretic responses of TFP bearings while not being precisely accurate. Various reasons are causing the predictions to deviate from the experiments. For example, the input mechanical properties were not necessarily identical to the test specimen's (recall that the experimenters did not provide this information); discrepancies were expected. The agreement can be improved with better material parameter selection and potentially by refining the spatial (mesh sizes) and temporal (time increment) resolution of the ABAQUS FEM model. As one can see, modeling the TFP hysteric response utilizing the continuum finite element method in a particular case is acceptable. However, this method is not suitable for large-scale analysis, for example, important building design, since the analysis is time-consuming and unstable. Other efficient and stable methods should be utilized in general.

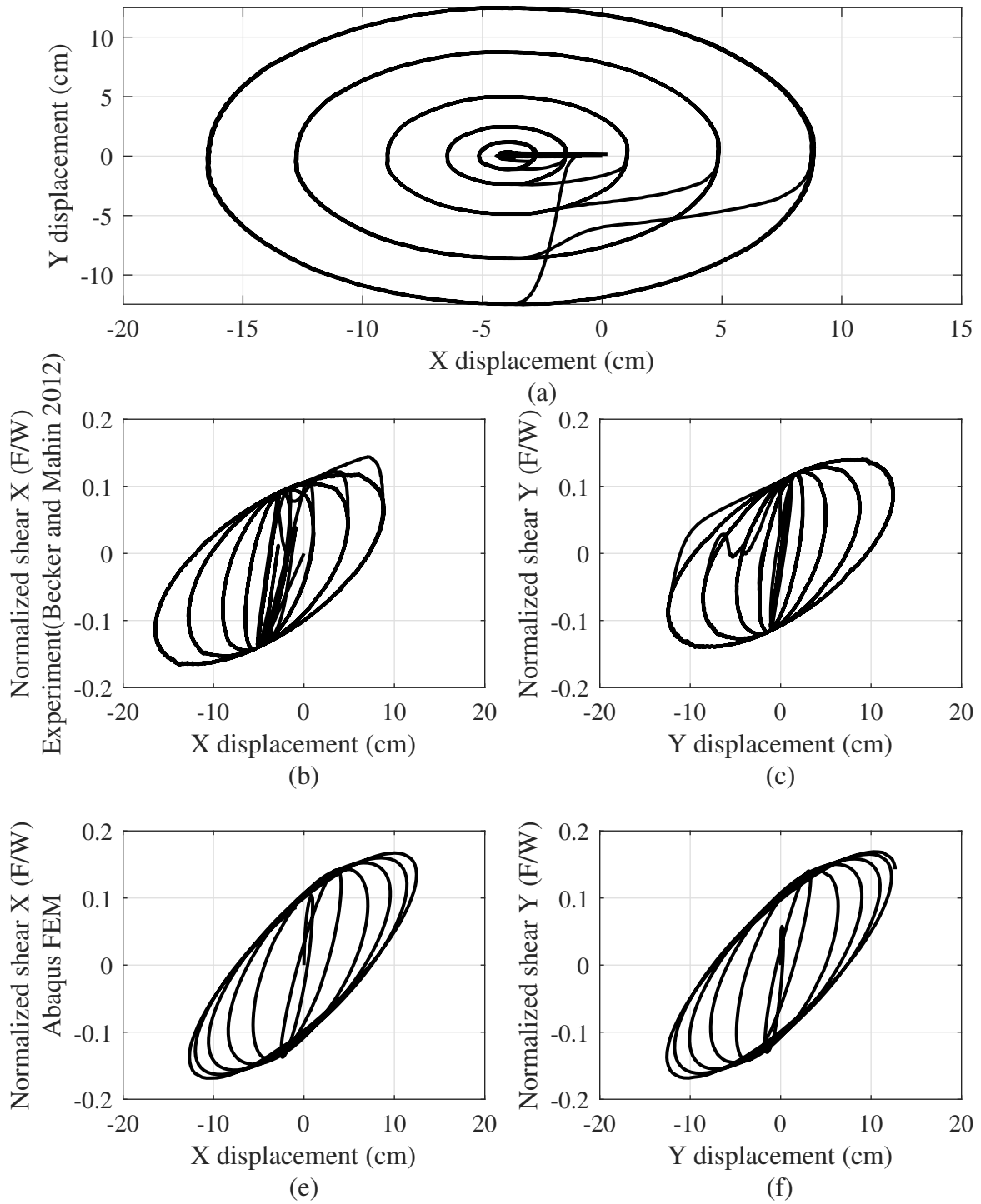


Figure 3.7: Isolator circular displacement orbit (a), hysteresis of the isolator in experiment results (b)(c) [5], and ABAQUS finite element analysis results (d)(e).

CHAPTER 4

An Omnidirectional Modeling Approach for Hysteretic Response of TFP Bearings

As stated earlier, TFP bearings rely on friction to dissipate seismic energy and have highly nonlinear and complex response mechanisms; the continuum finite element method also has its' disadvantages. An alternative to the use of geometric compatibility and sliding surface constitutive relationships is to use a bidirectional Bouc-Wen model [67], which was originally developed by Bouc [8] and generalized by Wen [98]. However, the Bouc-Wen model is a pure phenomenological model and hard to add additional functions. Therefore, this study discards the Bouc-Wen model. Another candidate is the multi-surface plasticity modeling concept; it can represent the multi-stage hardening behavior of TFP bearings consistently under multiaxial loading cycles. The multi-surface plasticity model that will be adopted herein for this purpose is an extension of the classical J2 plasticity model, presented, for example, by Simo and Hughes [82]. In order to capture the Masing behavior of nonlinear materials, Montáns [56, 57, 54, 55] developed various of implicit algorithms for multi-surface J2-plasticity. The corresponding multiaxial nonlinear hardening function is described in a relatively simple way. Coincidentally, biaxial lateral responses are often required in seismic response simulation. Therefore, Montáns' multi-surface plasticity model satisfies the requirement for modeling the hysteretic behavior of TFP bearings [49, 50].

4.1 Implicit Algorithm for Multi-surface Plasticity

In this section, the implicit algorithm for multi-surface plasticity will be discussed in detail. The model is deviatoric, and $\boldsymbol{\sigma}$ is the current deviatoric stress tensor and $\boldsymbol{\sigma}^f$ is the full stress tensor [56]. The symbol $\mathbf{1}$ represents the second-order identity tensor, and \mathbf{I} the fourth-order identity tensor. The symbol “:” represents double contraction—for example $\boldsymbol{\sigma} : \boldsymbol{\varepsilon} = \sigma_{ij}\varepsilon_{ij}$, and $\|\boldsymbol{\sigma}\| = \sqrt{\boldsymbol{\sigma} : \boldsymbol{\sigma}}$. The yield condition is described as

$$f := \|\boldsymbol{\sigma} - \boldsymbol{\alpha}\| - r. \quad (4.1)$$

where $\boldsymbol{\alpha}$ is the back-stress tensor (i.e., the deviatoric-projection of the center of the hyper-cylinder), and r is the radius of the hyper-cylinder. There will be several loading surfaces in the multi-surface plasticity model, and the elastic part is in the innermost circle. The centers of all loading surfaces are at the origin at the beginning. When the stress increases beyond the elastic region, the first loading surface will begin to harden kinematically according to the hardening modulus with the first loading surface. Likewise, when the stress reaches the second loading surface, the material hardens kinematically according to the hardening modulus associated with the second loading surface. Two inner surfaces contact at the current stress point. The yield condition can be expressed as

$$f^1 := \|\boldsymbol{\sigma} - \boldsymbol{\alpha}^1\| - r^1. \quad (4.2)$$

The super index denotes the number of the yield surface. The back-stress tensor is at the origin in virgin state—i.e., $\boldsymbol{\alpha}^i = 0$ where $i = 1, \dots, N$. Additionally, the overlap between surfaces is forbidden, the stress and back-stress tensor should satisfy the following condition:

$$\|\boldsymbol{\sigma} - \boldsymbol{\alpha}^i\| > \|\boldsymbol{\sigma} - \boldsymbol{\alpha}^j\| \quad \forall i > j. \quad (4.3)$$

In order to achieve this goal, a translation rule for the back-stress tensor is needed. Therefore, the well-known explicit translation rule—the Mróz translation rule—is adopted here.

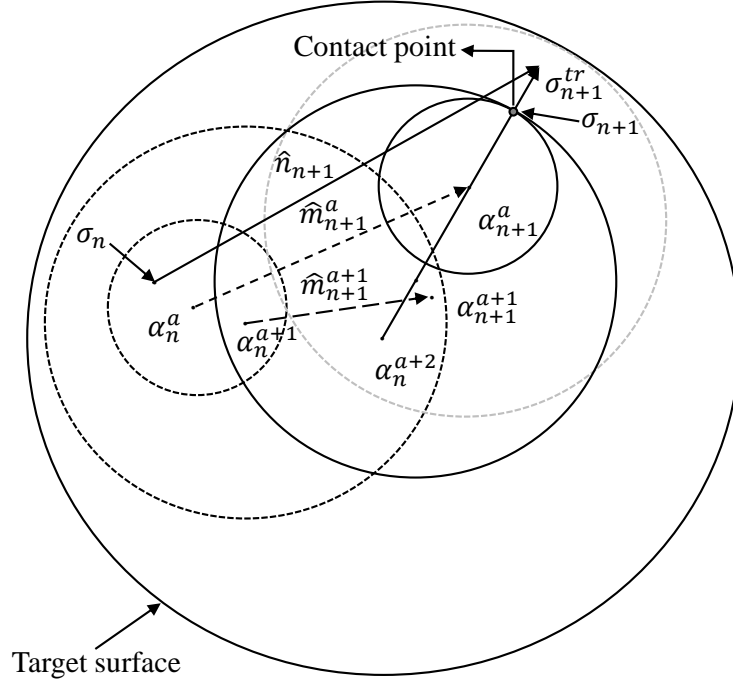


Figure 4.1: The Mroz's translation rules for multisurface plasticity

4.2 Mroz's Translation Rule

The Mroz's translation rule (Figure 4.1) was derived initially by Mróz [63]; later on, Montáns developed implicit algorithm and modified it in 2006 [56, 12]. From Figure 4.1, the moving direction of each surface can be expressed as

$$\mathbf{m} = \frac{r^{a+1}}{\|\boldsymbol{\sigma} - \boldsymbol{\alpha}^a\|} (\boldsymbol{\sigma} - \boldsymbol{\alpha}^a) - (\boldsymbol{\sigma} - \boldsymbol{\alpha}^{a+1}). \quad (4.4)$$

Where a is the 'active' loading surface, and $(a+1)$ is the 'target' surface. The 'active' surface means the current stress state is on the a^{th} yield surface, but inside the $(a+1)^{th}$ yield surface.

This condition can be expressed as

$$f^a := \|\boldsymbol{\sigma} - \boldsymbol{\alpha}^a\| - r^a = 0 \quad \text{and} \quad f^{a+1} := \|\boldsymbol{\sigma} - \boldsymbol{\alpha}^{a+1}\| - r^{a+1} < 0. \quad (4.5)$$

For simplification, in the following section, $\sigma^a = \alpha$, $r^{a+1} = R$, and $r^a = r$. Also, σ is on the ‘ i -th’ surface means that $f^1(\sigma) = 0$. The material enters the plastic region when

$$\dot{\sigma} : \hat{\mathbf{n}} > 0 \quad \text{and} \quad f^1(\sigma) = 0, \quad (4.6)$$

where $\dot{\sigma}$ is stress-rate tensor and $\hat{\mathbf{n}}$ is the normal unitary ‘tensor’ of the yield surface. The consistency condition is

$$\dot{f}^1 = 0. \quad (4.7)$$

When the flow rule is established, the consistency parameter $\dot{\gamma}$ can be determined. The most common flow rule is the associative flow rule, in which the plastification direction is normal to the yield surface. The strain-rate tensor can be decomposed additively into elastic and plastic parts, as in:

$$\dot{\epsilon} = \dot{\epsilon}^e + \dot{\epsilon}^p \quad (4.8)$$

$$\dot{\epsilon}^p = \dot{\gamma} \hat{\mathbf{n}}. \quad (4.9)$$

Therefore, the stress-rate tensor can be computed by the elastic strain-rate tensor

$$\dot{\sigma} = \mathbb{C} : \dot{\epsilon}^e = \mathbb{C} : (\dot{\epsilon} - \dot{\gamma} \hat{\mathbf{n}}), \quad (4.10)$$

where \mathbb{C} is the elastic forth-order tensor. The consistency condition $\dot{f}^1 = 0$ is equivalent to

$$\hat{\mathbf{n}} : (\dot{\sigma} - \dot{\alpha}) = 0, \quad (4.11)$$

$$\dot{\alpha} = \dot{\gamma} H \hat{\mathbf{m}}. \quad (4.12)$$

Where H is the kinematic hardening modulus, $\hat{\mathbf{m}}$ is the unitary translation tensor, and \mathbf{H} is the general hardening tensor. Substituting Equation 4.10 and Equation 4.12 into Equation 4.11, the consistency parameter can be computed via

$$\dot{\gamma} = \frac{\hat{\mathbf{n}} : \mathbb{C} : \dot{\epsilon}}{\hat{\mathbf{n}} : \mathbb{C} : \hat{\mathbf{n}} + \hat{\mathbf{n}} : \mathbf{H} : \hat{\mathbf{m}}}. \quad (4.13)$$

Therefore, the continuum elastoplastic tangent can be obtained as

$$\mathbb{C}^{ep} = \mathbb{C} - \frac{\hat{\mathbf{n}} : \mathbb{C} \otimes \hat{\mathbf{n}} : \mathbb{C}}{\hat{\mathbf{n}} : \mathbb{C} : \hat{\mathbf{n}} + \hat{\mathbf{n}} : \mathbf{H} : \hat{\mathbf{m}}}. \quad (4.14)$$

As one can see, all the quantities used in calculating the moving direction of backstress tensors are based on the converged step n . Thus, in order to obtain an implicit algorithm, the translation rule should be based on the final stress state. The unitary ‘tensor’ normal to the yield surface $\hat{\mathbf{n}}_{n+1}$ can be estimated from trial stress state σ_{n+1}^{tr} in an iterative way since the following equation holds.

$$\hat{\mathbf{n}}_{n+1}(\sigma_{n+1}^{\text{tr}}, \boldsymbol{\alpha}_{n+1}) = \hat{\mathbf{n}}_{n+1}(\sigma_{n+1}, \boldsymbol{\alpha}_{n+1}) \quad (4.15)$$

For simplicity, the ‘target’ normal tensor \mathbf{t}_{n+1} is defined as $\hat{\mathbf{t}}_{n+1} = \frac{1}{\|\sigma_{n+1}^{\text{tr}} - \beta_n\|} (\sigma_{n+1}^{\text{tr}} - \beta_n)$, Where $\beta = \boldsymbol{\alpha}^{a+1}$. The final back-stress tensor of the current surface is computed as

$$\boldsymbol{\alpha}_{n+1}^a = \beta_{n+1} + (R - r)\hat{\mathbf{t}}_{n+1}. \quad (4.16)$$

The center of the target back-stress tensor remains the same as before, therefore, $\beta_{n+1} = \beta_n$, the movement direction of back-stress tensor of the active surface is

$$\mathbf{m}_{n+1} := \mathbf{a}_{n+1} - \mathbf{a}_n \quad (4.17)$$

$$\hat{\mathbf{m}}_{n+1} := \frac{\mathbf{m}_{n+1}}{\|\mathbf{m}_{n+1}\|}. \quad (4.18)$$

Mroz’s translation rule iteratively determines the target surface. All the surfaces in the target surface will contact the final stress state at the end of the step by its own translation rule. Thus, the initial guess is from the inner surface until the target surface is determined. Assuming $a = 1$ is the target surface, the following conditions hold.

$$f^a(\sigma_{n+1}^{\text{tr}}, \boldsymbol{\alpha}_n) > 0 \quad (4.19)$$

$$f^{a+1}(\sigma_{n+1}^{\text{tr}}, \boldsymbol{\alpha}_n) < 0 \quad (4.20)$$

At the final stress state, the consistency condition $f^1 = 0$ is equivalent to

$$\hat{\mathbf{n}} : (\dot{\boldsymbol{\sigma}} - \dot{\boldsymbol{\alpha}}) = 0 \quad (4.21)$$

$$\dot{\boldsymbol{\alpha}} = \dot{\gamma} H \hat{\mathbf{m}}. \quad (4.22)$$

Therefore

$$\boldsymbol{\alpha}_{n+1}^a = \boldsymbol{\alpha}_n^a + \Delta\gamma_{n+1}^a H^a \hat{\mathbf{m}}_{n+1}^a. \quad (4.23)$$

This translation rule is explicitly determined since it depends on the converged stresses and the trial stress state, the superscript is dropped to differentiate it from the inner surfaces, which means $\hat{\mathbf{m}}_{n+1}^a = \hat{\mathbf{m}}_{n+1}$, $r^a = r$. The final back-stress tensor of inner surfaces ($i \leq a$) can be obtained by the condition that the final stress tensor $\boldsymbol{\sigma}_{n+1}$ contacts each inner surface.

$$\boldsymbol{\alpha}_{n+1}^i = \boldsymbol{\sigma}_{n+1} - (r - r^i) \hat{\mathbf{n}}_{n+1} \quad (4.24)$$

The translation rule for the inner surface is

$$\boldsymbol{\alpha}_{n+1}^i = \boldsymbol{\alpha}_n^i + \Delta\gamma_{n+1}^i H^i \hat{\mathbf{m}}_{n+1}^i. \quad (4.25)$$

Therefore,

$$\mathbf{m}_{n+1}^i := (\boldsymbol{\alpha}_n - \boldsymbol{\alpha}_n^i) + (r - r^i) \hat{\mathbf{n}}_{n+1} + \bar{H}^a \Delta\gamma_{n+1}^a \hat{\mathbf{m}}_{n+1}^a. \quad (4.26)$$

This tensor depends on the normal to the yield surface $\hat{\mathbf{n}}_{n+1}$ at the final stress state; thus, it must be calculated with consistency parameter γ by iteration. The final stress state is based on the trial stress state, which is defined as follows.

$$\boldsymbol{\sigma}_{n+1}^{tr} = \boldsymbol{\sigma}_n + 2\mu\Delta\boldsymbol{\varepsilon} \quad (4.27)$$

where $\Delta\boldsymbol{\varepsilon}$ is the strain increment from stress state n to $n + 1$. The subscript has been omitted, since no ambiguity will occur by this omission. The final stress state is then

$$\boldsymbol{\sigma}_{n+1} = \boldsymbol{\sigma}_{n+1}^{tr} - 2\mu\Delta\boldsymbol{\varepsilon}^p. \quad (4.28)$$

Note that the strain increment $\Delta\boldsymbol{\varepsilon}$ includes elastic part $\Delta\boldsymbol{\varepsilon}^e$ and plastic part $\Delta\boldsymbol{\varepsilon}^p$ (i.e., $\Delta\boldsymbol{\varepsilon} = \Delta\boldsymbol{\varepsilon}^e + \Delta\boldsymbol{\varepsilon}^p$) which can be expressed as

$$\Delta\boldsymbol{\varepsilon}^p = \Delta\gamma_{n+1} \hat{\mathbf{n}}_{n+1}. \quad (4.29)$$

Plugging Equation 4.29 into Equation 4.28

$$\boldsymbol{\sigma}_{n+1} = \boldsymbol{\sigma}_{n+1}^{tr} - 2\mu\Delta\gamma_{n+1} \hat{\mathbf{n}}_{n+1}. \quad (4.30)$$

Then the consistency condition Equation 4.1 can be rewritten as

$$\|\sigma_{n+1}^{tr} - 2\mu\Delta\gamma_{n+1}\hat{\mathbf{n}}_{n+1} - \boldsymbol{\alpha}_n^a - H^a\Delta\gamma_{n+1}^a\hat{\mathbf{m}}_{n+1}\| - r = 0. \quad (4.31)$$

Where $\hat{\mathbf{n}}_{n+1} := \frac{\mathbf{n}_{n+1}}{\|\mathbf{n}_{n+1}\|}$. Since $\hat{\mathbf{n}}_{n+1}$ is a function of $\Delta\gamma_{n+1}$, \mathbf{n}_{n+1} can be expressed as follows:

$$\mathbf{n}_{n+1} := \boldsymbol{\sigma}_{n+1}^r - \boldsymbol{\alpha}_n^a - H^a\Delta\gamma_{n+1}^a\hat{\mathbf{m}}_{n+1}. \quad (4.32)$$

The consistency parameter can be estimated as

$$\Delta\gamma_{n+1} = |\Delta\gamma_{n+1}^a + \sum_{i=1}^{a-1}\Delta\gamma_{n+1}^i| = \sum_{i=1}^a\Delta\gamma_{n+1}^i. \quad (4.33)$$

The consistency parameters of the inner surfaces can be obtained in the following way. For every $1 \leq i \leq a$,

$$\begin{aligned} \boldsymbol{\sigma}_{n+1} &= \boldsymbol{\alpha}_{n+1}^i + r^i\hat{\mathbf{n}}_{n+1} \\ &= \boldsymbol{\alpha}_n^i + H^i\Delta\gamma_{n+1}^i\hat{\mathbf{m}}_{n+1}^i + r^i\hat{\mathbf{n}}_{n+1}. \end{aligned} \quad (4.34)$$

The final stress tensor contacts each inner surface. Therefore, the following condition holds.

$$\boldsymbol{\alpha}_n^a + H^a\Delta\gamma_{n+1}^a\hat{\mathbf{m}}_{n+1} + r\hat{\mathbf{n}}_{n+1} = \boldsymbol{\alpha}_n^i + H^i\Delta\gamma_{n+1}^i\hat{\mathbf{m}}_{n+1}^i + r^i\hat{\mathbf{n}}_{n+1} \quad (4.35)$$

After rearranging the Equation 4.35, $\Delta\gamma_{n+1}^i$ can be expressed in terms of $\Delta\gamma_{n+1}^a$.

$$\Delta\gamma_{n+1}^i = \left[\frac{H^a}{H^i}\Delta\gamma_{n+1}^a\hat{\mathbf{m}}_{n+1} + \frac{1}{H^i}(\boldsymbol{\alpha}_n - \boldsymbol{\alpha}_n^i) + \frac{(r - r^i)}{H^i}\hat{\mathbf{n}}_{n+1} \right] : \hat{\mathbf{m}}_{n+1}^i = \frac{1}{H^i} \|\mathbf{m}_{n+1}^i\| \quad (4.36)$$

Equation 4.31 can be written in a residual form since $\hat{\mathbf{n}}_{n+1}$ is a function of $\Delta\gamma_{n+1}^a$, and $\hat{\mathbf{m}}_{n+1}^i$ is also a function of a $\Delta\gamma_{n+1}^a$.

$$g(\Delta\gamma_{n+1}^a) = (\boldsymbol{\sigma}_{n+1}^{tr} - \boldsymbol{\alpha}_n^a) : \hat{\mathbf{n}}_{n+1} - H^a\Delta\gamma_{n+1}^a(\hat{\mathbf{m}}_{n+1} : \hat{\mathbf{n}}_{n+1}) - 2\mu\Delta\gamma_{n+1} - r \quad (4.37)$$

The Newton-Raphson method can be utilized to solve the nonlinear Equation 4.37, the derivative of the residual form will be

$$\frac{\partial f_{n+1}}{\partial(\Delta\gamma_{n+1}^a)} = -H^a(\hat{\mathbf{m}}_{n+1} : \hat{\mathbf{n}}_{n+1}) - 2\mu\frac{\partial\Delta\gamma_{n+1}}{\partial\Delta\gamma_{n+1}^a}. \quad (4.38)$$

The derivative of the unitary normal tensor can be expressed as following:

$$\frac{\partial \hat{\mathbf{n}}_{n+1}}{\partial \Delta \gamma_{n+1}^a} = \frac{-H^a}{\|\mathbf{n}_{n+1}\|} (\mathbb{I} - \hat{\mathbf{n}}_{n+1} \otimes \hat{\mathbf{n}}_{n+1}) : \hat{\mathbf{m}}_{n+1}. \quad (4.39)$$

Because $\Delta \gamma_{n+1} = \Delta \gamma_{n+1}^a + \sum_{i=1}^{a-1} \Delta \gamma_{n+1}^i$, the derivative of consistency parameter can be obtained through Equation 4.40.

$$\frac{\partial \Delta \gamma_{n+1}}{\partial \Delta \gamma_{n+1}^a} = \frac{-H^a}{H^i} \left[\hat{\mathbf{m}}_{n+1} - \frac{(r - r^i)}{\|\mathbf{n}_{n+1}\|} (\mathbb{I} - \hat{\mathbf{n}}_{n+1} \otimes \hat{\mathbf{n}}_{n+1}) : \hat{\mathbf{m}}_{n+1} \right] : \hat{\mathbf{m}}_{n+1} \quad (4.40)$$

Substituting Equation 4.40 and Equation 4.39 into Equation 4.38.

$$\begin{aligned} \frac{\partial f_{n+1}}{\partial (\Delta \gamma_{n+1}^a)} (\Delta \gamma_{n+1}^a) &= [-2\mu + H^a (\hat{\mathbf{m}}_{n+1} : \hat{\mathbf{n}}_{n+1})] \\ &- 2\mu \sum_{i=1}^{a-1} \frac{H^a}{H^i} \left[(\hat{\mathbf{m}}_{n+1}^i : \hat{\mathbf{m}}_{n+1}) - \frac{(r - r^i)}{\|\mathbf{n}_{n+1}\|} \hat{\mathbf{m}}_{n+1}^i : (\mathbb{I} - \hat{\mathbf{n}}_{n+1} \otimes \hat{\mathbf{n}}_{n+1}) : \hat{\mathbf{m}}_{n+1} \right]. \end{aligned} \quad (4.41)$$

The final stress and the strain can be obtained, when $\Delta \gamma_{n+1}^a$ is determined.

$$\Delta \boldsymbol{\varepsilon}^p = \Delta \gamma_{n+1} \hat{\mathbf{n}}_{n+1} \quad (4.42)$$

$$\boldsymbol{\alpha}_{n+1}^a = \boldsymbol{\alpha}_n^a + H^a \Delta \gamma_{n+1}^a \hat{\mathbf{m}}_{n+1}^a \quad (4.43)$$

$$\boldsymbol{\sigma}_{n+1} = \boldsymbol{\alpha}_n + r \hat{\mathbf{n}}_{n+1} \quad (4.44)$$

For all the inner surfaces, the back-stress tensor can be obtained via

$$\boldsymbol{\alpha}_{n+1}^i = \boldsymbol{\alpha}_{n+1}^a - (r - r^i) \hat{\mathbf{n}}_{n+1}. \quad (4.45)$$

Therefore, the full stress tensor is

$$\boldsymbol{\sigma}_{n+1}^f = \boldsymbol{\sigma}_{n+1} + \kappa \left(\boldsymbol{\varepsilon}_{n+1}^f : \mathbf{I} \right) \mathbf{I}. \quad (4.46)$$

The Figure 4.2 shows the flowchart of Mroz's translation rule.

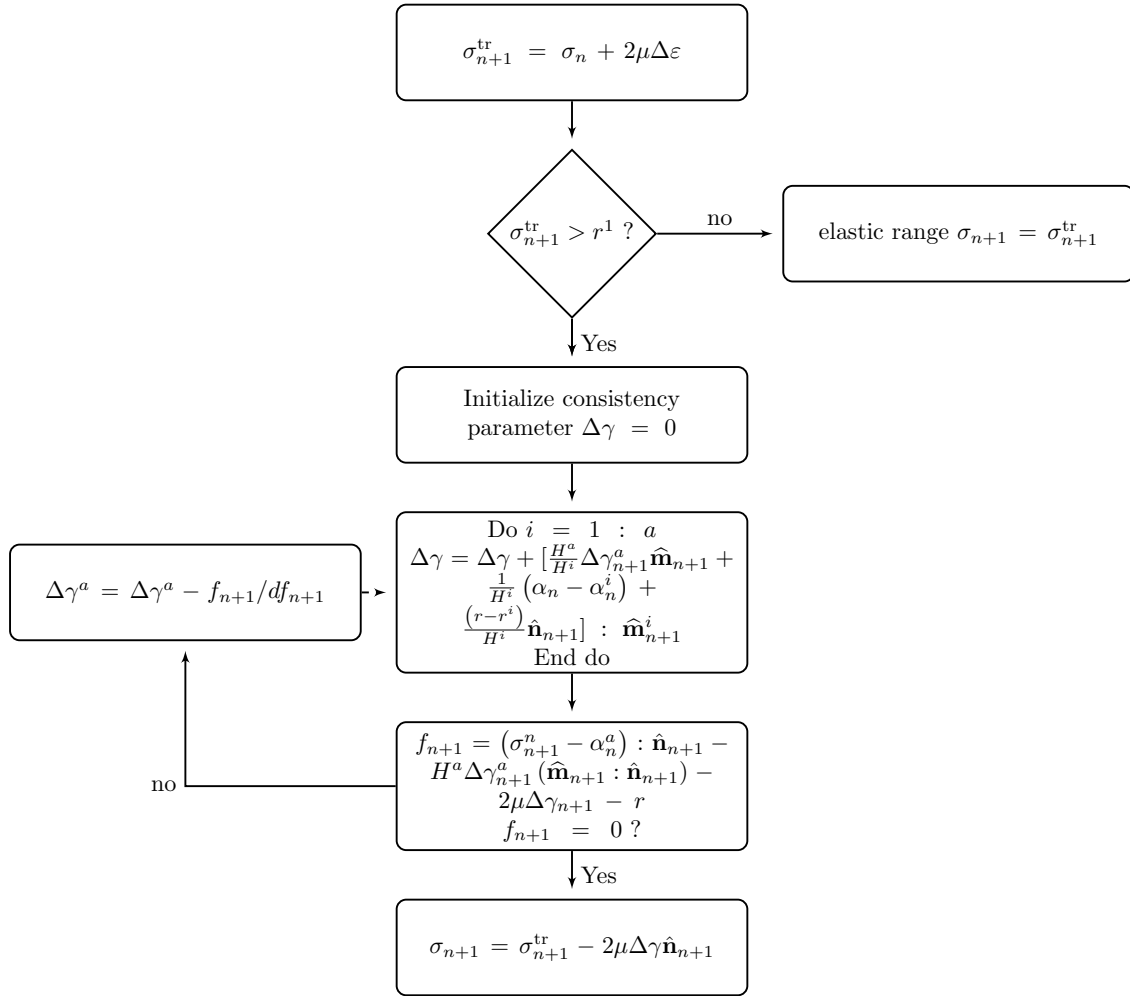


Figure 4.2: Flowchart of multi-surface plasticity model

4.3 ABAQUS User-defined Element (UEL) Implementation

In this study, the macroelement models adopting Mroz’s translation rule are implemented in ABAQUS [87] as a User-defined Element (UEL). The substantial advantage of the multilayer plasticity model is the multi-axial coupling behavior. Therefore, the 2D omnidirectional model includes multi-axial coupling behavior automatically. This omnidirectional element has two nodes, and each node has two degrees of freedom, which means the omnidirectional element can be stretched and compressed in a plane. Assuming the omnidirectional element is in the horizontal ($x-z$) plane, the displacements and internal forces are represented by the shear strains (τ_{12} , τ_{23}) and shear stresses (σ_{12} , σ_{23}) separately, since the shear deformation, is insusceptible to hydrostatic stress.

4.4 ABAQUS User-defined Element (UEL) Validation

In order to verify the omnidirectional spring element with Mroz’s translation rule, a uniaxial test is performed, since the monotonic tangent modulus associated with each surface can be obtained analytically from the following equation [55].

$$\frac{\Delta\sigma}{\Delta e} = \frac{1}{\frac{1}{2\mu} + \sum_{i=1}^a \frac{1}{H^i}} \quad (4.47)$$

A sinusoidal loading protocol (Figure 4.3 (a)) is prescribed the omnidirectional model in γ_{12} direction. The parameters utilized in the uniaxial test are listed in Table 4.1. Figure 4.3 demonstrates the difference between Mroz’s translation rule and theoretical curve, which was obtained from Equation 4.47. It can be seen that the omnidirectional models utilizing Mroz’s translations rules agree with the theoretic curve very well. This result indicates the algorithms converged, since Mroz’s translation rule produced the same response as the theoretical value under the uniaxial loading scenario.

In order to validate the omnidirectional model, controlled and uncontrolled-displacement experiments of the TFP bearing conducted at the UC Berkeley by Becker and Mahin [5]

Table 4.1: Discretization utilized for the uniaxial test.

Number of surfaces	Radii	Hardening moduli
i	r^i (kPa)	H^i (kPa)
1	6	50000
2	10	30000
3	15	10000
4	25	5000
5	40	1000
6	70	400
7	100	100
8	120	1

Shear modulus $\mu = 60000$ (kPa)

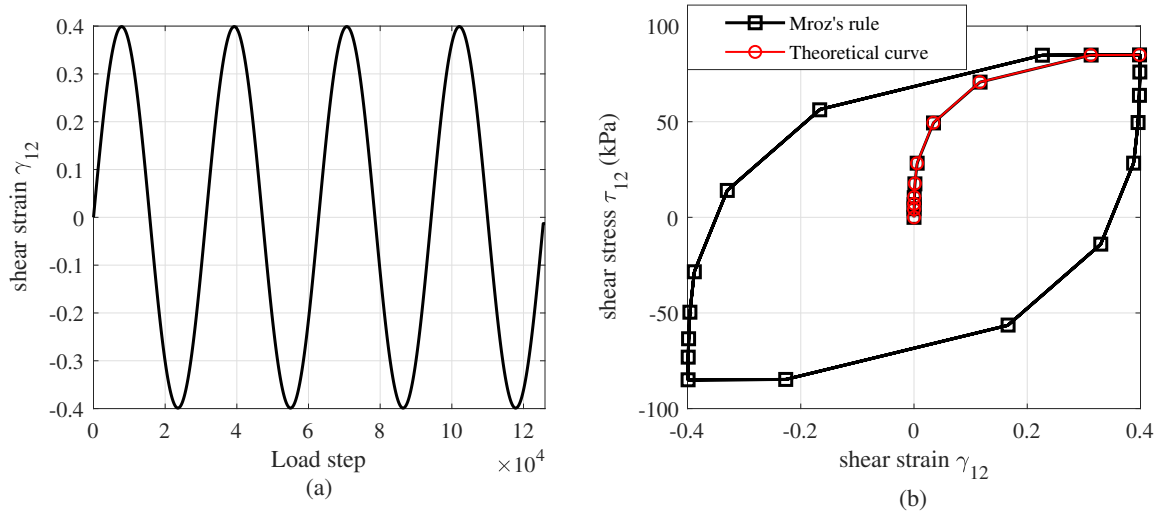


Figure 4.3: The uniaxial behavior of multisurface plasticity models under sine wave (a) using Mroz's translation rule (b).

are utilized again as the target response hysteresis. In this study, a simplified version of the omnidirectional model is proposed to simulate the TFP response. There are several reasons for using a simplified omnidirectional model rather than employing the original omnidirectional model. Firstly, in every loading step during the experiment, the relative movement in the TFP bearing happens in one particular sliding surface, which means only the sliding surface will contribute to the reaction force. On the contrary, all the yield surfaces inside the current active surface contribute to the reaction force in the original omnidirectional model. In order to mitigate this issue, one solution is to vanish the first yield surface from the original model when the displacement reaches the limit of the second yield surface (Figure 4.4). Therefore, when the displacement exceeds the second yield surface limit, only the second yield surface contributes to the reaction force.

Additionally, the transition region from the first phase to the second phase in TFP bearing is insignificant compared to the third phase, which plays the dominant role in the base-isolated building design. Besides, the experiment results indicate that the transition region from the first phase to the second phase is not pronounced, which agrees with the simplified omnidirectional model. Moreover, this simplification makes this model much more robust and efficient since only two surfaces are active at most in one step, which reduces the number of iterations. Note that the target surface radius must be smaller than twice the current active surface radius [56]. Some TFP geometry can violate this restriction in Mroz's translation rule.

Four controlled-displacement loading protocols and one controlled-acceleration orbit are adopted to compare the experimental with the omnidirectional model results—namely, the sine waves, circular, eight-shaped, square-shaped, and the Kobe @ JMA earthquake. The input variables (Table 4.2) of the omnidirectional model are calibrated from the TFP bearings' response under uniaxial sine wave.

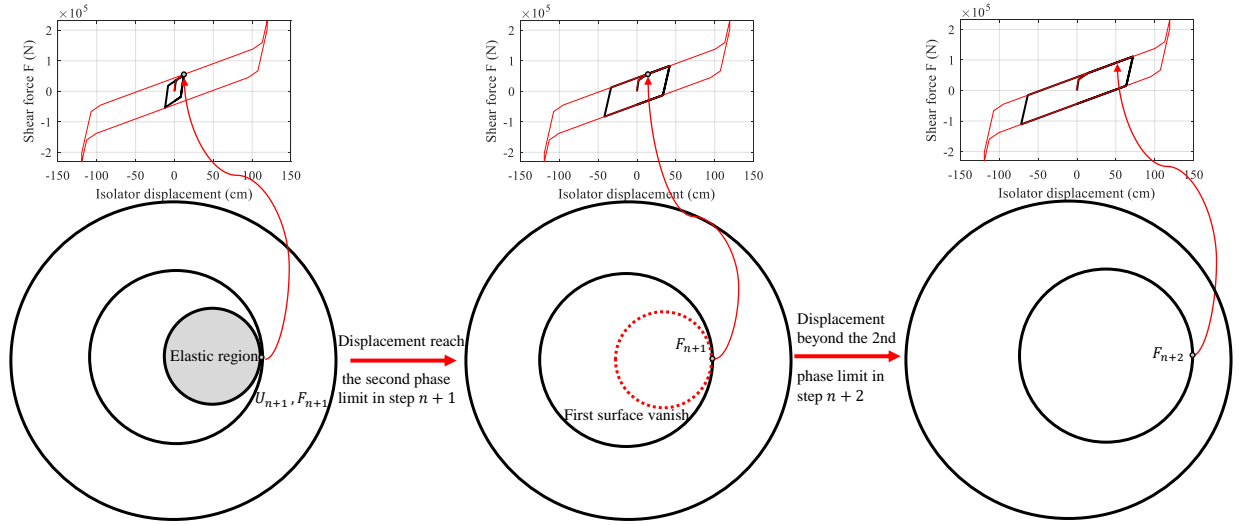


Figure 4.4: The simplified omnidirectional model.

Table 4.2: Parameters calibrated from the uniaxial sine wave test.

Number of surfaces	Normalized Radii	Normalized Hardening moduli
i	$r^i (\times 10^{-5})$	$H^i (\times 10^{-5})$
1	5448	23013
2	15726	1757
3	33305	586

Normalized Shear modulus $\mu = 1.671$

Poisson's ratio $\nu = 0.3$

4.4.1 Unidirectional Sine Wave Displacement Orbit

Figure 4.5 (a) presents the loading path of the sine wave. Figure 4.5 (b) demonstrates that both simplified and original omnidirectional models agree with the experimental response very well; the difference between them is negligible, which is verified by the energy dissipation per close loading cycle (Figure 4.5 (c)). Therefore, this simplification is validated; for convenience, the omnidirectional will represent the simplified omnidirectional in the following discussion.

4.4.2 Circular Displacement Orbit

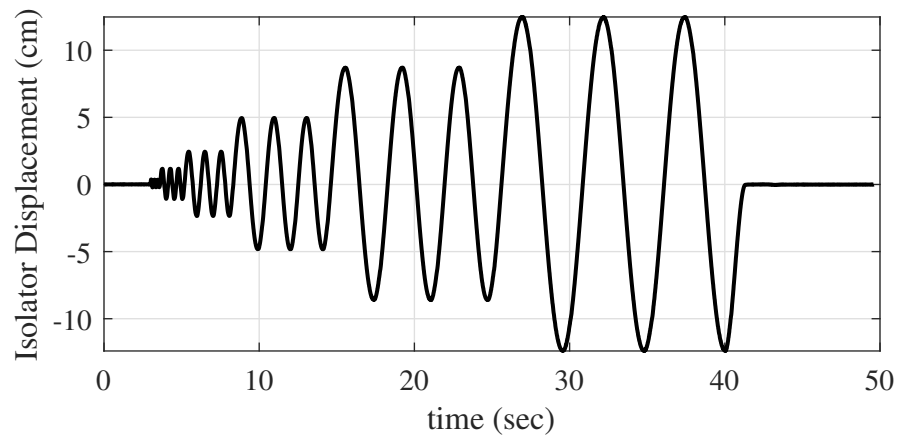
Figure 4.6 demonstrates the circular displacement orbits (a), reaction force relationship in two horizontal directions (b), and their corresponding hysteresis (c)(d). It is seen that the omnidirectional model predicts the hysteresis quite accurately, especially for maximum normalized shear force. However, the prediction sometimes underestimates the reaction, probably due to sacrificing the second phase after the total displacement beyond the second phase displacement limitation.

4.4.3 Eight-Shaped Displacement Orbit

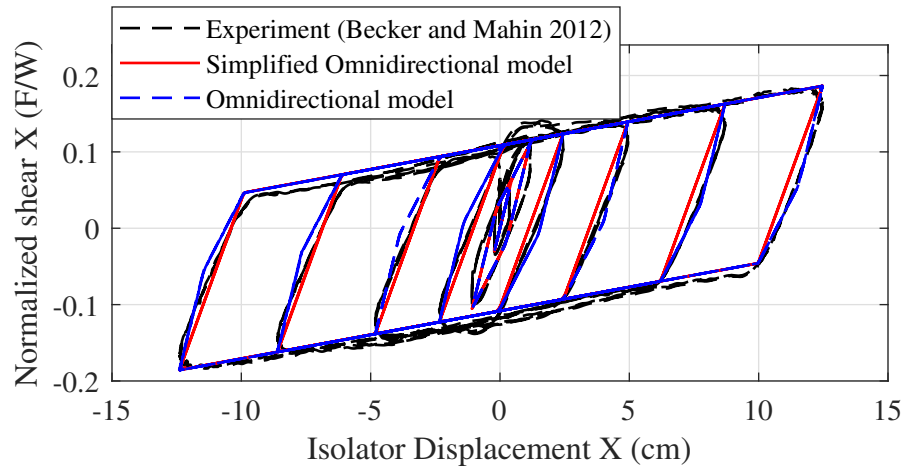
As one can see, Figure 4.7 demonstrates that the omnidirectional model predicts the hysteresis of TFP bearings precisely, even under the challenging eight-shaped displacement orbit. These results endorse that the omnidirectional model can predict the hysteresis of TFP bearings effectively and accurately.

4.4.4 Square-Shaped Displacement Orbit

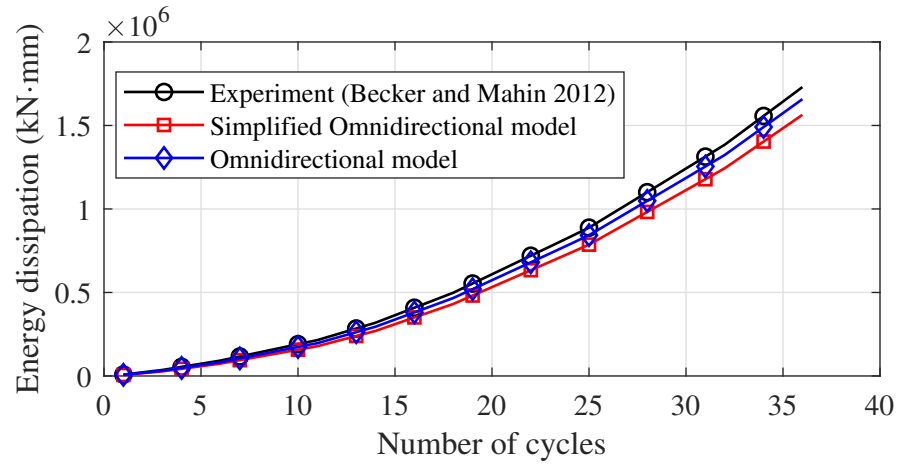
Figure 4.8 indicates that the omnidirectional model is able to capture the trend of the hysteresis of TFP bearings. The reaction forces are sometimes underestimated in one direction,



(a)



(b)



(c)

Figure 4.5: Isolator displacement time-history (a), hysteresis (b), and energy dissipation (c).

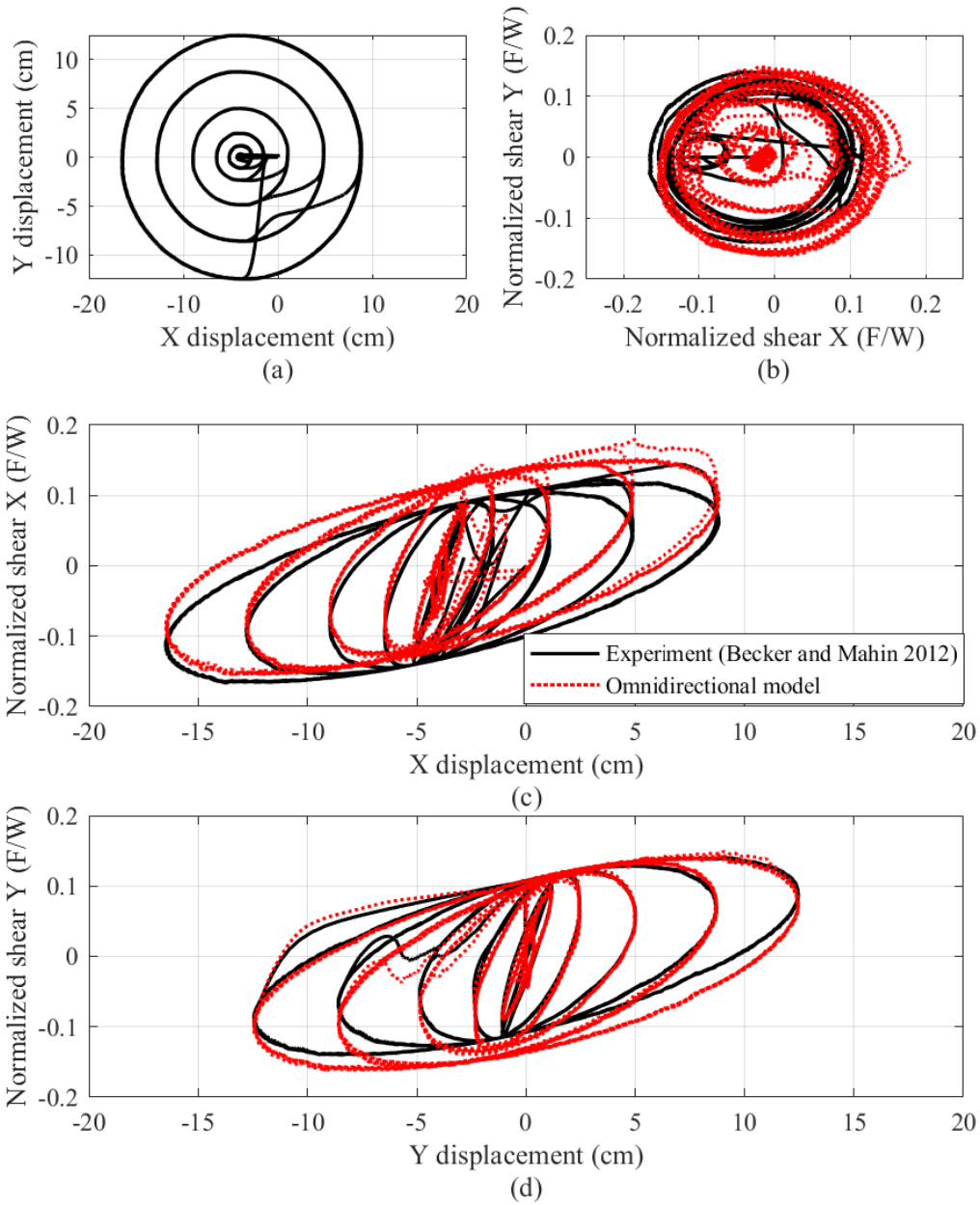


Figure 4.6: TFP bearings hysteresis for the circular displacement orbit.

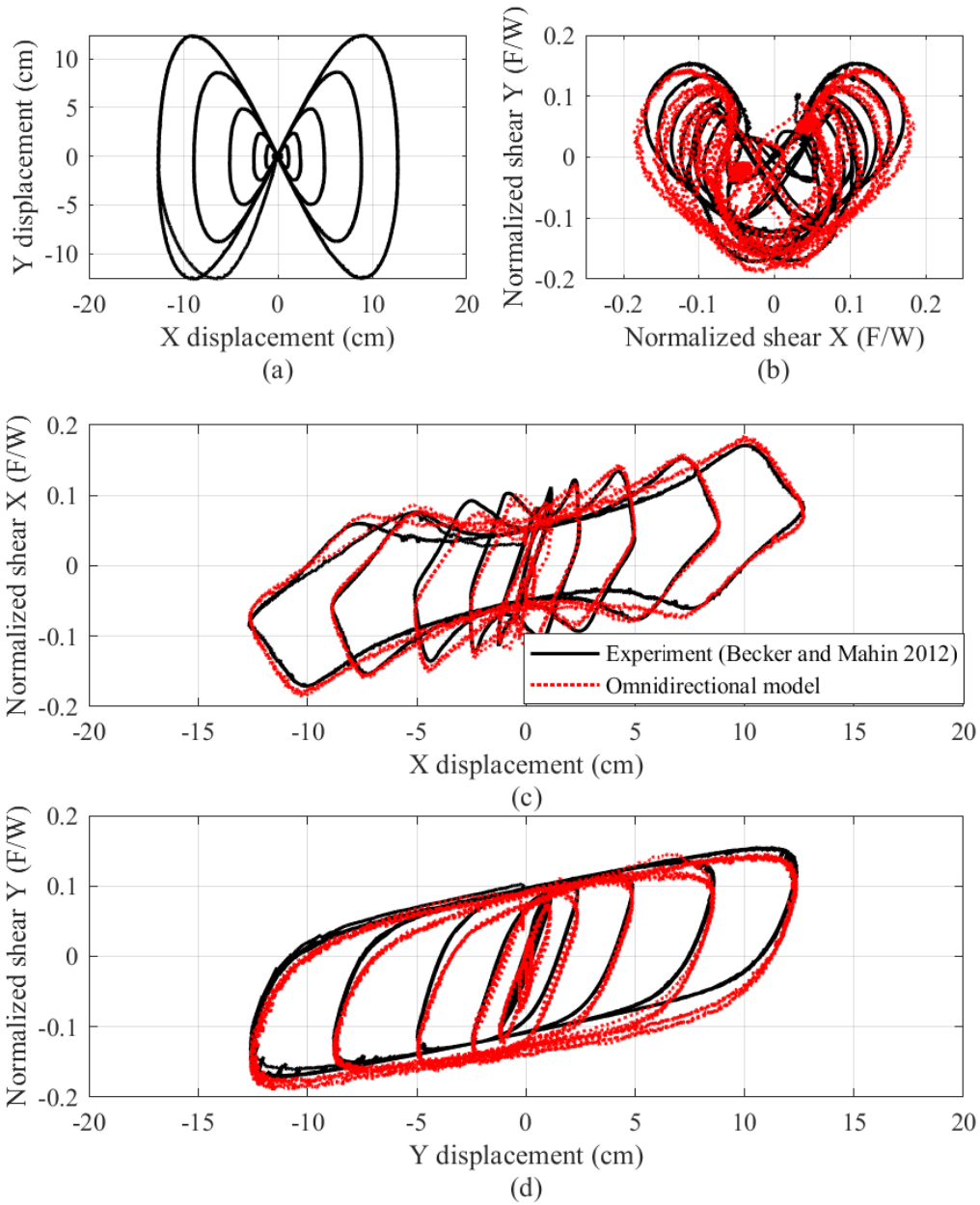


Figure 4.7: TFP bearings hysteresis for the eight-shaped displacement orbit.

probably due to the abrupt change in the displacement history. Therefore, shrink the increment size during analysis can mitigate this problem.

4.4.5 Uncontrolled Displacement Orbit

Earthquake excitation is the most challenging and significant test for the numerical model; in order to validate the omnidirectional model, the acceleration history of the Kobe @ JMA earthquake is applied (Figure 4.9 (a)). The displacement orbit is shown in Figure 4.9 (b). Figure 4.9 (c) and (d) compare the hysteresis between the experiment and the numerical model. The result indicates that the numerical model's prediction is promising, since it demonstrates the capability to accurately capture the trend of TFP bearings' responses.

By comparing the omnidirectional model with experiment results utilizing these four sets of hysteresis, this omnidirectional model is validated and indicates its ability to predict TFP bearings' response under complex conditions.

4.5 An Application of the Omnidirectional Model: Dynamic Analysis of a Prototype Base-Isolated Building.

This section demonstrates an application of the omnidirectional model in base-isolated building design and compares it with the corresponding fixed-based building and base-isolated building adopting the unidirectional model.

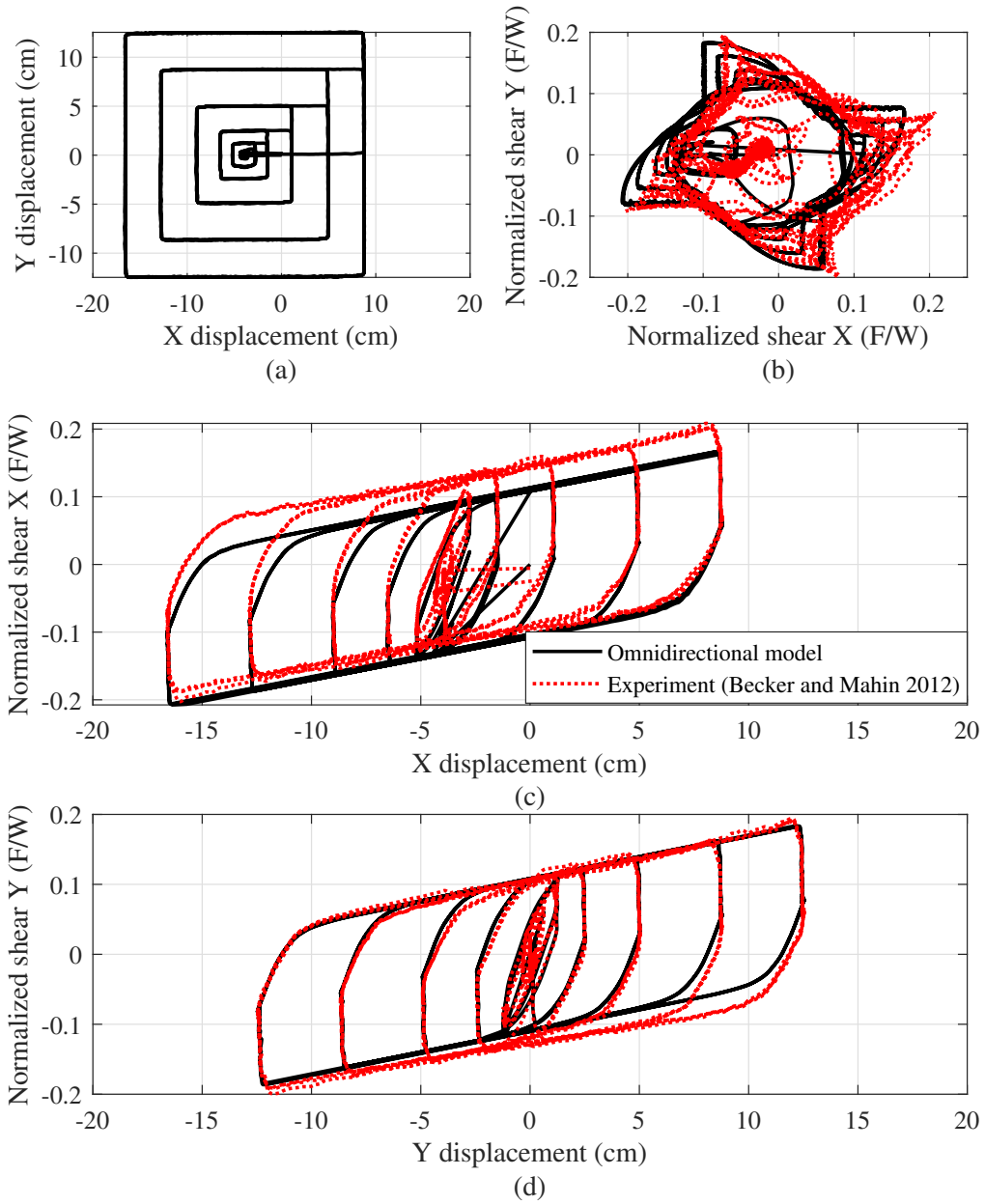


Figure 4.8: TFP bearings hysteresis for the square-shaped displacement orbit.

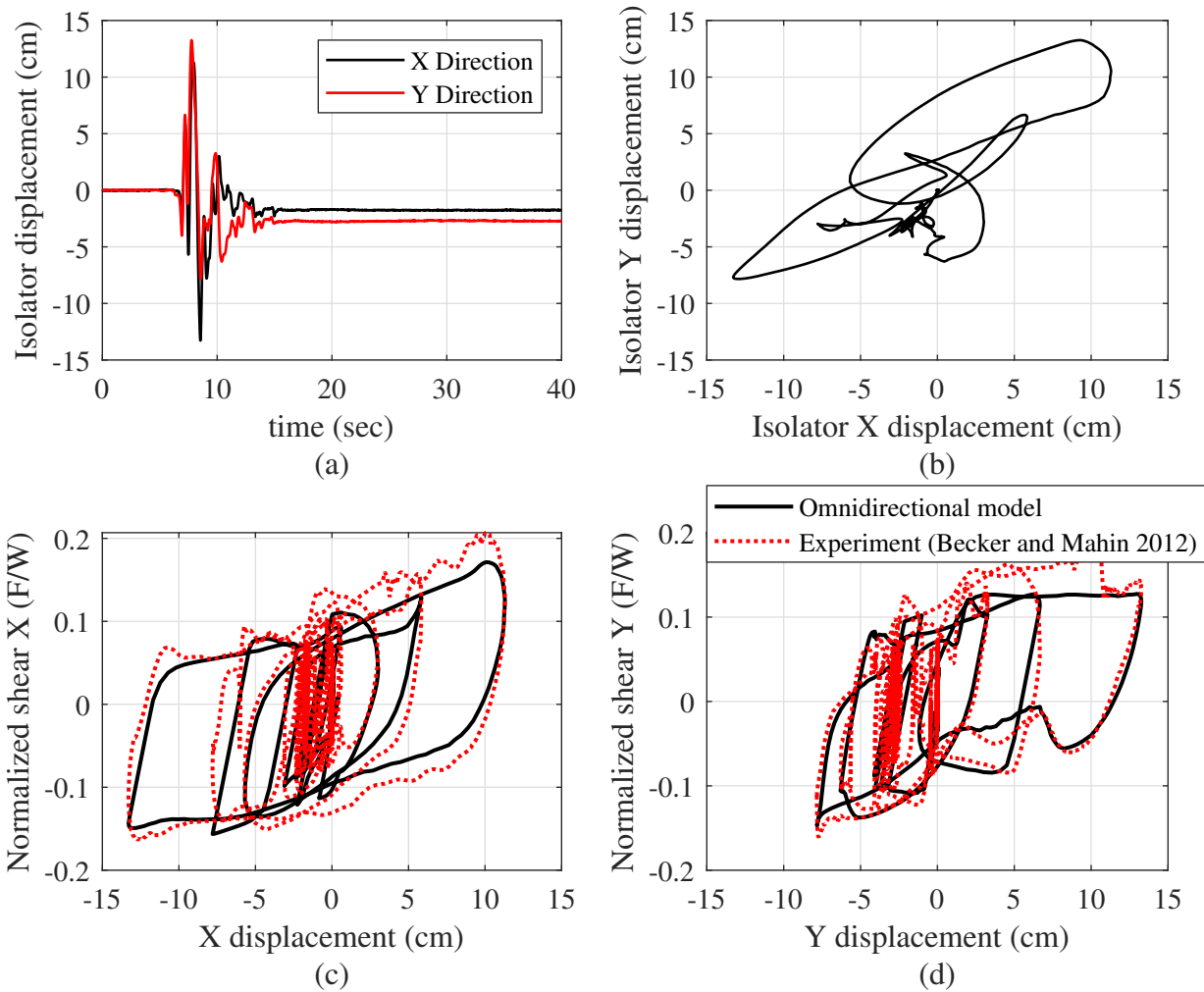


Figure 4.9: TFP bearings displacement history, orbit and hysteresis from response to the Kobe @ JMA earthquake record.

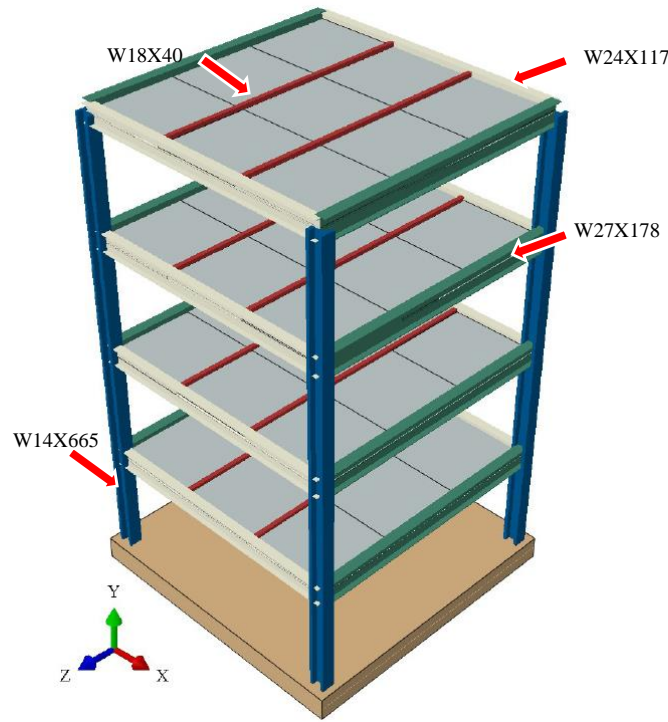


Figure 4.10: 3D view of the ABAQUS model.

4.5.1 The Prototype Building Geometry and Loads

A prototype model of a 4-story building consisting of one bay in both orthogonal directions (9×9 m) was created in ABAQUS CAE (Figure 4.10). The floor-to-floor height of all four levels is 4 meters. The columns and beams were modeled as B31 elements (2-node linear beam in space). All the connections of the moment frame system are modeled as fixed connections. The floor system and the foundation are considered rigid diaphragms with the concrete slab of 0.1 m and 0.8 m depth separately, modeled as S4 elements (4-node general-purpose shell element). The roof loads include the ground snow load of 957 N/m^2 ; floor loads include the dead load of 2400 N/m^2 and the live load of 2400 N/m^2 . Only self-weight and superimposed dead loads are accounted for as the seismic mass in the dynamic analysis.

Table 4.3: The selected earthquake records.

Record No.	Event (abbreviation)	Year	Station	Magnitude (M_w)
1	Imperial Valley-06 (IV)	1979	Delta	6.53
2	Superstition Hills-02 (SH)	1987	El Centro	6.54
3	Landers (L)	1992	Yermo Fire Station	7.28
4	Kobe-Japan (KJ)	1995	Abeno	6.9
5	Duzce-Turkey (DT)	1999	Duzce	7.14
6	Darfield-New Zealand (DNZ)	2010	GDLC	7.0
7	Chi-Chi-Taiwan (CCT)	1999	TCU076	7.62

4.5.2 Ground Motion Selection

The structural system of the building was designed following the provisions of ASCE 7-16 [2]. The prototype building is assumed to be located in Los Angeles. Therefore, the USGS worldwide seismic design tool can obtain the mapped acceleration parameters $S_S = 2.01$ g, $S_1 = 0.74$ g, and $T_L = 8$ sec. Thereafter, per ASCE 7-16 [2], a minimum of 7 earthquake records are required to perform the time history analysis (Table 4.3). Acceleration response spectrum curves for MCE scenario earthquake records are presented in Figure 4.11, where the selected earthquake records are matched with MCE fault normal (Figure 4.11 (a)) and MCE fault parallel (Figure 4.11 (b)).

4.5.3 Design of the TFP Bearings

The geometry of the TFP bearings (Table 4.4) is selected based on chapters 12 and 17 structural performance requirements, seismic hazard, and design requirements stated in ASCE 7-16 [2]. After that, the parameters utilized in the omnidirectional model are estimated

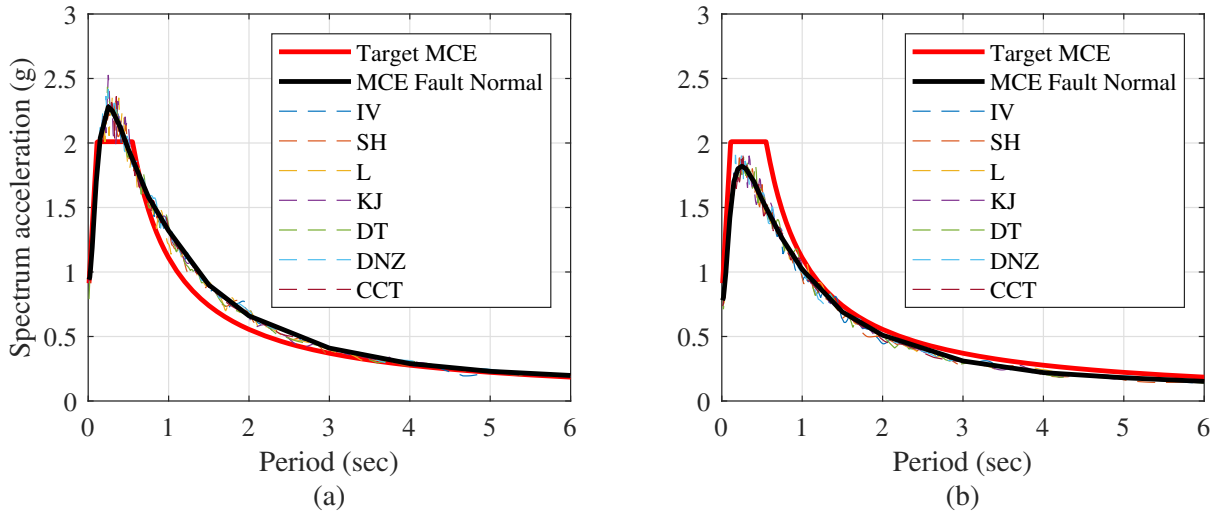


Figure 4.11: Acceleration response spectrum curves for MCE scenario earthquake records: Fault Normal (a), Fault Parallel (b).

based on the selected TFP bearings' geometry. The theoretical backbone curve and the omnidirectional model are shown in Figure 4.12.

4.5.4 Dynamic Analysis Results

After performing the dynamic nonlinear history analysis, the displacement orbit, hysteresis repose, and energy dissipation of the TFP bearings under Chi-Chi @ TCU076 earthquake

Table 4.4: The geometry parameter of the TFP bearing.

Nominal Friction Coefficient		Radius (cm)		Height (cm)	
μ_1	0.05	R_1	396.24	h_1	13.97
μ_2	0.02	R_2	40.64	h_2	8.89
μ_3	0.02	R_3	40.64	h_3	8.89
μ_4	0.08	R_4	396.24	h_4	13.97

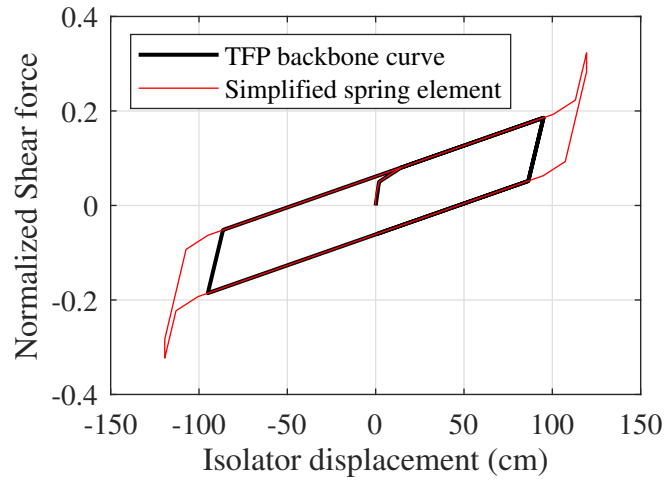


Figure 4.12: The TFP backbone curve and the omnidirectional model.

excitations are shown in Figure 4.13, the TFP bearing response under the other six earthquakes are listed in Appendix 7.2. These results indicate that base isolation is effective in reducing the base shear under earthquakes with different intensities. The omnidirectional model produces 94% and 12.5% less normalized shear force than the fixed-based building and unidirectional model on average (Table. 4.5), separately. Similarly, compared to the fixed-based building, the maximum story drift (Table. 4.6) and acceleration (Table. 4.7) are reduced 93% and 94% separately when the omnidirectional model is employed. As expected, the unidirectional model has an 8% larger story drift and 18% larger acceleration than the omnidirectional model, since the biaxial coupling effect is not considered. The hysteresis responses estimated by the omnidirectional model agree with the design backbone curve very well. The difference between the omnidirectional and unidirectional model predictions indicates that the bi-axial coupling effect is essential. The normalized base shear predicted by the unidirectional model is higher than the omnidirectional model in all the cases, since the bi-axial coupling effect 'reduce' the shear stiffness. In general, the unidirectional model dissipates slightly more energy than the omnidirectional model. Therefore, the unidirectional model, currently widely used in practical design, can not accurately represent the bi-axial coupling effect; this issue can be addressed by adopting the omnidirectional model, which

Table 4.5: Max. normalized base shear under earthquake.

Earthquake event	Max. base shear (normalized by seismic weight) of fix-based building (%)	Max. base shear (nor- malized by seismic weight) of base-isolated building utilizing om- nidirectional model (%)	Max. base shear (nor- malized by seismic weight) of base-isolated building utilizing unidi- rectional model (%)
Imperial Valley-06	246	11	14
Superstition Hills-02	211	13	15
Landers	191	17	17
Kobe	225	12	13
Duzce	228	13	14
Darfield	215	16	18
Chi Chi	223	15	19
Mean	220	14	16
Median	223	13	15

provides a more robust solution. In addition, Figure 4.14 shows the difference between the unidirectional model and the omnidirectional model in terms of the acceleration and the influence of the uncoupled macroelement model orientation selection. Similarly, the prediction of maximum normalized based shear also depends on the orientation of the uncoupled macroelement model because of the misrepresenting the circular yield surface; the details are shown in Table 4.8.

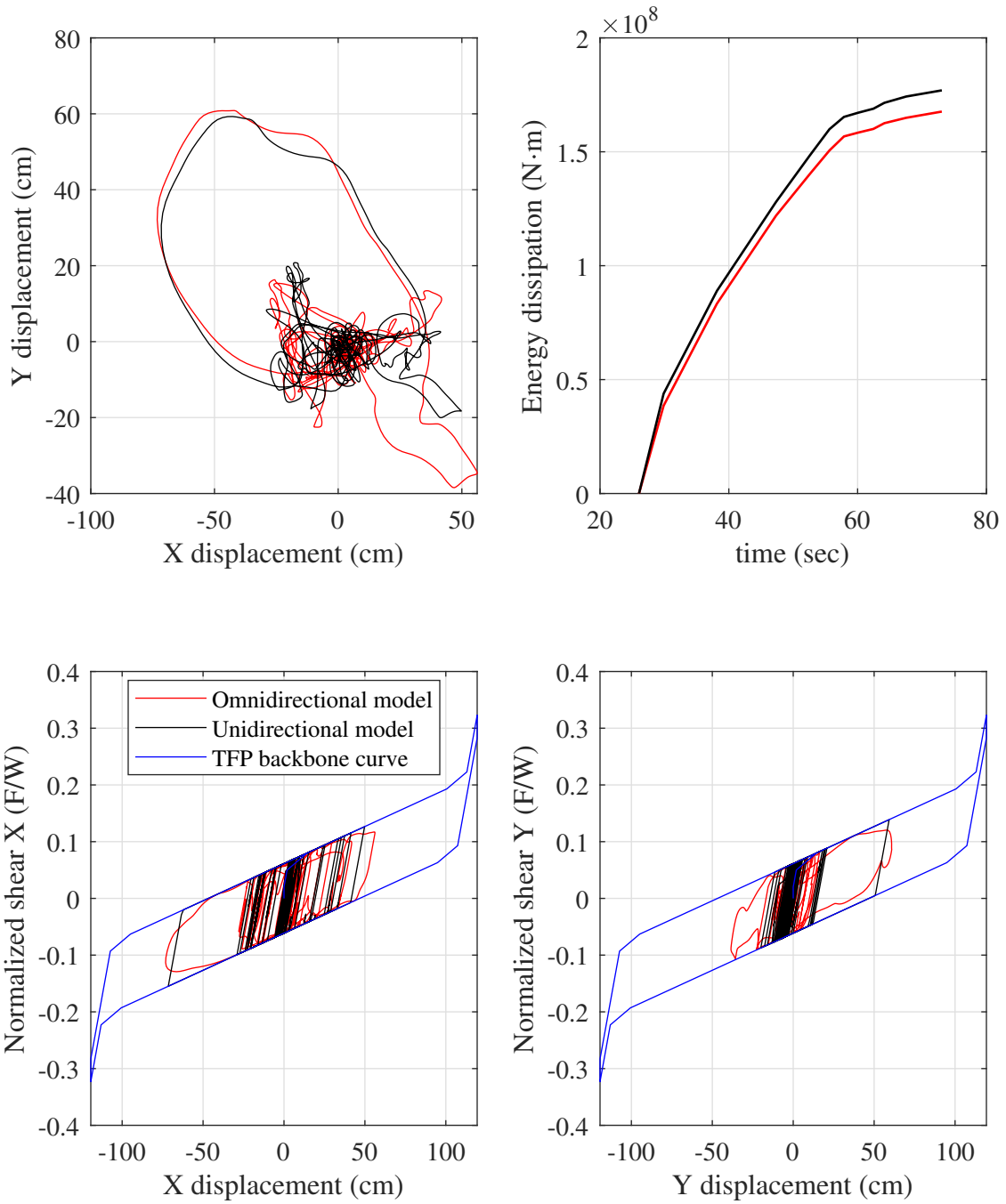


Figure 4.13: Displacement orbit of Chi-Chi @ TCU076 earthquake (a), energy dissipation (b) and hysteresis of the TFP bearings (c)(d).

Table 4.6: Max. story drift under earthquake.

Earthquake event	Max. inter-story drift of fixed based building (%)	Max. inter-story drift of base-isolated building utilizing omnidirectional model (%)	Max. inter-story drift of base-isolated building utilizing unidirectional model (%)
Imperial Valley-06	1.85	0.09	0.11
Superstition Hills-02	1.54	0.10	0.12
Landers	1.48	0.13	0.13
Kobe	1.35	0.08	0.10
Duzce	1.74	0.12	0.13
Darfield	1.89	0.13	0.14
Chi Chi	1.86	0.12	0.13
Mean	1.67	0.11	0.12
Median	1.74	0.12	0.13

Table 4.7: Max. acceleration under earthquake.

Earthquake event	Max. floor acceleration of fix-based building (g)	Max. floor acceleration of base-isolated building utilizing omnidirectional elements (g)	Max. floor acceleration of base-isolated building utilizing unidirectional elements (g)
Imperial Valley-06	4.27	0.22	0.28
Superstition Hills-02	3.76	0.24	0.26
Landers	3.07	0.22	0.28
Kobe	4.02	0.21	0.27
Duzce	3.79	0.22	0.28
Darfield	3.65	0.22	0.28
Chi Chi	3.81	0.29	0.31
Mean	3.77	0.23	0.28
Median	3.81	0.22	0.28

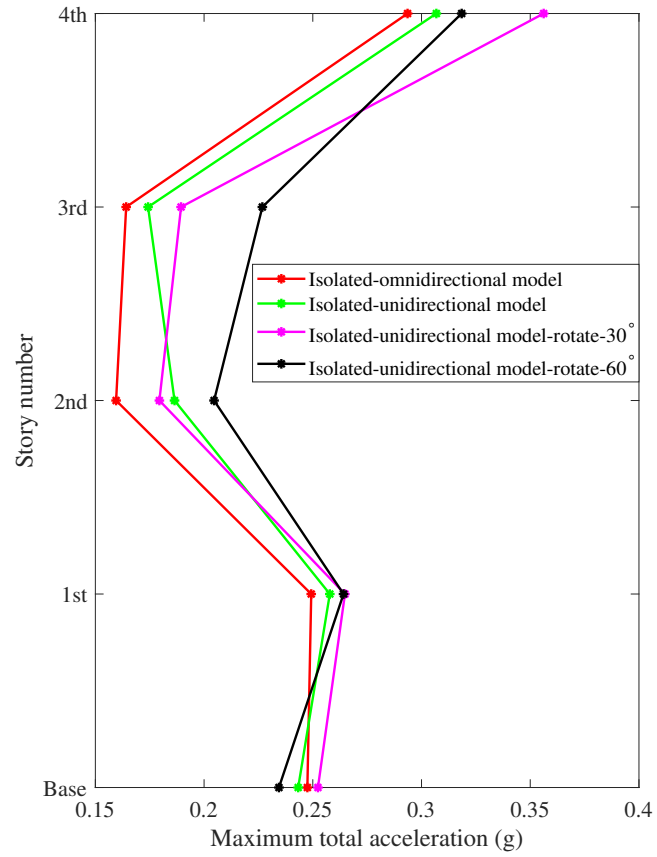


Figure 4.14: Max. normalized base shear under Chi-Chi @ TCU076 earthquakes with different orientations of the unidirectional model and the omnidirectional model.

Table 4.8: Max. normalized base shear under earthquakes with different orientations of the uncoupled macroelement model.

Earthquake event	Building utilizing uncoupled macroelement model		
	rotate 0°	rotate 30°	rotate 60°
Imperial Valley-06	13.8%	14.7%	14.6%
Superstition Hills-02	14.6%	13.5%	14.8%
Landers	17.2%	16.8%	17.9%
Kobe	12.7%	14.7%	14.6%
Duzce	13.8%	15.2%	14.5%
Darfield	17.7%	16.8%	18.3%
Chi Chi	18.5%	17.8%	18.1%

CHAPTER 5

A Pressure-dependent Macroelement Modeling Approach for Hysteretic Response of TFP Bearings

In 1986, Lin and Tadjbakhsh [45] showed that both the horizontal reaction and displacement of a mass block isolated by friction pendulum bearings are magnified due to considering the vertical earthquake excitation. The similar results had been found by Calvi et al. [11] in 2004 and several analytical studies [78, 26, 66]. The increase of horizontal base shear and displacement will cause amplification of the floor acceleration of the superstructure, suggested by Rabiei and Khoushnoudian [70]. There is no experimental test that demonstrates the significance of the vertical earthquake excitation effect on the horizontal response of a base-isolated structure until 2016 proposed by Ryan and Dao [74], the importance of vertical earthquake excitation effect on the horizontal response of the superstructure was verified.

5.1 The Methodology of the Pressure-dependent Macroelement Model

As stated above, the vertical earthquake excitation affects the horizontal response of the superstructure significantly. However, the previous omnidirectional model for TFP bearings lacks pressure-dependent ability.

In the original omnidirectional element model, two nodes represent the TFP bearings' top and bottom separately. Each node has two degrees of freedom to simulate the horizontal X and Y axis. Currently, the newly introduced third degree of freedom incorporates the

vertical pressure effect by monitoring the vertical pressure of the top of the TFP bearings is introduced. Then the ratio η of the instantaneous pressure to the static pressure can be estimated through Equation 5.1. After that, the radius of each yield surface will be adjusted by Equation 5.2, which indicates that the yielding surface's radius changes proportionally to the normal pressure, except for the ultimate one. Figure 5.1 demonstrates the involvement of the yielding surfaces' radius. Therefore, the shape of yielding surfaces becomes from circles with constant radius to a cone shape (Figure 5.2).

$$\eta = \frac{P_{\text{instantaneous}}}{P_{\text{static}}} \quad (5.1)$$

$$r_{\text{new}}^i = \eta r^i, i = 1, 2, n - 1 \quad (5.2)$$

5.2 Validation of the Pressure-dependent Macroelement model

In 2011, a full-scale 5-story steel moment frame building with TFP bearings was tested at Hyogo Earthquake Engineering Research Center (E-Defense) of Miki, Japan [77]. The recorded displacement and forces history of TFP bearings are able to verify the pressure-dependent macroelement model.

The design parameters of TFP bearing used in the E-defense are shown in Table 5.1. The input parameters of the pressure-dependent macroelement model (Table 5.2) are obtained by the geometry of TFP bearings. Seven earthquake excitations plus one sine wave displacement orbit are utilized to verify the pressure-dependent macroelement model, which is listed in Table 5.3.

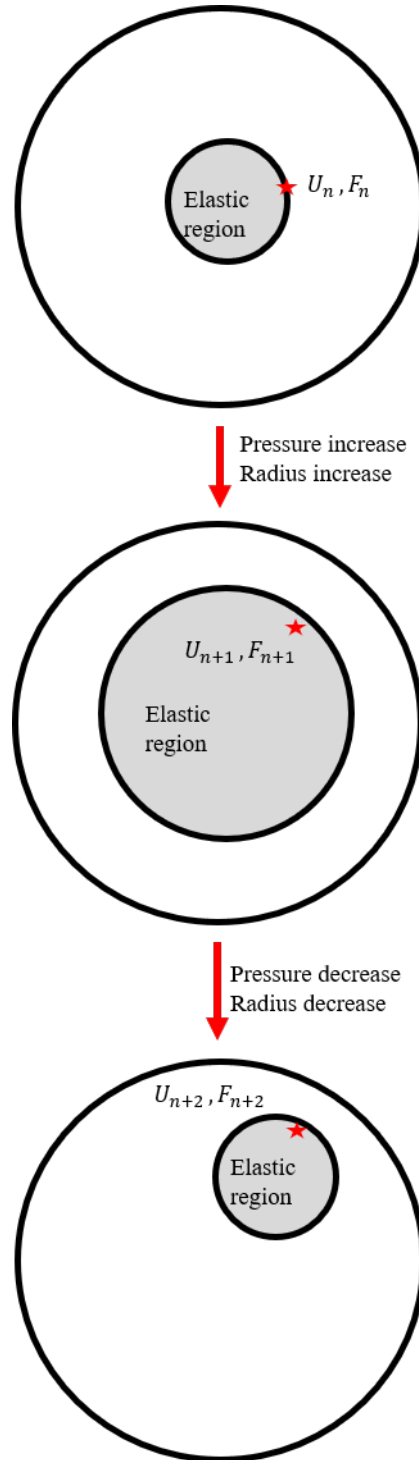


Figure 5.1: The pressure-dependent macroelement model.

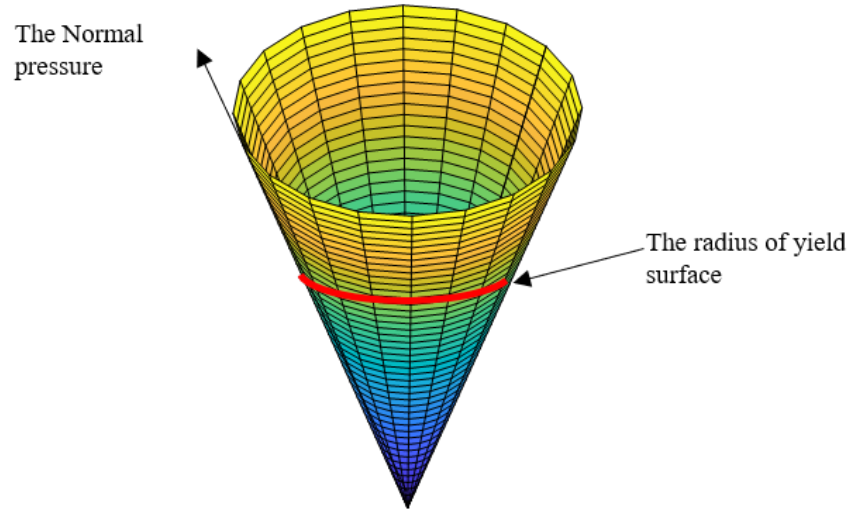


Figure 5.2: The cone shape yielding surfaces of the pressure-dependent macroelement model.

Table 5.1: Geometry of the TFP bearing used in the E-defense.

μ (%)	R (mm)	h (mm)	d (mm)
$\mu_1 = 0.02$	$R_1 = 457$	$h_1 = 38$	$d_1 = 51$
$\mu_1 = 0.08$	$R_2 = 3962$	$h_2 = 114$	$d_1 = 514$
$\mu_1 = 0.08$	$R_3 = 3962$	$h_3 = 114$	$d_1 = 514$

Table 5.2: Input parameters of the pressure-dependent macroelement model.

Number of surfaces	Normalized Radii	Normalized Hardening moduli
i	$r^i (\times 10^5)$	$H^i (\times 10^5)$
1	0.87	0.72
2	1.16	2.95
3	1.63	9.84

Normalized Shear modulus $\mu = 3.7 \times 10^4$

Poisson's ratio $\nu = 0.3$

Table 5.3: Earthquake excitations applied to the E-defense building.

Record No.	Earthquake/Station	Scale factor		
		X	Y	Z
1	1940 Imperial Valley @ El Centro	1.3	1.3	1.3
2	1994 Northridge @ Symlar Olive View Hosp.	1.0	1.0	1.0
3	1989 Loma Prieta @ Los Gatos Pres. Ctr.	0.7	0.7	0.7
4	2011 Tohoku @ Iwanuma	1.0	1.0	0.0
5	1995 Kobe @ Takatori	1.0	1.0	1.0
6	1999 ChiChi @ TCU065	0.8	0.8	0.0
7	1992 Tabas @ Tabas	1.0	1.0	0.0

5.2.1 Single Element Test

The vertical force histories were recorded for all excitation during the E-defense experiment. Therefore, the pressure-dependent macroelement can be tested without the superstructure by fixing one node (TFP bearing top) of the element and applying three-dimensional excitations on the other node (TFP bearing bottom).

The hysteresis of TFP bearings under sine wave is shown in Figure 5.3. Note that there is no vertical excitation applied under the sine wave test. The pressure-dependent macroelement model agrees with the experiment much better than the macroelement model because of incorporating the vertical pressure effect. Therefore, the sine wave test validated the effectiveness of the pressure-dependent macroelement model.

The hysteresis of TFP bearings under seven earthquake excitations are shown from Figure 5.4 to Figure 5.10. These results indicate that the pressure-dependent macroelement model predicts the hysteresis of the TFP bearing more accurately than the normal macroelement model, especially when the vertical excitation can not be ignored. Under real earthquake excitations, a huge amount of spikes of horizontal force are observed due to the abrupt change of the vertical forces. Therefore, the normal macroelement model can not capture those characteristics which are significant for TFP bearing design. Both maximum displacement and shear force obtained by the macroelement model are underestimated in most cases. In other words, the pressure-dependent macroelement model provides a more conservative result, which is good for structure design. Besides, the difference between the two numerical models is negligible when mild earthquakes are applied. However, the pressure-dependent macroelement model can capture the peak base shear and displacement of TFP bearing in huge earthquakes, but the macroelement model can not. This result also confirms that vertical earthquake excitation plays a significant role, especially in a big earthquake.

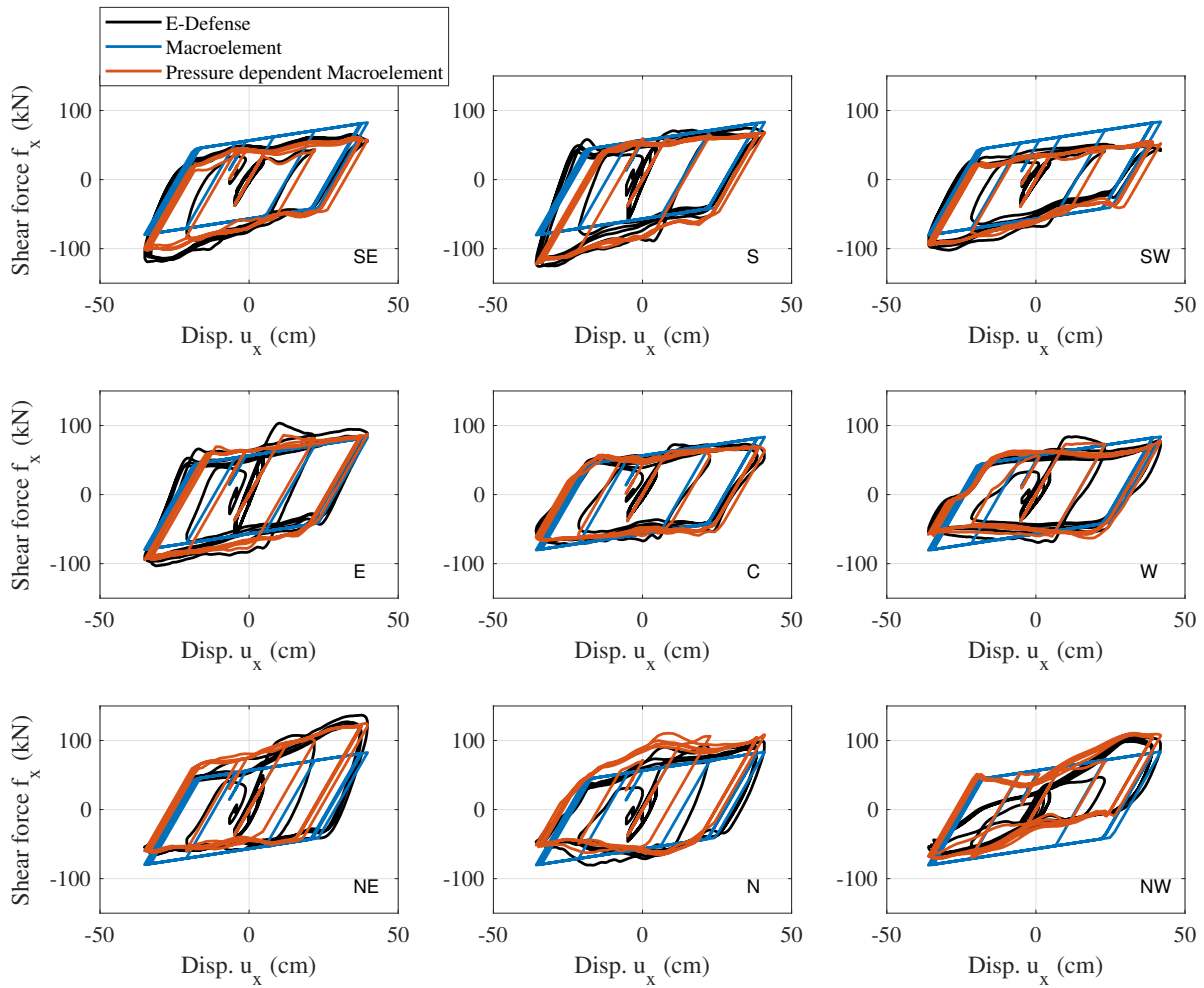


Figure 5.3: The hysteresis of TFP bearings under sine wave.

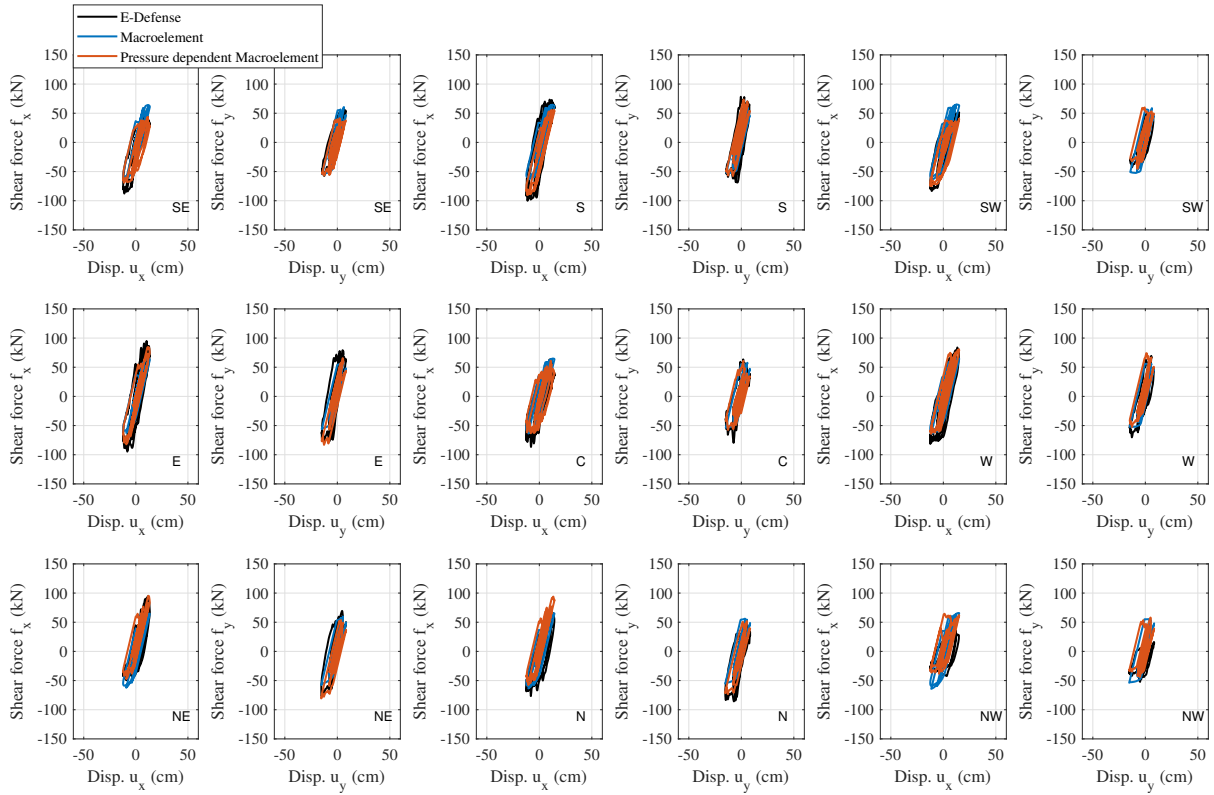


Figure 5.4: The hysteresis of TFP bearings under Imperial Valley @ Westmorland earthquake.

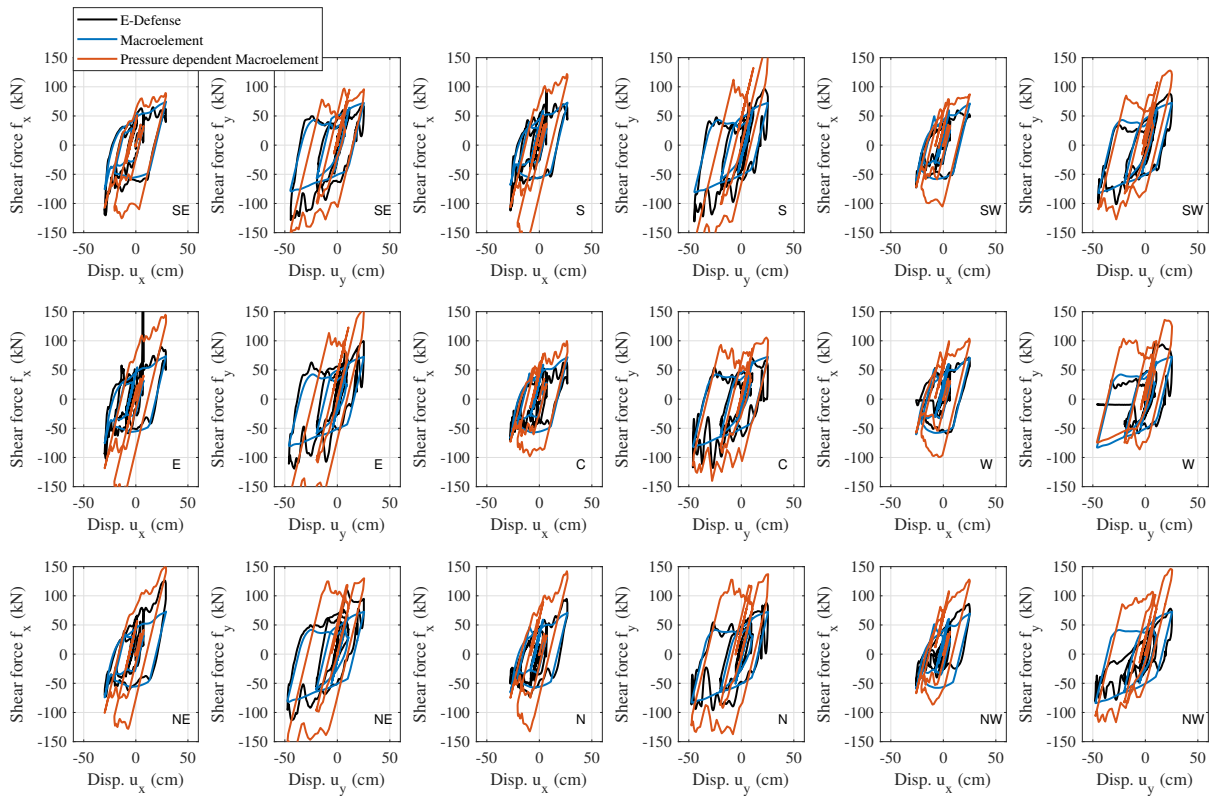


Figure 5.5: The hysteresis of TFP bearings under Northridge @ Sylmar earthquake.

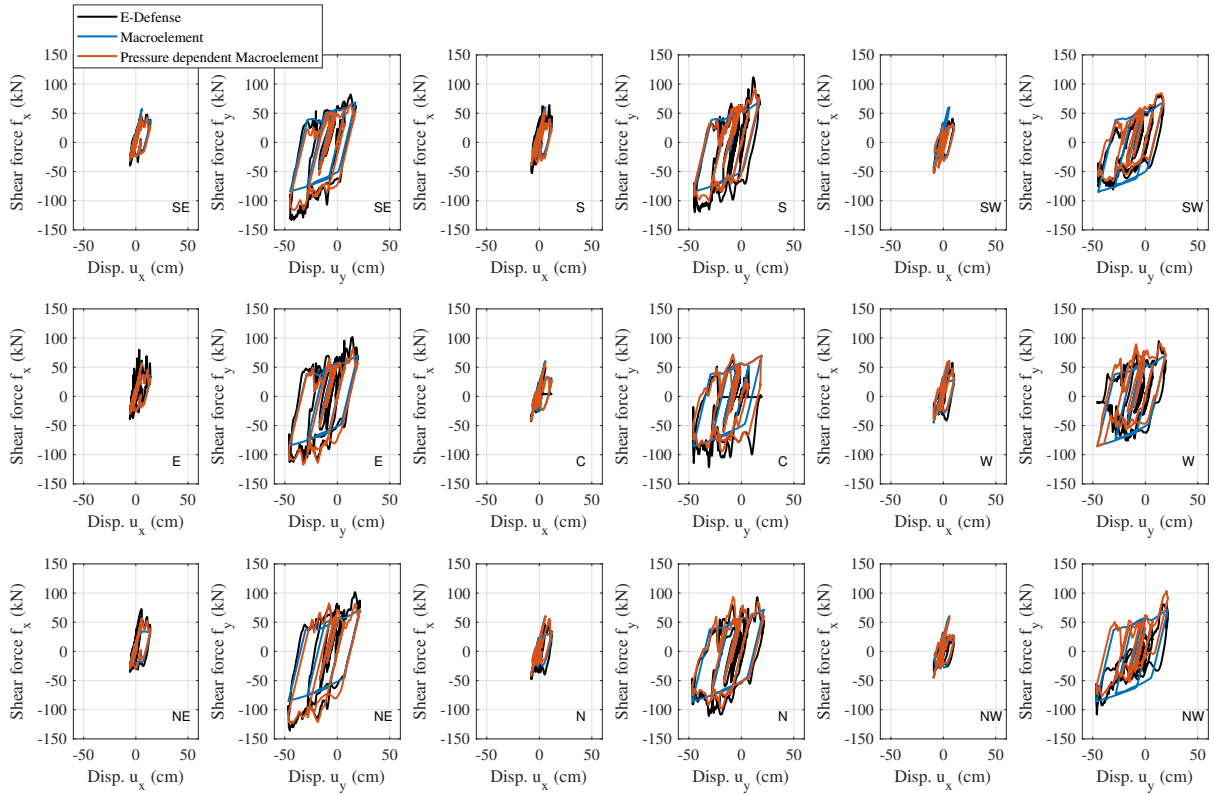


Figure 5.6: The hysteresis of TFP bearings under Loma Prieta @ Los Gatos Pres. Ctr. earthquake.

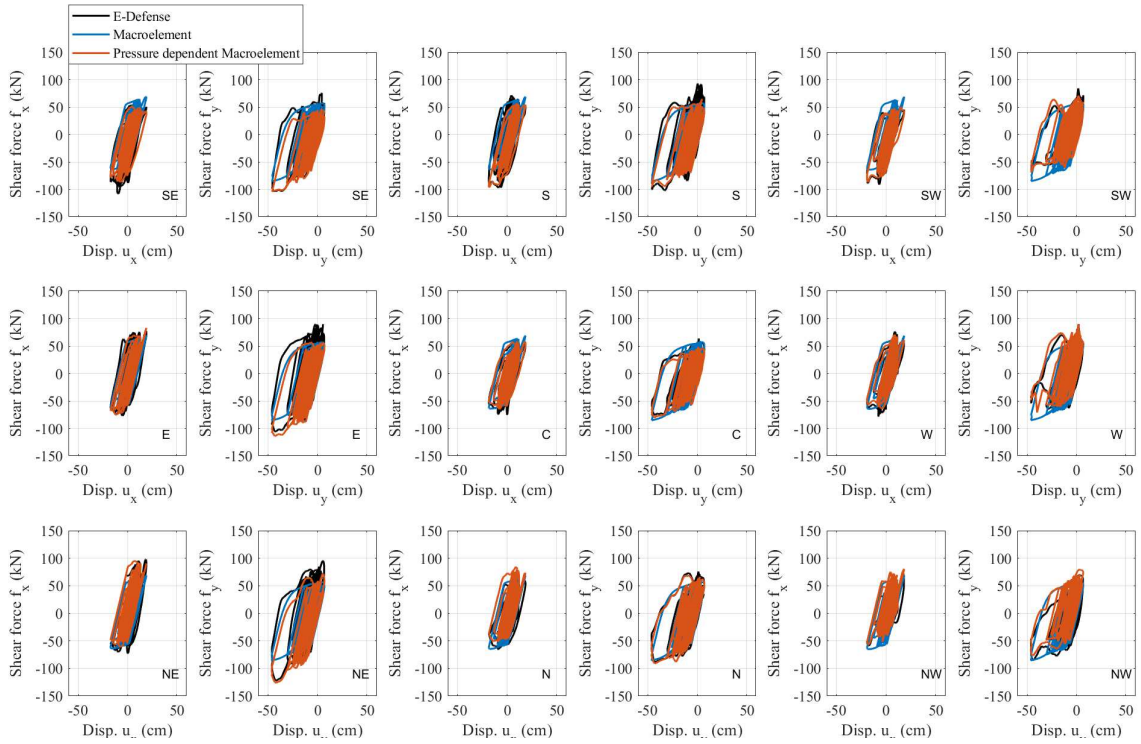


Figure 5.7: The hysteresis of TFP bearings under Tohoku @ Iwanuma earthquake.

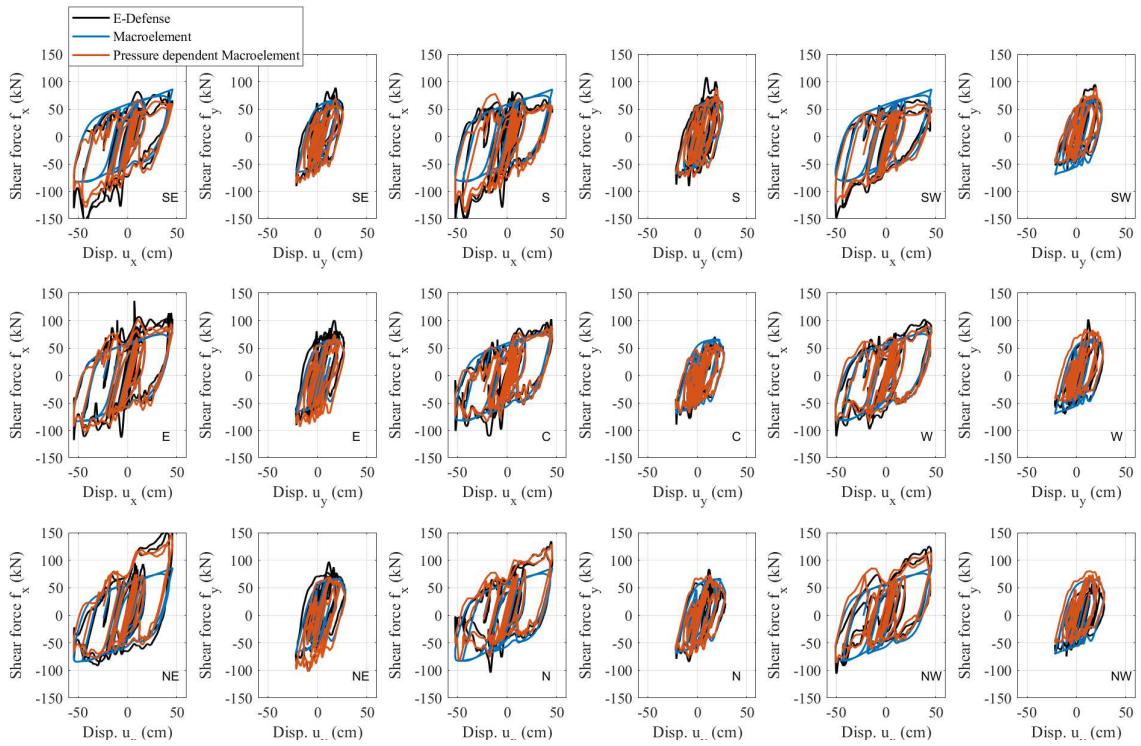


Figure 5.8: The hysteresis of TFP bearings under Kobe @ Takatori earthquake.

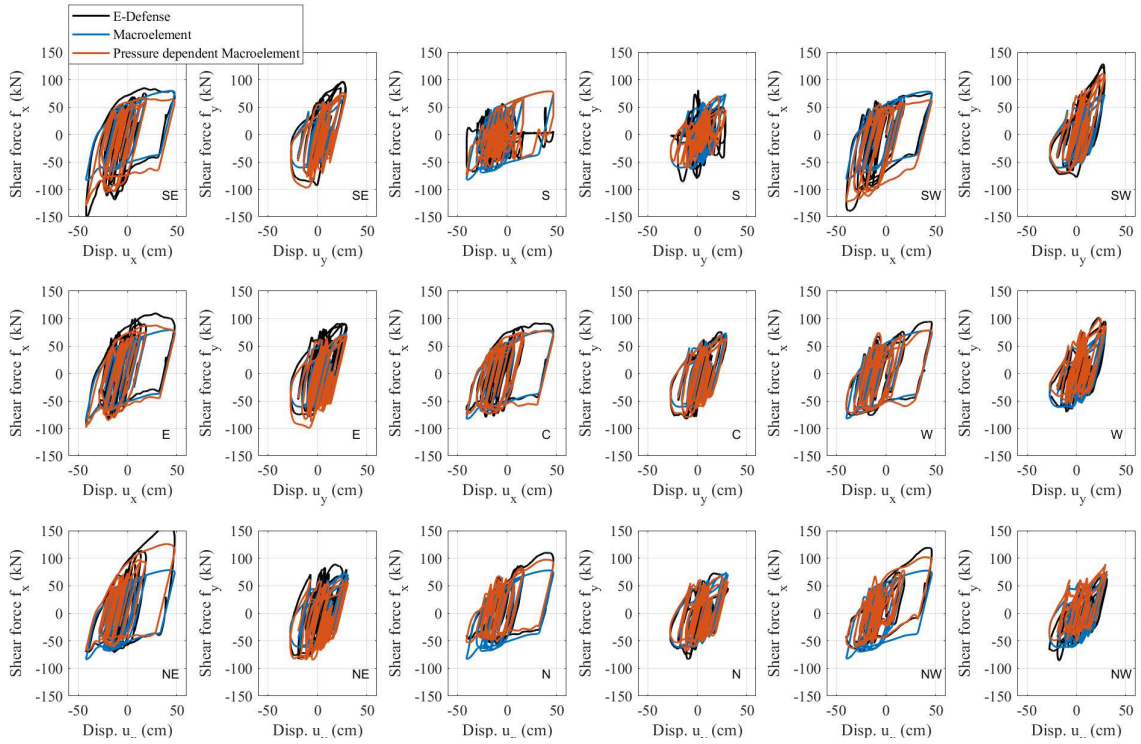


Figure 5.9: The hysteresis of TFP bearings under Chi-Chi @ TCU065 earthquake.

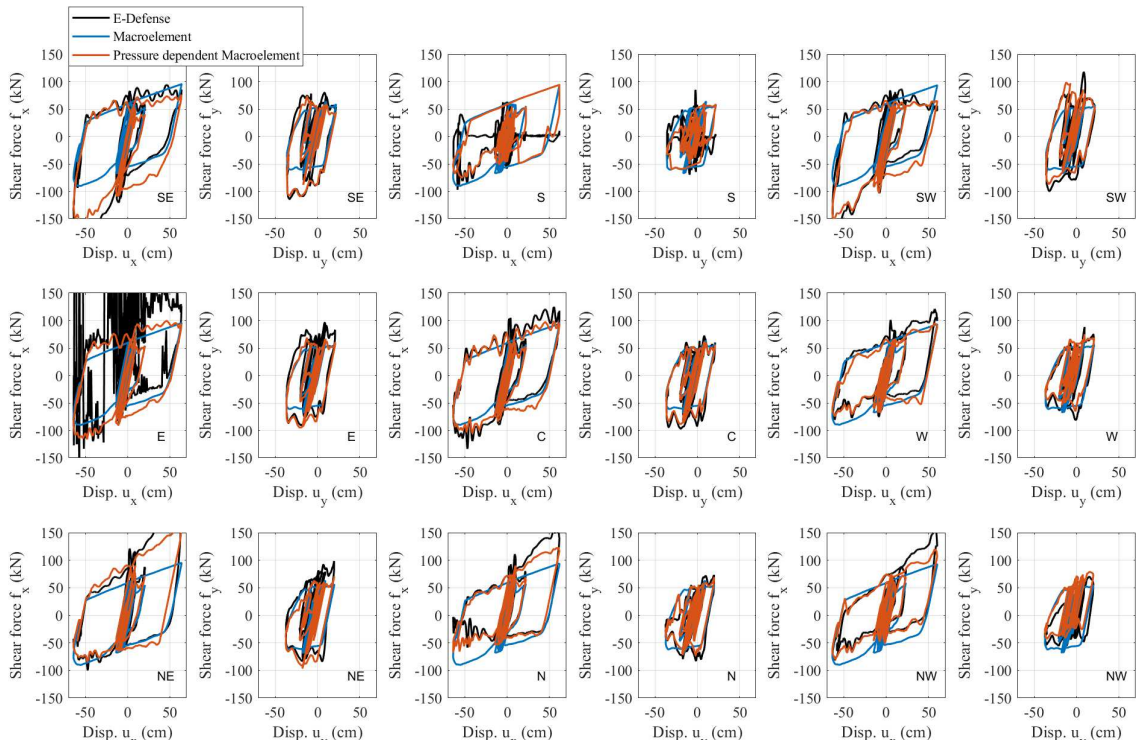


Figure 5.10: The hysteresis of TFP bearings under Tabas @ Tabas earthquake.

Table 5.4: Estimated weight of the specimen by floor level.

Floor	Roof	5 th	4 th	3 rd	2 nd	Base
Total weight (kN)	1153	771	781	782	792	842

5.2.2 E-Defense Building Test

This section will demonstrate the validation of the pressure-dependent macroelement model by simulating the response of the E-defense building and its isolators.

The dimensions of the 5-story steel moment frame building utilizing in E-Defense are obtained from Dao's Ph.D. thesis [22]. The mass distribution of each floor is showed in Table 5.4. Additionally, the vertical reaction at the bases needs to be adjusted due to the imperfection of the E-Defense building. The procedure detail refers to Dao's Ph.D. thesis [22].

The finite element model of E-Defense building was created in Abaqus CAE (Figure 5.11), and the modal analysis has been performed. The first three modes shapes of the fixed base building are shown in Figure 5.12. The Table 5.5 demonstrates the finite element model mode shapes match with E-Defense experiment data [33] very well. The maximum error is 7%, which indicates a good fit.

The damping also plays an important role in the structure [51, 19, 75]. In this study, Rayleigh damping was used to represent energy dissipation in the E-Defense structure. The Rayleigh damping matrix can be expressed by Equation 5.3 [15].

$$\mathbf{C} = \alpha_m \mathbf{M} + \alpha_K \mathbf{K} \quad (5.3)$$

Where \mathbf{C} , \mathbf{M} , \mathbf{K} are the global damping, mass, and stiffness matrix. The damping ratio ξ can be obtained through Equation 5.4.

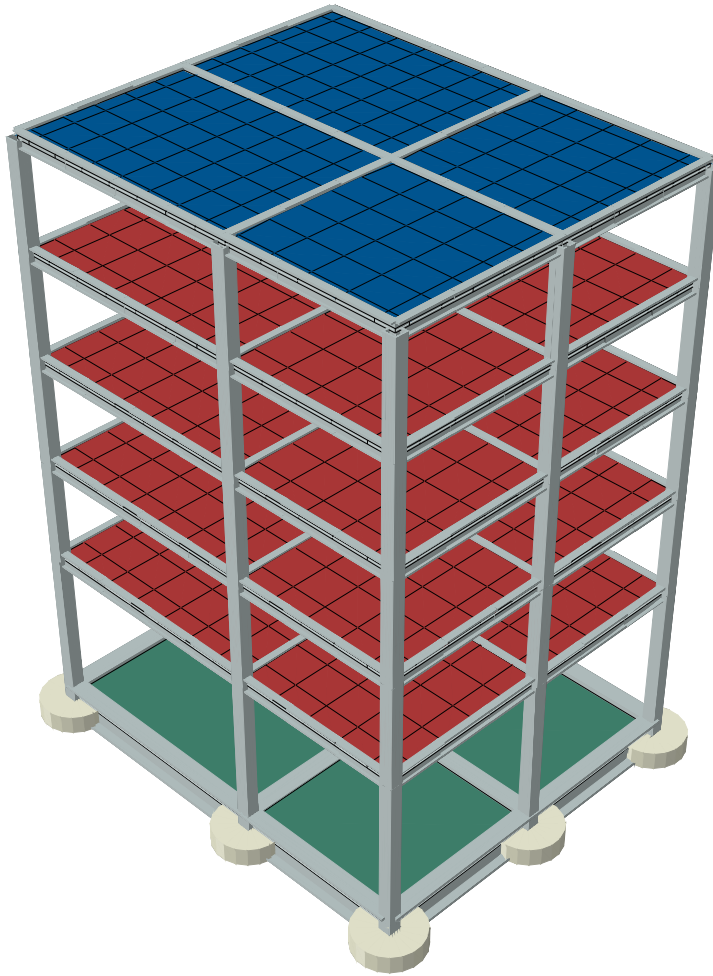


Figure 5.11: The finite element model of E-Defense building.

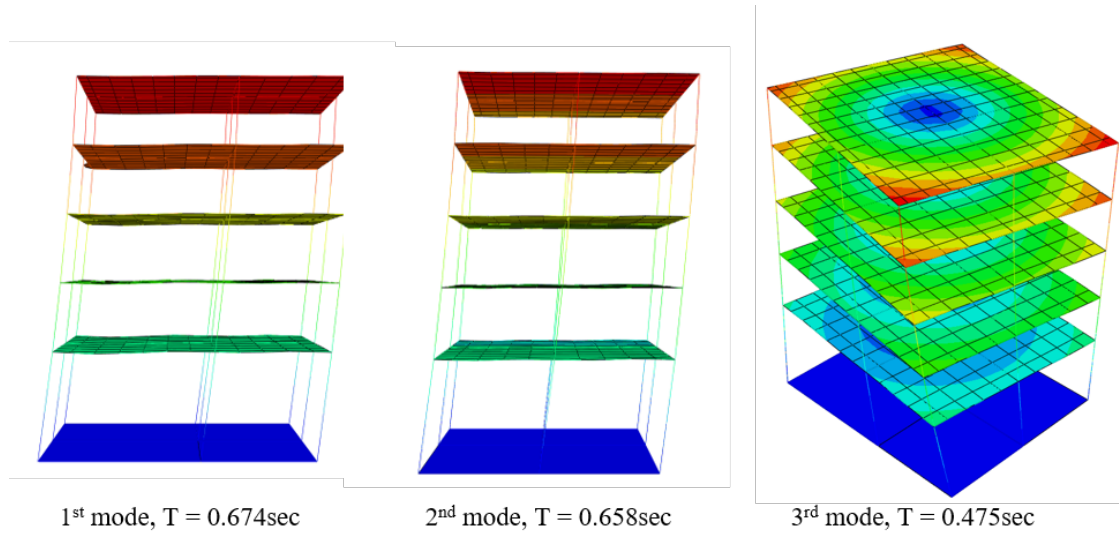


Figure 5.12: The first 3 modes shape and period of the E-Defense building.

Table 5.5: modal analysis of the E-Defense building.

Mode No.	Experiment period T (sec)	Abaqus model period T (sec)	Error (%)
1 st y direction mode	0.677	0.674	0.52
2 nd y direction mode	0.211	0.223	5.21
3 rd y direction mode	0.113	0.119	4.71
1 st x direction mode	0.652	0.658	0.96
2 nd x direction mode	0.204	0.220	7.18
3 rd x direction mode	0.112	0.117	4.56
1 st vertical mode	0.142	0.146	2.8
1 st rotational mode	0.472	0.475	0.65

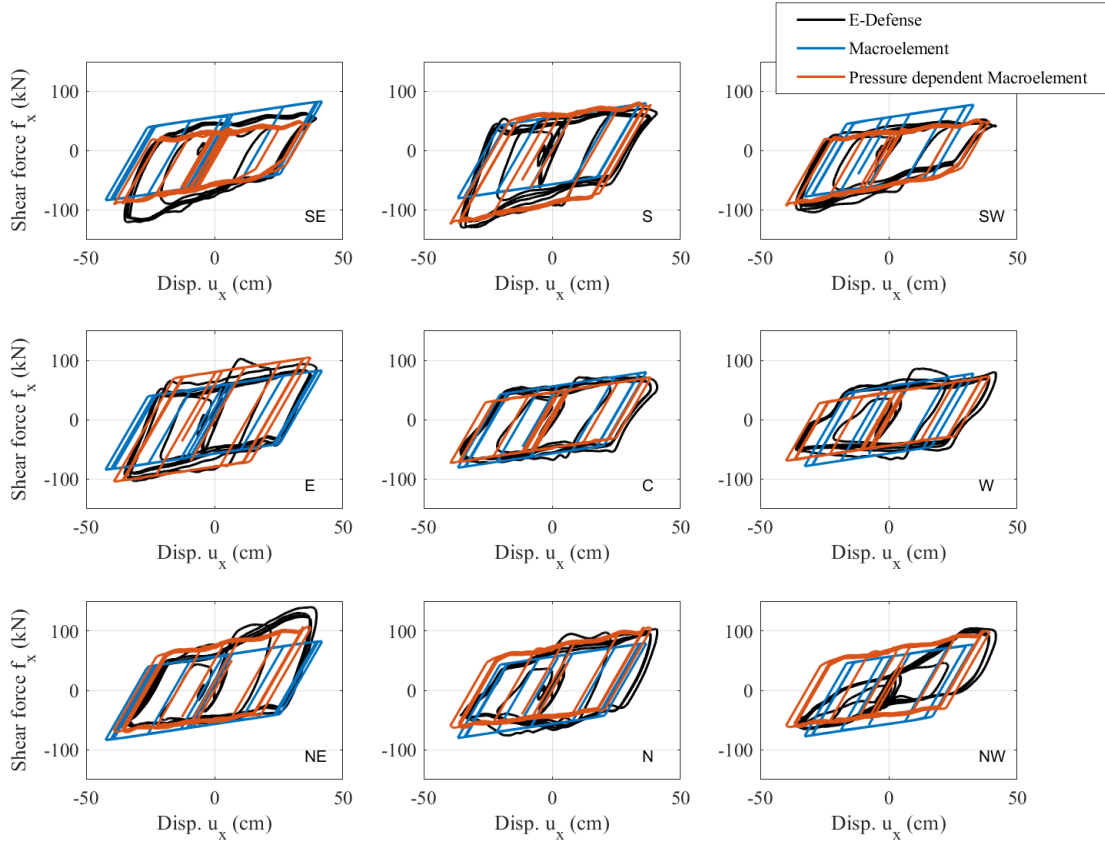


Figure 5.13: The hysteresis of TFP bearings under sine wave.

$$\xi_n = \frac{a_M}{2} \frac{1}{\omega_n} + \frac{a_K}{2} \omega_n \quad (5.4)$$

Where ω_n is the structure's natural frequency of the n^{th} mode. After combine Equation 5.3 and 5.4, a_M and a_K can be evaluated by Equation 5.5 with selected damping ratio. The ξ_1 and ξ_2 are chosen as 1.5% and 2.5% separately through manual adjusting.

$$\frac{1}{2} \begin{bmatrix} 1/\omega_i & \omega_i \\ 1/\omega_j & \omega_j \end{bmatrix} \begin{Bmatrix} a_M \\ a_K \end{Bmatrix} = \begin{Bmatrix} \xi_i \\ \xi_j \end{Bmatrix} \quad (5.5)$$

The hysteresis of TFP bearings under sine wave is shown in Figure 5.13. The pressure-dependent macroelement model provides better predictions of the TFP bearing hysteresis than the macroelement model. However, these results' accuracy is less than the single element

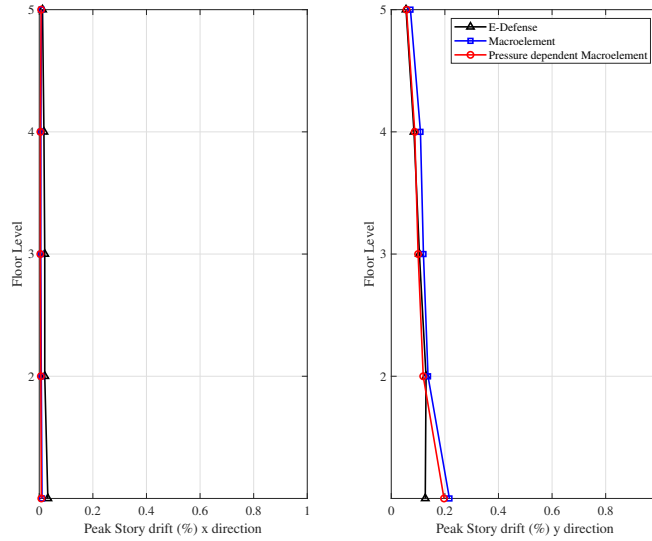


Figure 5.14: The peak inner-story drift ratio of E-Defense building under sine wave.

test since the instantaneous normal pressure is estimated from the finite element model analysis, not directly prescribed the experimental vertical pressure data. Figure 5.14 and Figure 5.15 demonstrate the peak inter-story drift ratio and the maximum floor acceleration of E-Defense building under sine wave. Note that both numerical macroelement models underestimate the first-floor peak acceleration; other than that, the difference between the three results is not significant. The pressure-dependent macroelement model has better predictions than the macroelement model. Therefore, this sine wave validates both TFP bearings elements, and the pressure-dependent macroelement model shows the advantage over the macroelement model.

The building response under the Kobe @ Takatori earthquake is demonstrated in this section as an example of earthquakes with vertical excitations. The details of the building response under else earthquakes are list in appendix C. Similar to the sin wave test, Figure 5.16 indicates that the pressure-dependent macroelement model captures more details of the TFP bearings' response than the macroelement model. The difference between the two numerical models is trivial when displacement is small. This phenomenon can be observed from the X direction hysteresis. However, the pressure-dependent macroelement model can

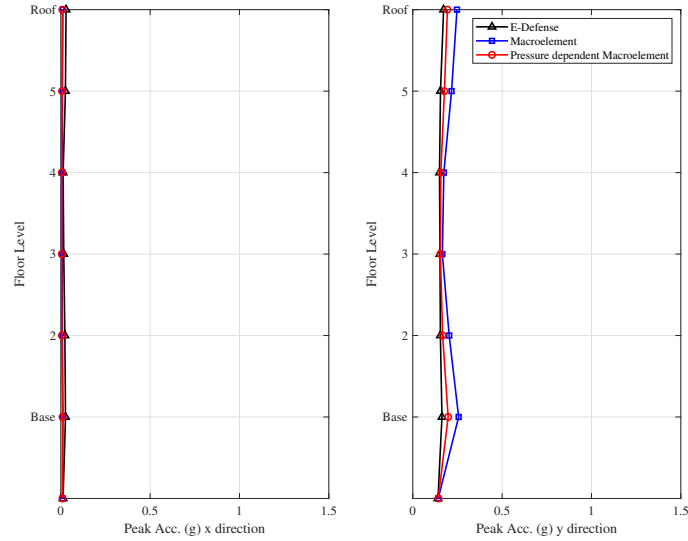


Figure 5.15: The peak floor acceleration of E-Defense building under sine wave.

predict the spikes of the shear forces more accurately than the macroelement model due to the pressure-dependent function applied. The difference in the peak inter-story drift ratio is observed between the numerical model and experiment data. Especially, the first floor maximum inter-story drift ratios are overestimated, which indicates the first story stiffness is smaller than the E-Defense building. Regarding the peak floor acceleration, the pressure-dependent macroelement model captures the second mode shape of the structure due to the vertical effect; on the contrary, the macroelement model misses that capability. These results solidly validate the pressure-dependent macroelement model and suggest that the pressure-dependent macroelement model is preferable to the macroelement model.

In addition, Figure 5.19 suggests the design backbone curve is not a constant anymore due to vertical excitation effects, and only the pressure-dependent macroelement model is able to predict the normalized based shear beyond the constant design backbone curve. The three TFP bearing models predict similar results when the earthquake excitation is moderate. However, only the pressure-dependent macroelement model can capture the spikes of hysteresis, especially when the vertical earthquake can not be neglected. Therefore, the pressure-dependent macroelement model can help designers better understand the response

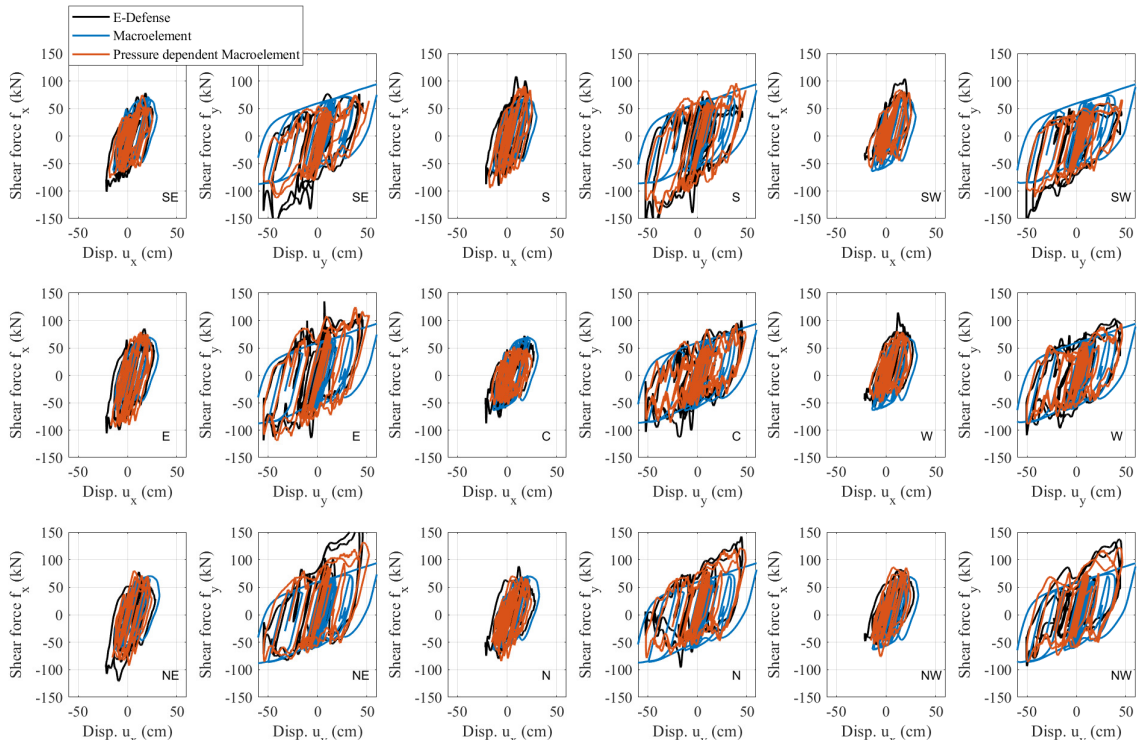


Figure 5.16: The hysteresis of TFP bearings under Kobe @ Takatori earthquake.

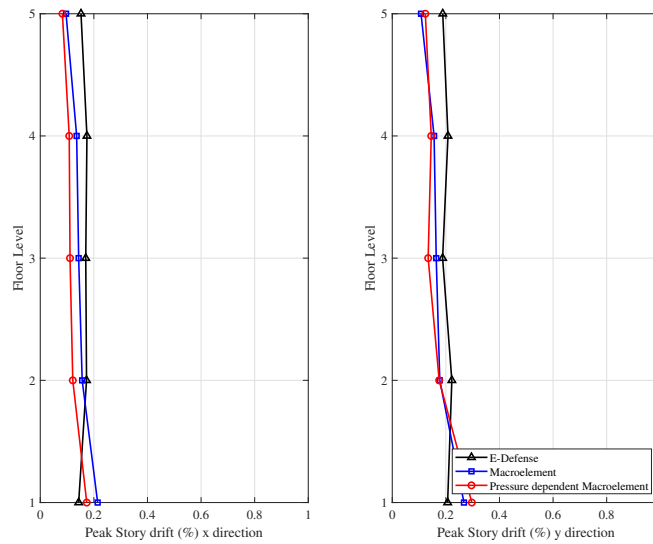


Figure 5.17: The peak inner-story drift ratio of E-Defense building under Kobe @ Takatori earthquake.

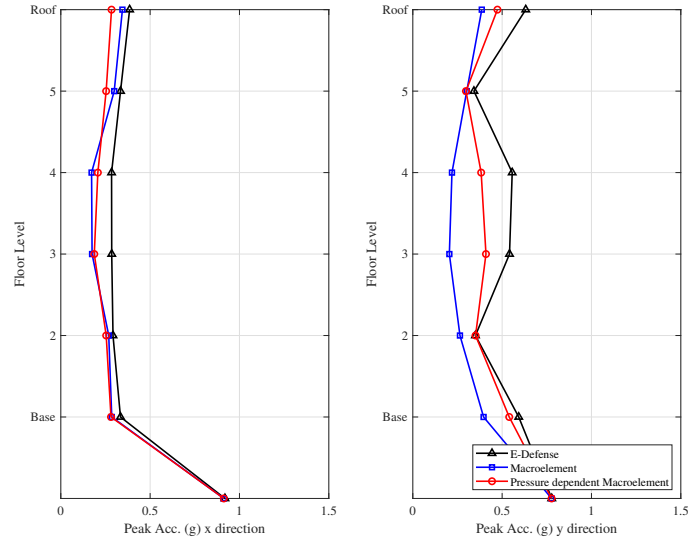


Figure 5.18: The peak floor acceleration of E-Defense building under Kobe @ Takatori earthquake.

of the TFP bearings.

In order to ensure the pressure-dependent macroelement model help increase the accuracy of predicting building response and the finite element model can represent E-Defense building's characteristics, the spectrum analysis of the numerical model had been conducted. The earthquake excitations were applied to the base isolation building. The floor acceleration history was recorded for both horizontal and vertical directions. Then the acceleration history was treated as an external force applied on an SDOF system with unit mass. The maximum accelerations were recorded for various natural periods. Therefore, the natural periods of the base-isolated structure are obtained according to the periods when the local peaks of accelerations appear. In the E-defense experiment, two horizontal accelerometers (Northwest and Southeast) and three vertical accelerometers (Northeast, Northwest, and Southeast) record the acceleration history on each floor. Those acceleration profiles can be used to comparing with the finite element model results. Four earthquake excitations, which include the vertical component, are selected to perform spectrum analysis. The response spectra of the building under the Kobe @ Takatori earthquake are shown through Figure 5.20 to Figure 5.24. The

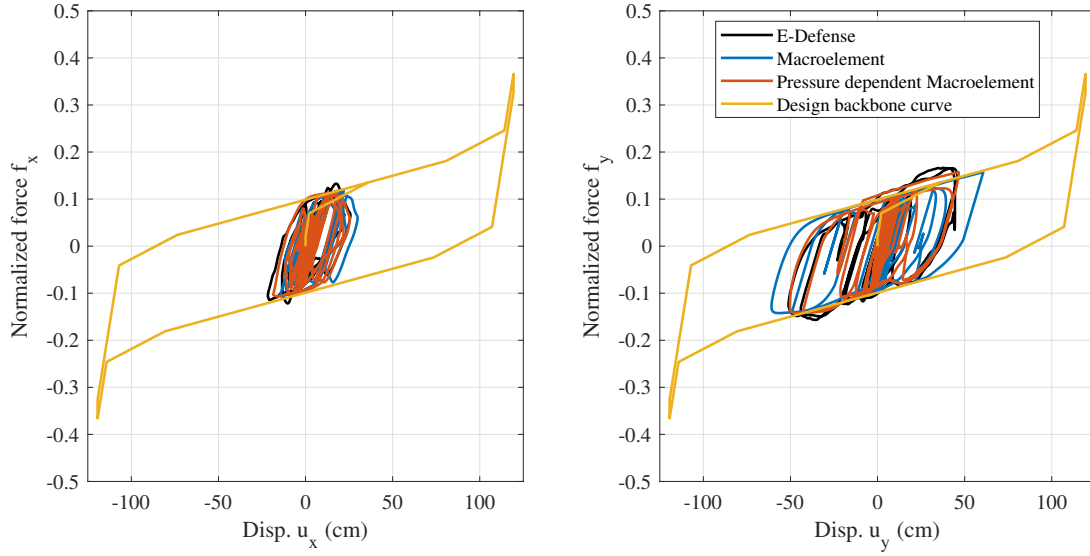


Figure 5.19: The southwest TFP bearings normalized base shear v.s. displacement under Kobe @ Takatori earthquake in E-Defense experiment.

response spectra of the building under the other three earthquakes are listed in Appendix B.

The horizontal acceleration profiles (Figure 5.20 and Figure 5.21) demonstrate that the building with the pressure-dependent macroelement model captures the natural period of the E-Defense building very well. The first three natural periods almost match. However, there is some difference in the magnitude of the acceleration, but still showing the notable advantages over the building with the macroelement model. The building with the macroelement model can also accurately capture the first two natural periods of the E-Defense building. The building with the macroelement model underestimates the magnitude of the acceleration in all the floors for both directions. These results verify the importance of the pressure-dependent macroelement model in helping predict the building response accurately. The difference between the pressure-dependent macroelement model and macroelement model indicates that the vertical force variation significantly affects the horizontal response of superstructures.

Regarding the vertical response of the building, the building utilizing the pressure-dependent macroelement model and macroelement model almost arrive at the same results,

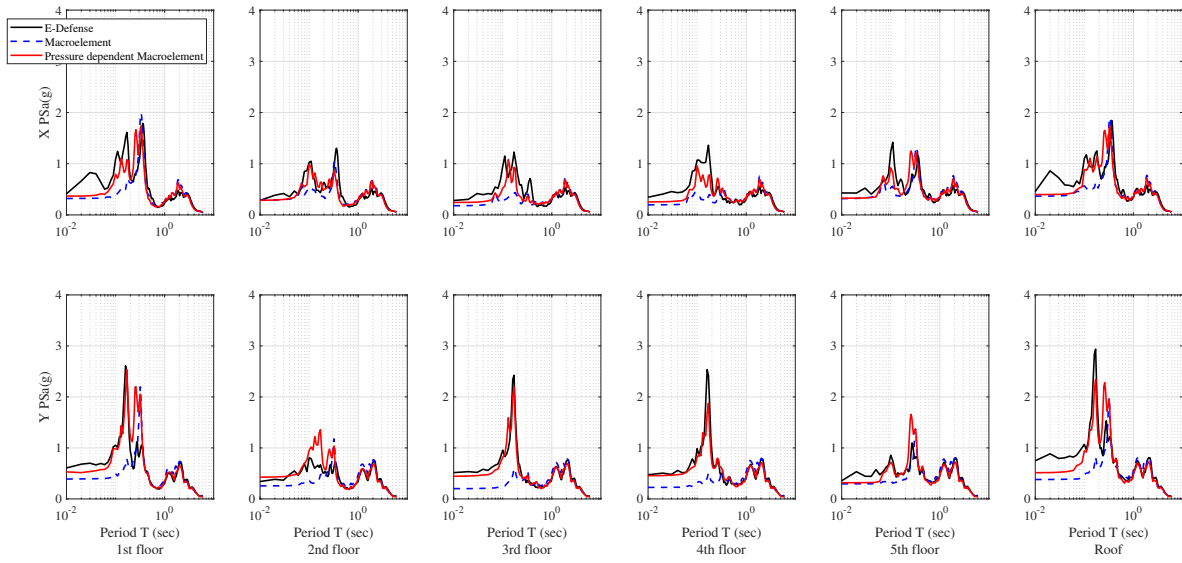


Figure 5.20: The horizontal response spectra of the building under Kobe @ Takatori earthquake (Northwest).

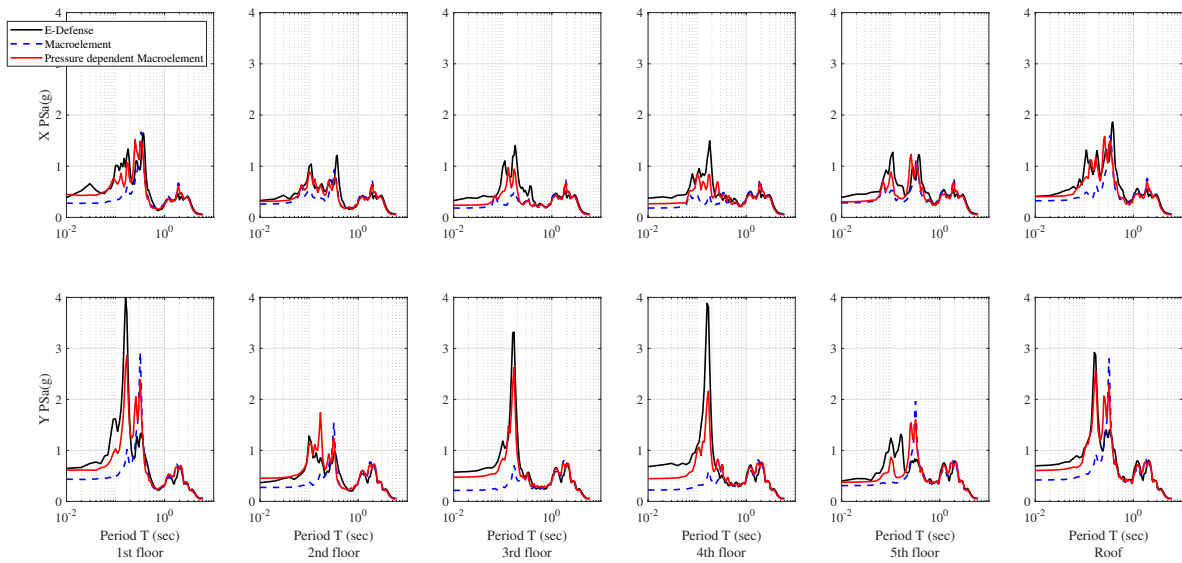


Figure 5.21: The horizontal response spectra of the building under Kobe @ Takatori earthquake (Southeast).

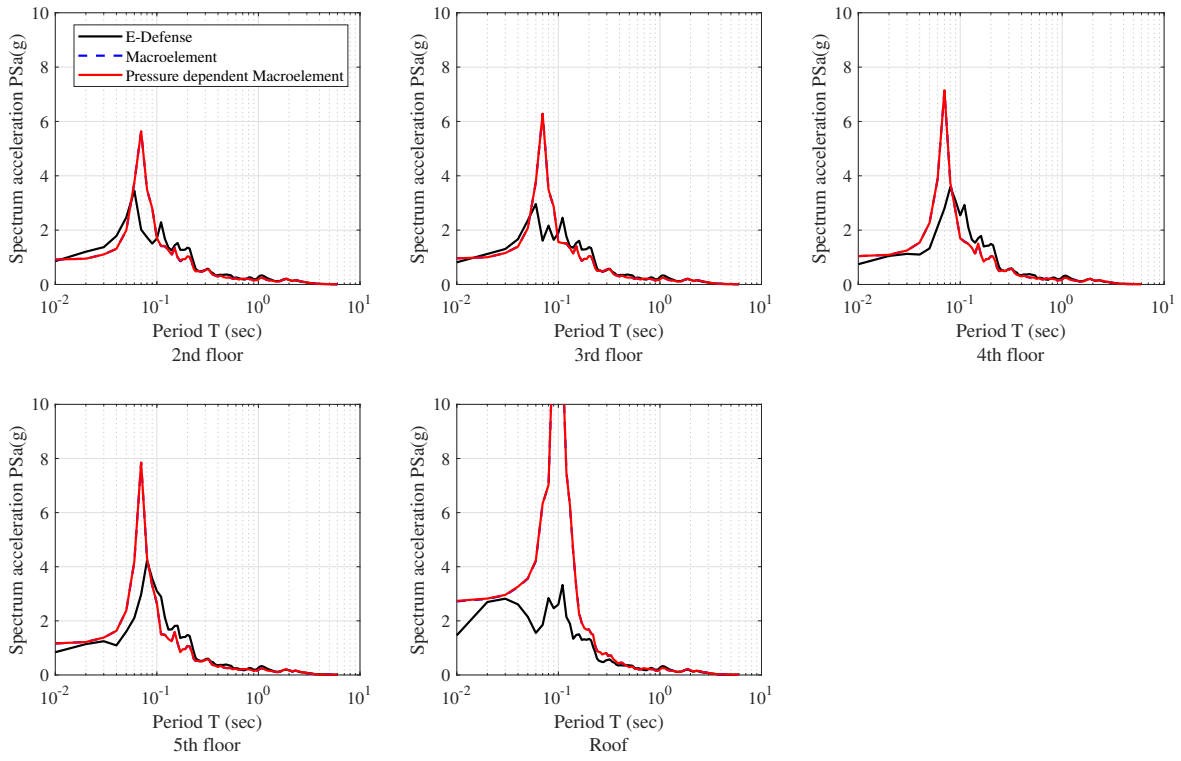


Figure 5.22: The vertical response spectra of the building under Kobe @ Takatori earthquake (Northwest).

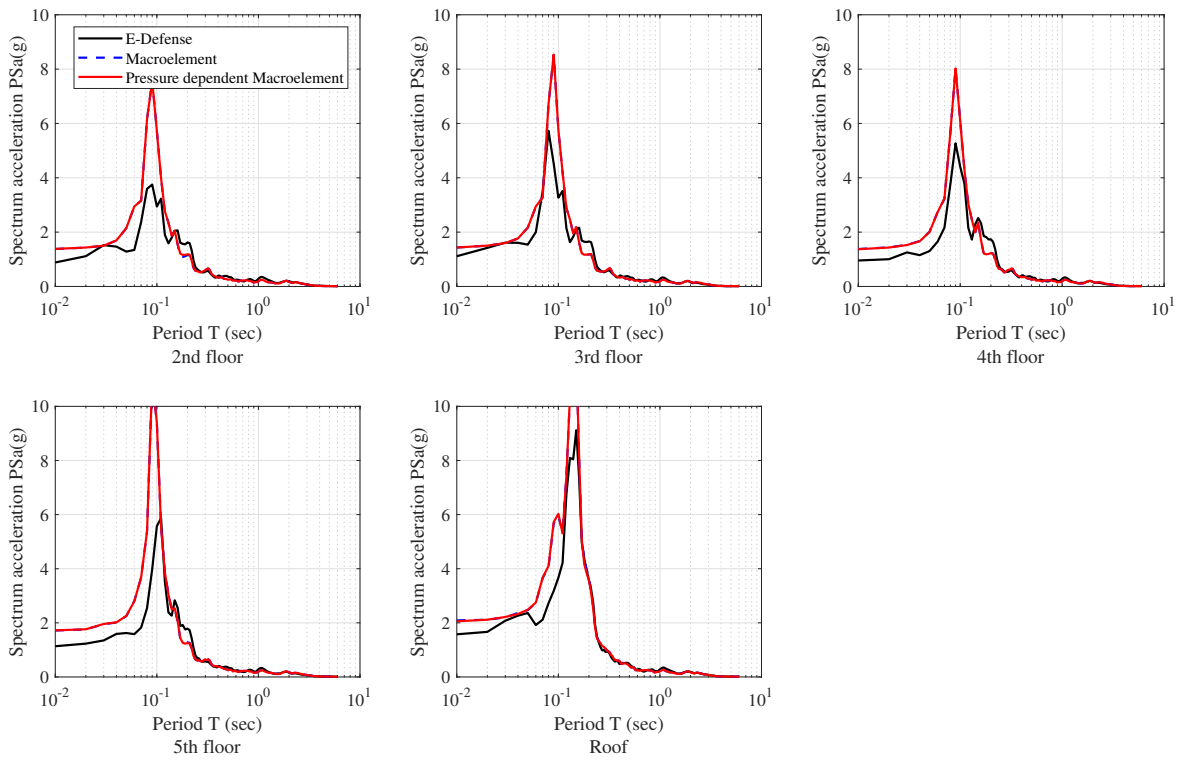


Figure 5.23: The vertical response spectra of the building under Kobe @ Takatori earthquake (Northeast).

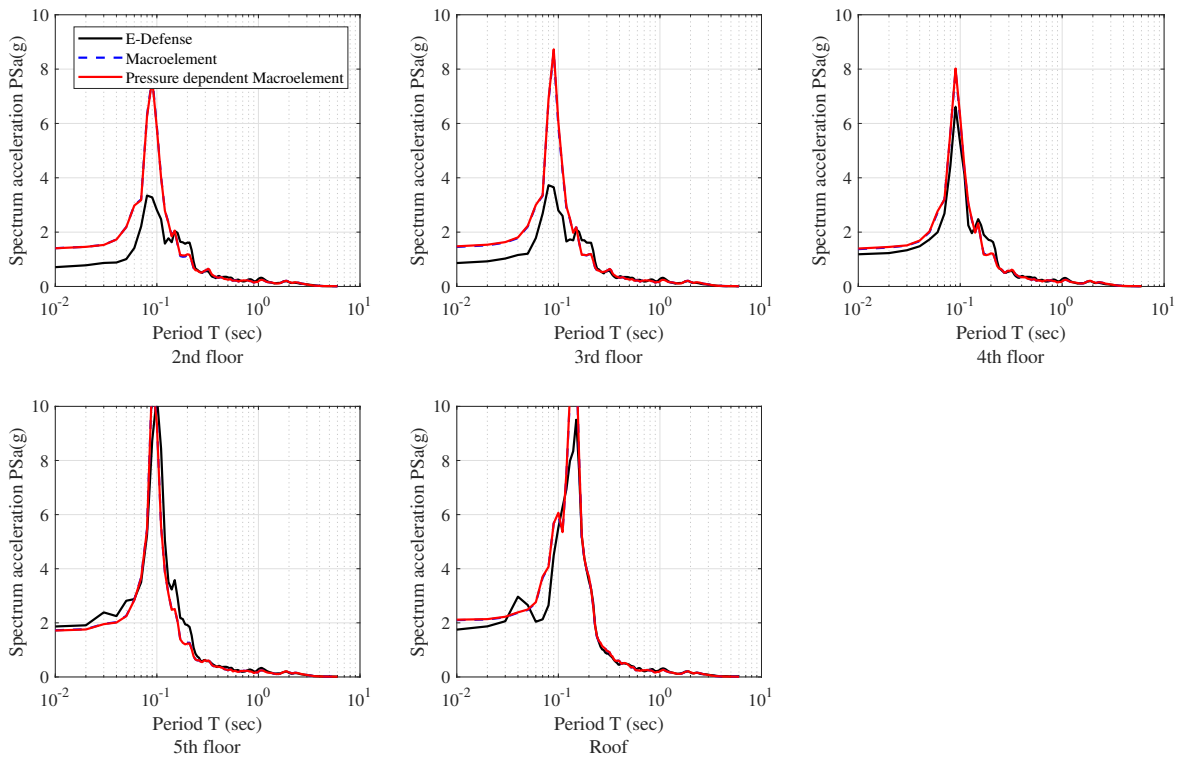


Figure 5.24: The vertical response spectra of the building under Kobe @ Takatori earthquake (Southeast).

which is reasonable since the element type of TFP bearing will not affect the vertical characteristic of the superstructure. This also verifies the finite element model of the E-Defense building can represent the characteristic of the E-Defense building effectively. Figure 5.22 and Figure 5.24 demonstrate that both TFP bearing models predict the vertical natural period of the E-Defense building accurately, but not the acceleration magnitude. There are various reasons to cause the mismatch; one could be misrepresenting the mass distribution for each floor. Besides, the damping ratio can also affect the building response significantly. Therefore, the damping model and parameters should be selected conscientiously.

CHAPTER 6

Fragility-based Seismic Performance Assessment of the E-Defense Building

In the past 30 years, a variety of base-isolated structure has been constructed to achieve the high seismic performance requirement [60], such as hospitals, electronic data center and other critical structures. In order to achieve those enhanced performance requirements, performance-based design is widely adopted [80, 96, 40] in varieties type of buildings and bridges [103, 100, 104, 99], while little attention was given to the base-isolated structures [106, 16, 44, 61, 79]. This chapter will perform a fragility-based seismic performance assessment of the E-Defense building. Three types of TFP bearing models are utilized during the nonlinear response history analysis (NRHA). The difference between the building utilizing three different TFP bearings models provides building owners insight to help them make decisions.

There are two major methods to develop the fragility curves; the first one is the incremental dynamic analysis (IDA) [93, 92, 24, 95] which requires performing NRHA of structures with continuing scaled ground motions in a specific range, for instance, [94, 4, 47]. However, the IDA method is debatable because scaling the ground motions incrementally will misrepresent the characteristic of seismic hazard for different earthquake intensity levels [3, 10, 42, 46]. On the contrary, the probabilistic seismic demand modeling (PSDM) approach [81, 48, 21, 29] can overcome the disadvantage of the IDA method mentioned above by formulating the relationship between the certain intensity measure (IM) and the engineering demand parameters (EDPs), which do not require scaling the ground motions. There are

varieties of examples showing developing fragility curves by PSDM approach for non-ductile reinforced concrete buildings [13, 38, 71]. Since base-isolated structures are designed for enhanced performance requirements, it is appropriate to focus on severe earthquake events analysis; in other words, the maximum considered event (MCE) is selected as the target seismic hazard level. The corresponding return period is 2475 years. Therefore, the PSDM approach is adopted in this study. The PSDM approach describes the relationship between Demand (D) and IM as Equation 6.1. By taking the logarithm of both sides of the Equation 6.1, the inverse logarithm of the vertical intercept a and the slope b can be estimated from regressing $\ln(IM)$ on $\ln(D)$, the mean demand is evaluated as Equation 6.2, and the corresponding dispersion (or standard deviation) is described in Equation 6.3.

$$D = a(IM)^b \quad (6.1)$$

$$\ln(D) = \ln(a) + b \cdot \ln(IM) \quad (6.2)$$

$$\beta_{D|IM} \cong \sqrt{\frac{\sum (\ln(d) - \ln(aIM^b))^2}{N - 2}} \quad (6.3)$$

The fragility curve, which describes the probability of demand exceeding the capacity (C) for a given intensity level, is expressed as Equation 6.4. β_M and β_C denote the uncertainty in modeling and variability in capacity, respectively. The selected β_M and β_C values are shown in Table 6.1 according to the requirement of HAZUS [34].

In this study, the peak floor accelerations (PFAs) are used to define median values of the damage to Non-Structural acceleration-sensitive components, and the threshold for four damage states are shown in Table 6.2 according to the requirement of HAZUS [34]. Similarly, for the structural drift-sensitive components, the inter-story drift ratios (IDRs) are selected as EDP, and the threshold for four damage states are shown in Table 6.3.

Table 6.1: The variability in capacity β_C and the uncertainty in modeling β_M .

	β_C	β_M
Nonstructural acceleration-sensitive components	0.25	0.6
structural drift-Sensitive components	0.25	0.4

Table 6.2: The peak floor accelerations are used to define median values of the damage to non-structural acceleration-sensitive components.

Floor acceleration (g) at the threshold of non-structural damage			
slight	Moderate	Extensive	Complete
0.3	0.6	1.2	2.4

$$P(D > C | IM) = 1 - \Phi \left(\frac{\ln(\hat{C}) - \ln(a \cdot IM^b)}{\sqrt{\beta_{D|IM}^2 + \beta_C^2 + \beta_M^2}} \right) \quad (6.4)$$

Table 6.3: The peak inter-story drifts ratio (%) are used to define median values of the damage to structural drift-sensitive components.

Inter-story drift at the threshold of structural damage			
slight	Moderate	Extensive	Complete
0.4	0.80	2.00	5.33

6.1 Ground Motion Selection

This study utilizing E-Defense building as an example building assumed located in Los Angeles; based on the site conditions, the target horizontal and vertical spectrums are constructed by the ground motion model (GMM) [9]. Then 40 earthquake records are selected from PEER NGA-West2 database [68] and match to the design spectrum through greedy ground motion selection algorithm [37]. The selected ground motions, which are the same as the ground motions mentioned in Zhang's paper [105], the response spectra of the selected records are shown in Figure 6.1.

6.2 The Effect of Earthquake Orientation

Multiple researchers point out that the orientation of the input earthquake excitations will affect the nonlinear history response of the superstructure [73, 72, 31, 6, 35, 28]. Therefore, the experiment investigating the sensitivity of the superstructure response under different ground motions directions has been conducted for two selected earthquakes (Chuetsu-Oki @ Kashiwazaki City Center earthquake and Landers @ North Palm Springs Fire Sta #36 earthquake). Nonlinear dynamic analyses are performed on E-Defense Building by considering twelve different earthquake directions, which rotate the direction of both the orthogonal components by 15° for each analysis. Three TFP bearing models mentioned in the previous chapter are utilized during the analysis. For convenience, the uncoupled macroelement model is denoted as 1D in this chapter's figure, and the macroelement model is denoted as 2D, and the pressure-dependent macroelement model is denoted as 3D. The peak floor accelerations and inter-story drift ratios are shown through Figure 6.2 to Figure 6.3. These results demonstrate that the ground motion orientation effect is not prominent. The uncoupled macroelement model shows the biggest difference of peak floor accelerations and inter-story drift ratios under different earthquake excitations. Table 6.4 shows the details of the peak floor accelerations and inter-story drift ratios, which confirms that the uncoupled

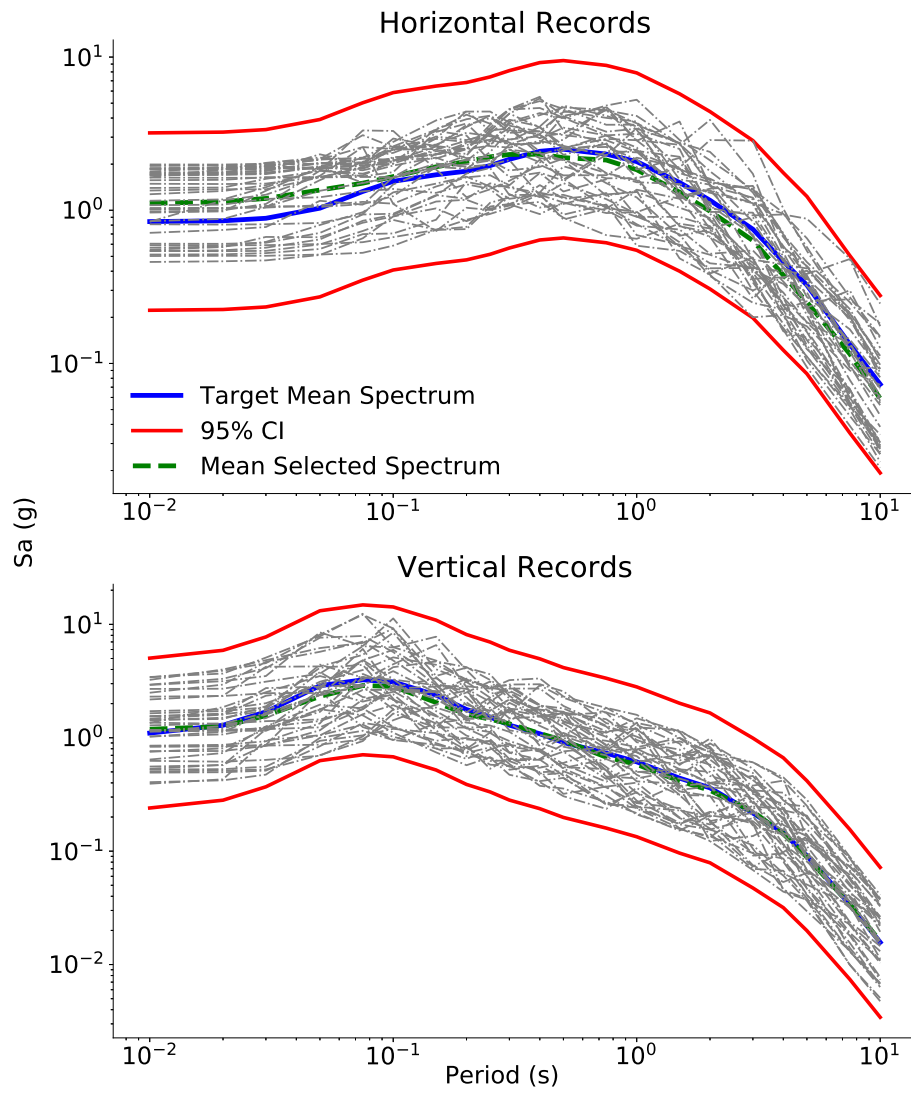


Figure 6.1: 5% damped acceleration response spectra of the selected records (2475 years)

[105].

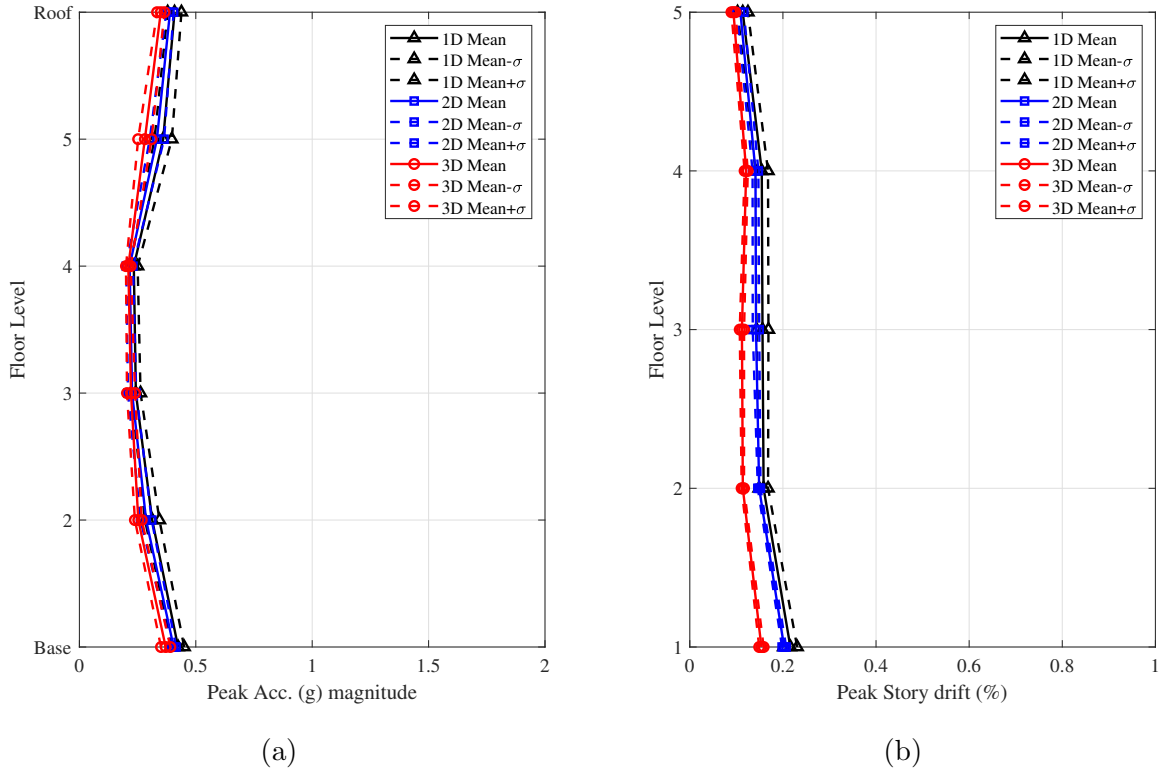


Figure 6.2: The distribution of the peak floor accelerations (a), and inter-story drift ratio (b) for three models under the Chuetsu-Oki @ Kashiwazaki City Center earthquake with different earthquake orientations.

macroelement model is sustainable to the orientation of the earthquake excitations. However, the difference of peak floor accelerations and inter-story drift ratios caused by ground motion orientation is insignificant. In order to save the computational power, two different earthquake directions (original and rotating the direction of both the orthogonal components by 90°) for each earthquake are utilized in this study.

6.3 Intensity Measure (IM) Selection & Damage Fragility Curves

Four IMs (i.e., $SaT1$, Sd , PGA , PGV) are investigated in this study. Efficiency, proficiency, and practicality are good metrics to evaluate the goodness of the IMs [14]. A small $\beta_{D|IM}$

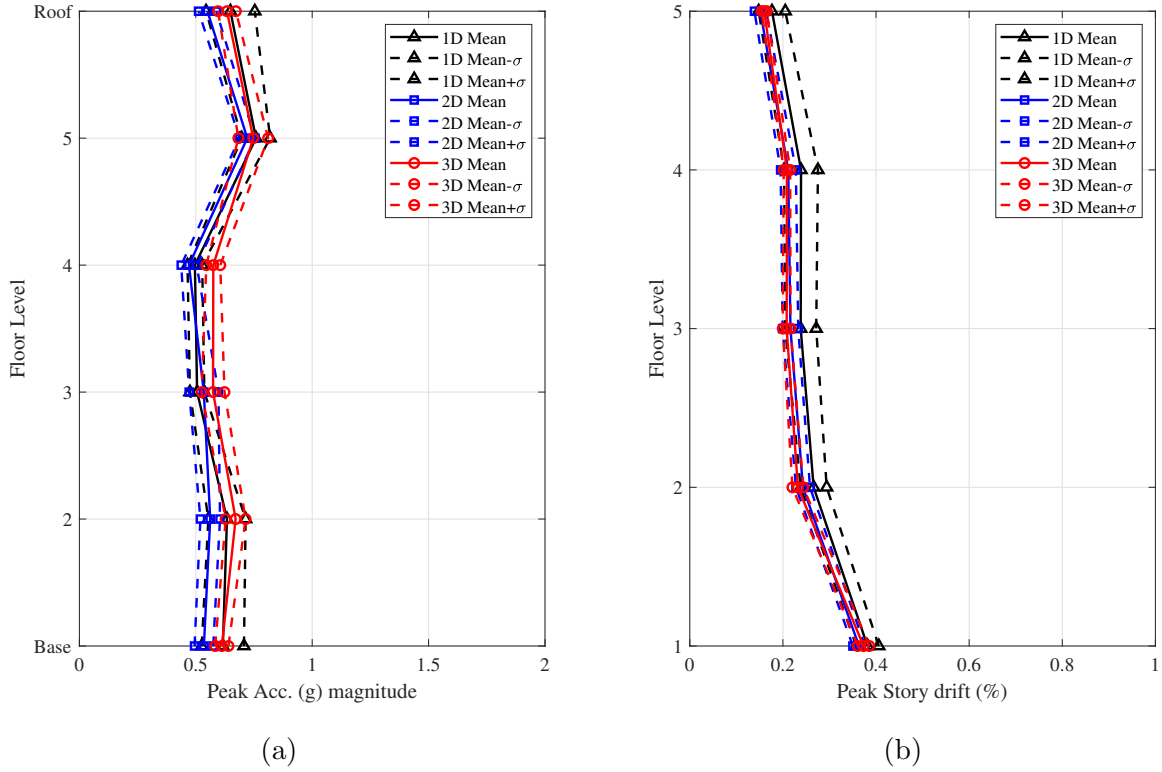


Figure 6.3: The distribution of the peak floor accelerations (a) and inter-story drift ratio (b) for three models under Landers @ North Palm Springs Fire Sta #36 earthquake with different earthquake orientations.

Table 6.4: Max. difference of the peak floor accelerations, and inter-story drift ratio under different orientations of the earthquake excitations.

Earthquake event	peak floor acc. (g)			peak drift ratio (%)		
	1D	2D	3D	1D	2D	3D
Chuetsu-Oki	0.1012	0.0981	0.0913	0.0597	0.0241	0.0148
Landers	0.3427	0.1911	0.2114	0.1179	0.0534	0.0409

Table 6.5: the proficiency ζ of different intensity measures for IDR.

IM	Uncoupled macroelement	macroelement	Pressure dependent macroelement
<i>SaT1</i> (g)	1.57	1.88	1.52
<i>Sd</i> (m)	1.57	1.87	1.52
<i>PGA</i> (g)	1.19	1.26	1.15
<i>PGV</i> (m/s)	1.09	1.18	1.05

Table 6.6: the proficiency ζ of different intensity measures for PFA.

IM	Uncoupled macroelement	macroelement	Pressure dependent macroelement
<i>SaT1</i> (g)	2.13	2.50	2.09
<i>Sd</i> (m)	2.13	2.50	2.10
<i>PGA</i> (g)	1.25	1.34	1.28
<i>PGV</i> (m/s)	1.33	1.49	1.29

leads to a slight variation of the estimated demand, which suggests efficient IM. The practicality depends on the slope b in the regression analysis (Appendix E). The EDP should be proportional to IM theoretically. Small b indicates that the EDP does not depend on IM; in other words, impractical. Therefore, bigger b is preferred. The proficiency is a combination of the efficiency and practicality expressed in Equation 6.5. The regression results are shown in Table 6.5, and Table 6.6 suggest that the PGA and PGV are the best IMs for PFA and IDR, respectively.

$$\zeta = \frac{\beta_{D|IM}}{b} \quad (6.5)$$

Figure 6.4 demonstrates the PFAs and IDRs for E-Defense building using three TFP

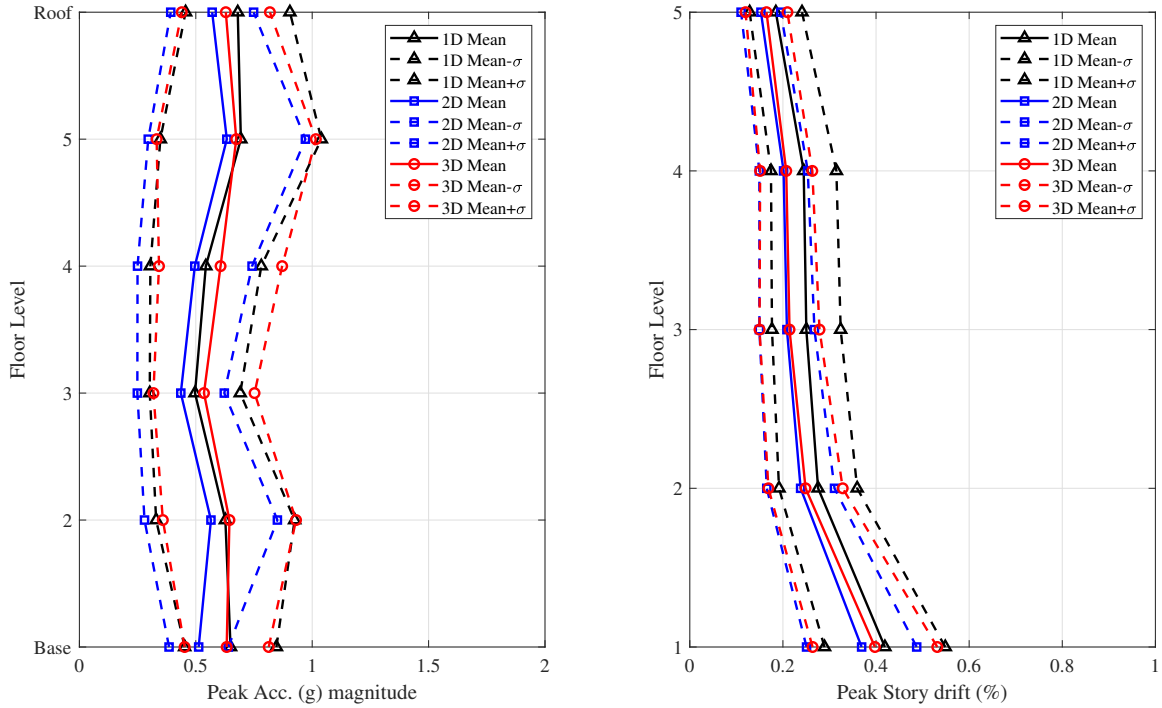


Figure 6.4: The average and standard deviation of the peak floor accelerations (a), and inter-story drift ratio (b) for three models.

bearing models. The pressure-dependent macroelement model and the uncoupled macroelement model generate higher PFAs than the macroelement model. The macroelement model predicts similar IDRs as the pressure-dependent macroelement model, and the uncoupled macroelement model provides the highest IDRs. From PSDM, the fragility curves are obtained through Equation 6.4. For non-structural acceleration-sensitive components (Figure 6.5), the pressure-dependent macroelement model and macroelement model indicate the highest and lowest probability of damage, respectively. These results verify that vertical earthquake excitations are not negligible since the pressure-dependent macroelement model provides the most conservative result, which helps the designer make a better decision. The uncoupled macroelement model overestimates the stiffness of the whole structure, and it is no surprise that this model predicts higher PFAs than the macroelement model. However, the pressure-dependent macroelement model makes the building even stiffer than the uncoupled

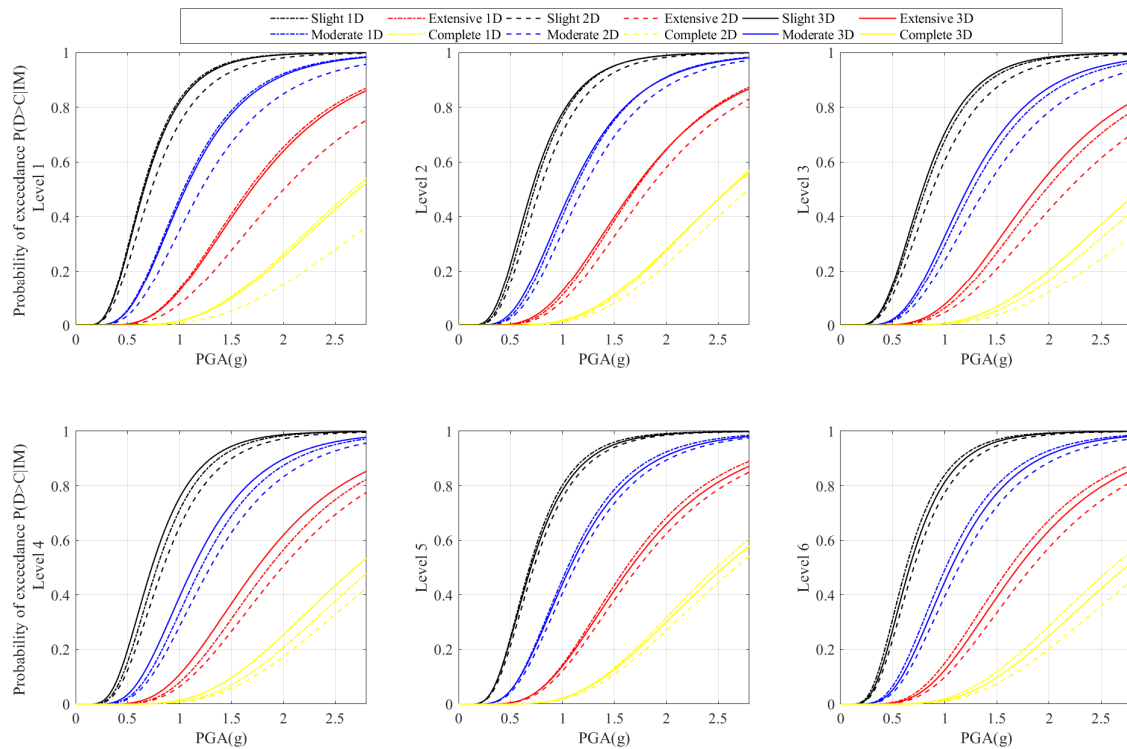


Figure 6.5: Fragility functions for slight, moderate, extensive, and complete damage (EDP=FPA).

macroelement model. Therefore, the pressure-dependent macroelement model experience the highest PFAs and probability of damage.

For structural drift-sensitive components (Figure 6.6), the macroelement model predicts the lowest probability of damage since the macroelement model underestimates the stiffness of the TFP bearings by ignoring the vertical pressure effect. On the contrary, the uncoupled macroelement model transfer more base shear to supper structure because of overestimating the stiffness of the TFP bearings; only the pressure-dependent macroelement model can represent the characteristic of the TFP bearings reasonably.

Figure 6.7 and Figure 6.8 demonstrate the probability of non-structural damage if MRI machines, IT servers, and Data Racks are placed in the E-Defense building. The floor acceleration thresholds of damage for them are 0.3 g and 0.2 g, respectively. The fragility curves

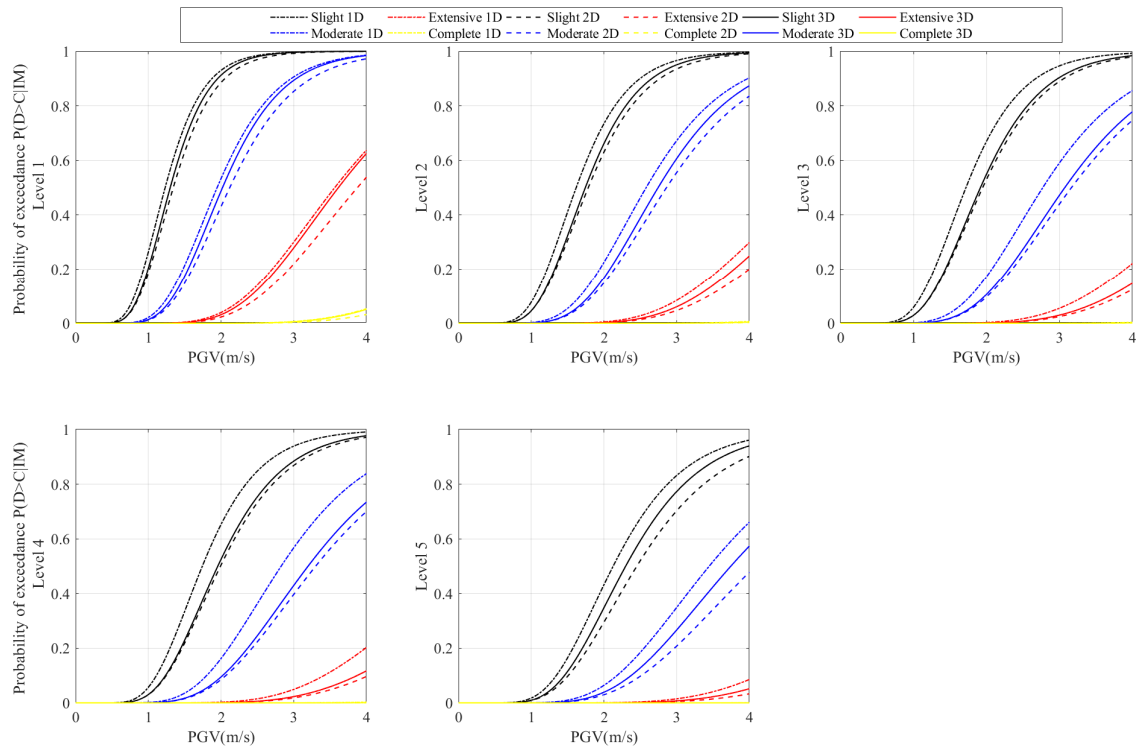


Figure 6.6: Fragility functions for slight, moderate, extensive, and complete damage (EDP=IDR).

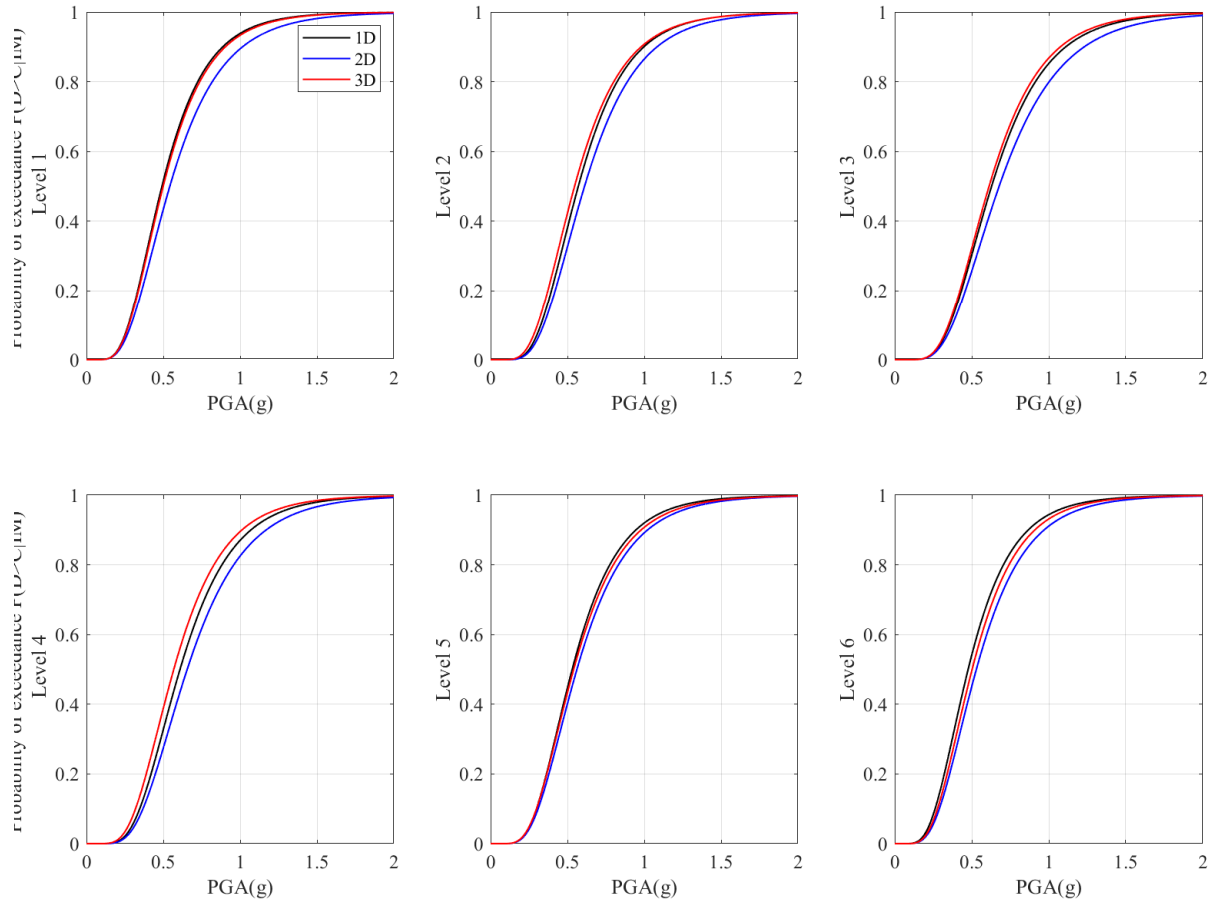


Figure 6.7: Fragility functions for slight, moderate, extensive, and complete damage (EDP=FPA).

suggested a higher probability of damage to this equipment when the pressure-dependent macroelement model was applied.

The lifetime repair cost is estimated utilizing the method described in HAZUS [34], the total construction cost of the E-Defense building has been normalized to the unit value, the repairing cost analysis is performed utilizing EDPs in Performance-Based Engineering Application develop by SimCenter [1]. Figure 6.9 indicated that the lifetime repair cost of the pressure-dependent macroelement model and uncoupled macroelement model is higher than the macroelement model. The probability of no need to repair during the building lifetime

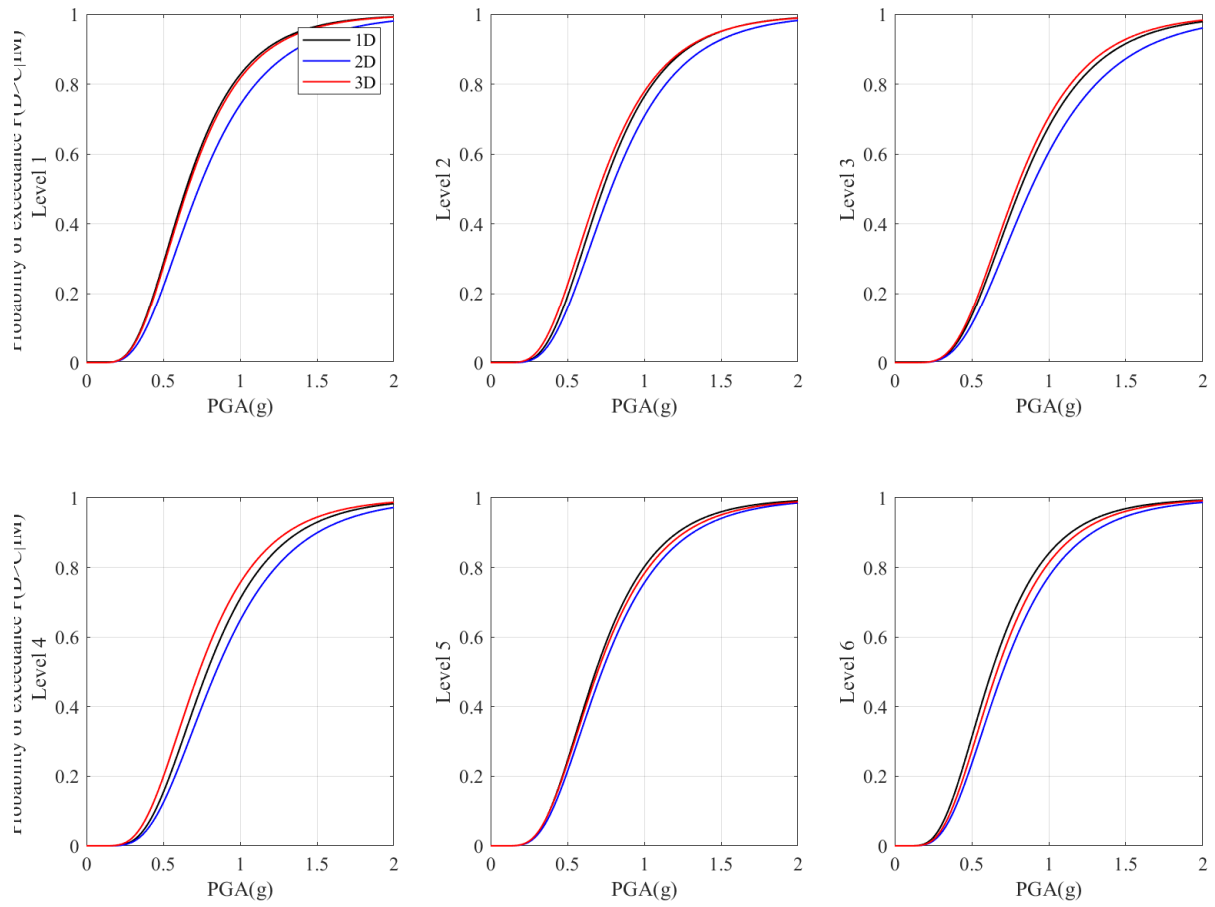


Figure 6.8: Fragility functions for slight, moderate, extensive, and complete damage (EDP=PFA).

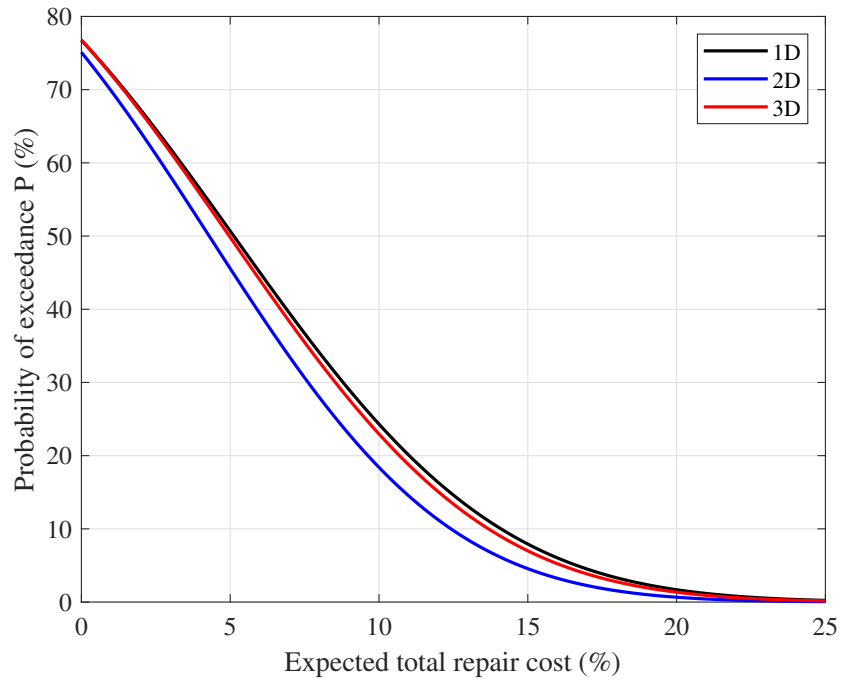


Figure 6.9: Expected total repair cost (%).

is around 25%. The building owner only has to pay around 5% of the total building cost for maintenance during the building lifetime, with a 50% probability. This result provides significant evidence to inform the building owners to make rational decisions.

CHAPTER 7

Conclusions & Future Work

7.1 Chapter-by-chapter Summaries and Conclusions

The first two chapters of this study were devoted to a literature review, which examined the basic attributes and design methodologies for base isolation and numerical modeling techniques, with a special focus on friction pendulum bearing devices.

In Chapter 3, highly detailed modeling and simulation of the hysteretic response of a TFP bearing through the finite element method was attempted. The model was demonstrated to capture the measured responses from a full-scale laboratory test. While such models are extremely useful in generalizing/extending experimental data and for detailed examinations of various phenomena using physics-based constituent/constitutive models, it was observed that they are yet far from being practically useful in an engineering design sense. This was due to the high computational costs of implicit time-stepping emanating primarily from the difficulties associated with multi-surface frictional contact nonlinearities. Computations with explicit methods were not fruitful, as they have exhibited either too many spurious oscillations under default procedures of a state-of-the-art finite element software (ABAQUS) or otherwise required extremely small time step sizes. Observations from this initial study led to the decision to pursue reduced-order (macroelement) models that can provide computational efficiency with adequate accuracy.

In chapter 4, a multi-surface plasticity framework was devised to represent the omnidirectional hysteretic responses of TFP bearings in a physically consistent manner. Unlike the

uncoupled models, which are commonly used in engineering practice, the omnidirectional macroelement model produces identical reactions regardless of its orientation in the numerical model. The proposed model also had the advantage of being physically intuitive due to its direct correspondence with the device's geometry and kinematics. It was also easy to calibrate, requiring only the uniaxial lateral load-deformation backbone curve.

The macroelement model was implemented in ABAQUS as a user element (UEL), and validated against data from experiments conducted at UC Berkeley [5]. An application of the macroelement model was also described in chapter 4. The prediction differences between the omnidirectional and the uncoupled model indicated that this modeling error was significant and could be easily avoided.

Another essential advantage of the macroelement model was cited as being its versatility. While not specifically demonstrated, a parallel study (not included in this dissertation) demonstrated that the proposed omnidirectional modeling approach could easily be adapted to other applications, such as soil-pile interaction [49, 50].

In chapter 5, the omnidirectional model was extended to consider vertical response coupled with lateral responses, and a pressure-dependent macroelement model was devised. This new triaxial model was then validated using data from a single element test and also from an E-Defense shake table experiment on a full-scale base-isolated building. It was observed in these validation studies that only the pressure-dependent macroelement model could predict the base shear beyond the nominal backbone curve and captured the experimentally observed spikes in the hysteresis loops. The pressure-dependency was significant when vertical motions were considered, and their omission in analyses appeared detrimental to engineering design and seismic risk characterization.

In chapter 6, performance-based analyses were performed on the E-Defense building. The computed fragility curves suggested that analyses utilizing the pressure-dependent macroelement model will predict generally higher probabilities of structural and non-structural damage than the other two (coupled biaxial and uncoupled biaxial models). The analysis of

lifetime repairing costs yielded similar conclusions.

These results indicated the importance of utilizing pressure-dependent macroelement models in engineering computations. Both the basic uncoupled, and—to a lesser degree—, the coupled biaxial models will misrepresent the fragility curves in general. Nevertheless, these findings were tied only to the specific (E-Defense) building studied, and the relatively limited ground motions considered.

7.2 Recommended Future Work

Various researchers have attempted to incorporate new physical phenomena into TFP models. For example, Monti and Petrone [58, 76, 43] have examined the effects of uplift and temperature in TFP bearings, as well as rim impact and ultimate rim behavior [91]. These effects and features are omitted in current models used in engineering practice. In some cases, vertical accelerations can cause severe damage to the superstructures, and the TFP bearings do not necessarily have sufficient constraints in the vertical direction. If the vertical acceleration is high enough, uplifting will happen. However, no numerical model can presently predict/represent this phenomenon.

Moreover, the performance of TFP bearings is highly dependent on the effective friction among the sliding surfaces. It is generally well accepted that both velocity and temperature have significant effects on the friction coefficient. Further studies are needed to quantify these effects and to develop accurate and experimentally validated predictive models.

An even more important follow-up study would be to generalize the findings on the effect of modeling errors on the fragility and loss results. The present effort only examined these issues using a single building as a case study and a relatively limited suite of ground motions. A study involving a broad set of buildings (different structural systems and geometries) and seismic hazard levels would illuminate this issue for the practicing engineering community.

APPENDIX A

The TFP Bearing Response under Earthquakes Described in Table 4.3

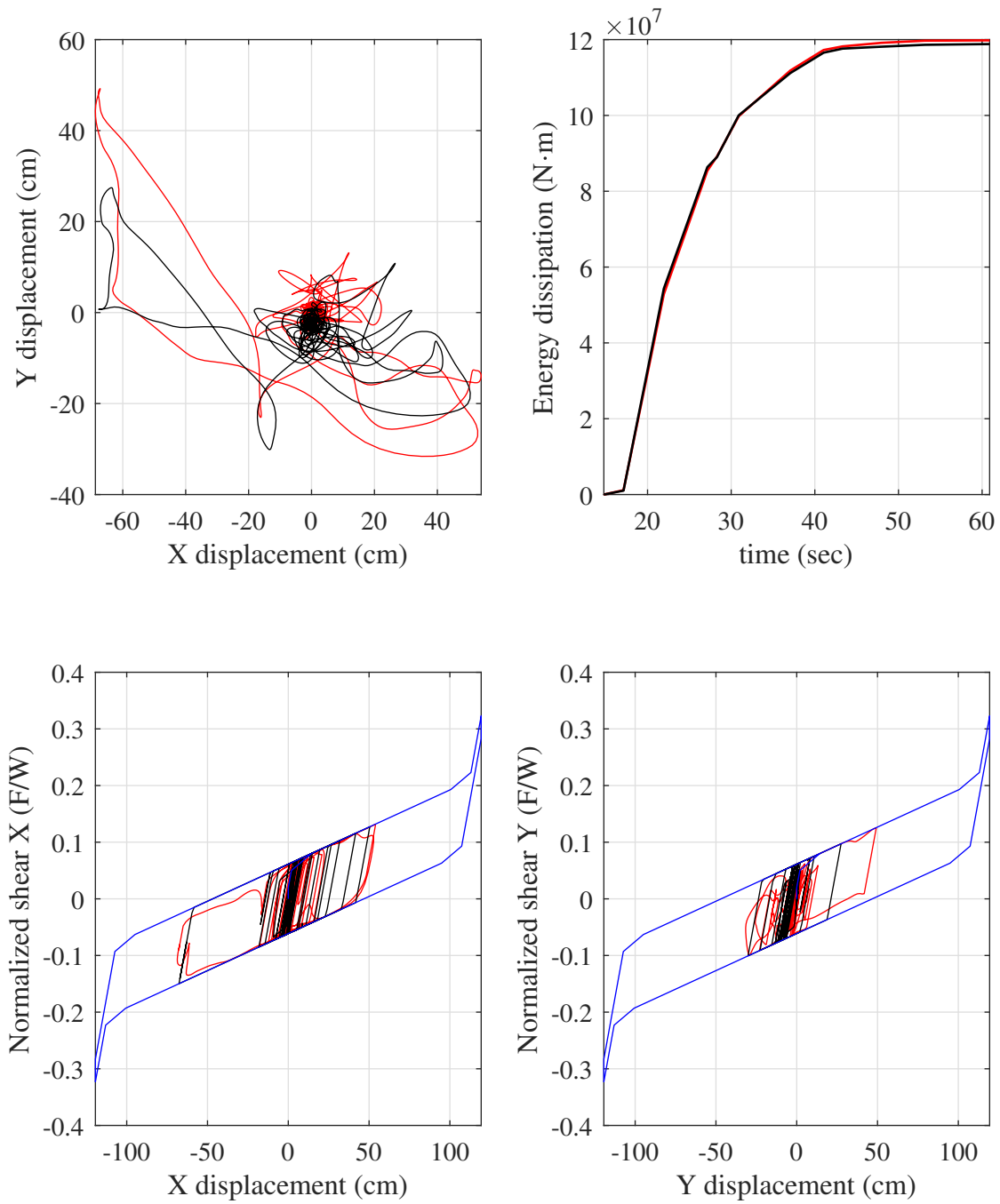


Figure A.1: Displacement orbit of Darfield @ GDLC earthquake (a), energy dissipation (b) and hysteresis of the TFP bearings (c)(d).

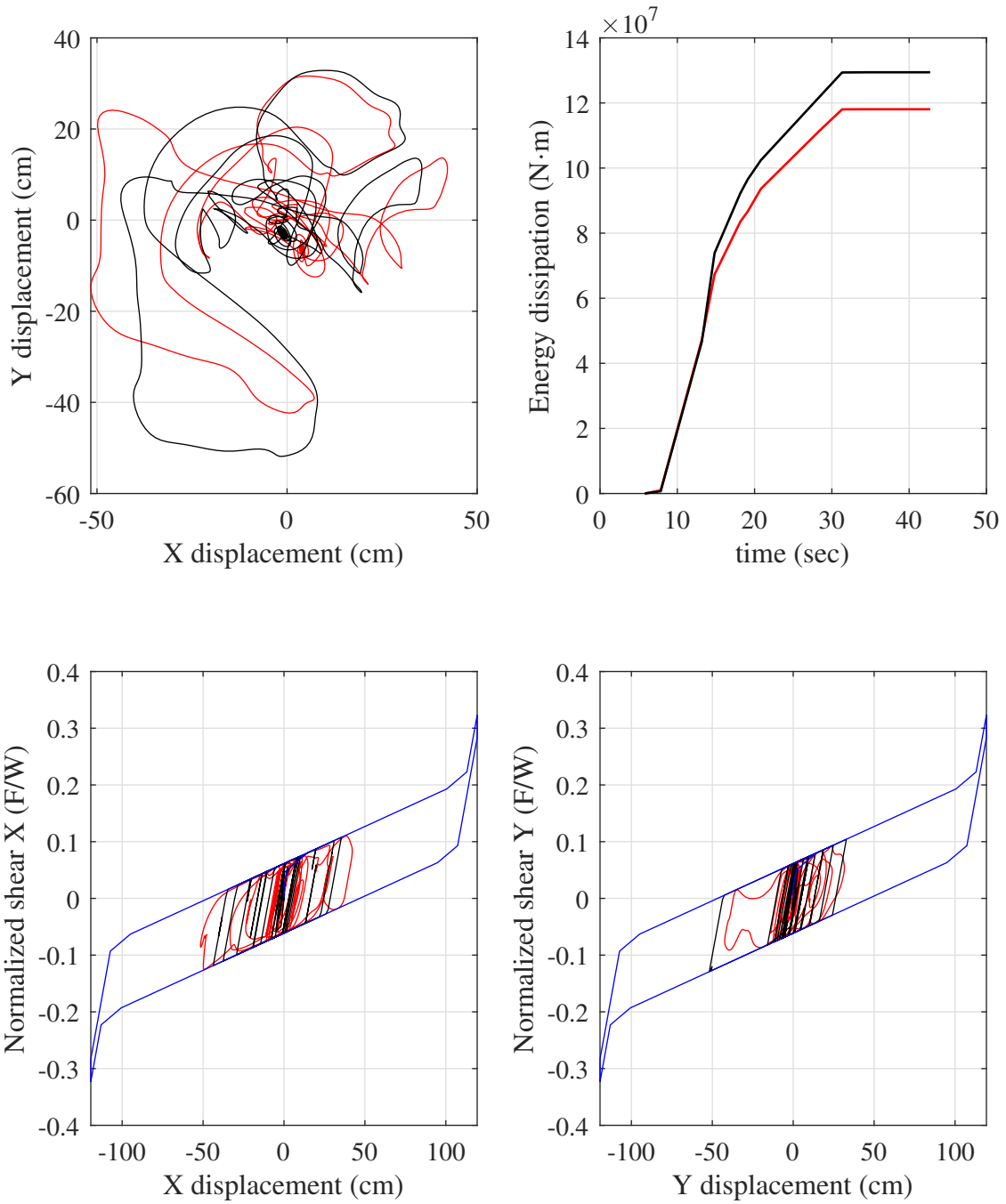


Figure A.2: Displacement orbit of Duzce @ Duzce earthquake (a), energy dissipation (b) and hysteresis of the TFP bearings (c)(d).

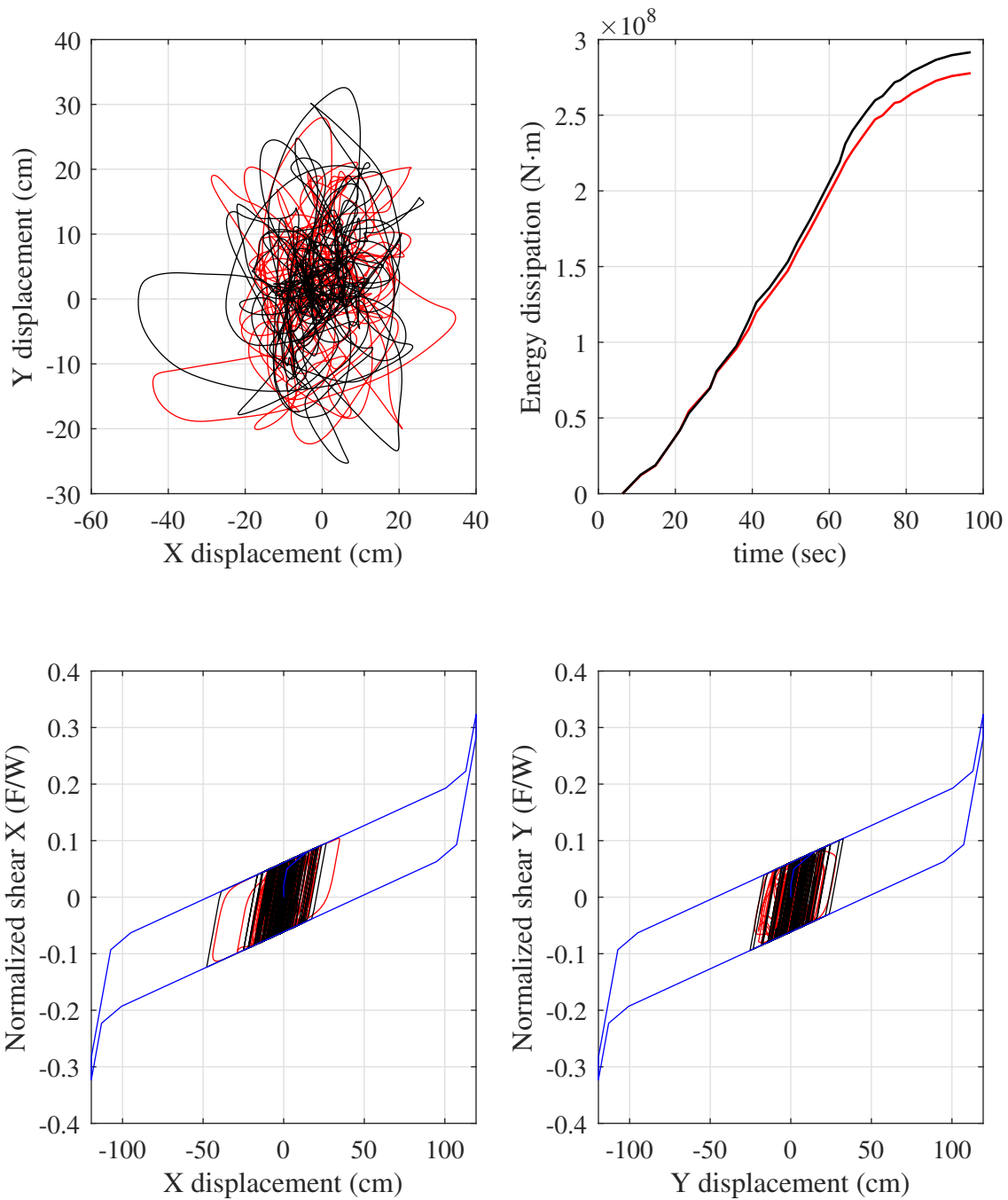


Figure A.3: Displacement orbit of Imperial Valley @ Delta earthquake (a), energy dissipation (b) and hysteresis of the TFP bearings (c)(d).

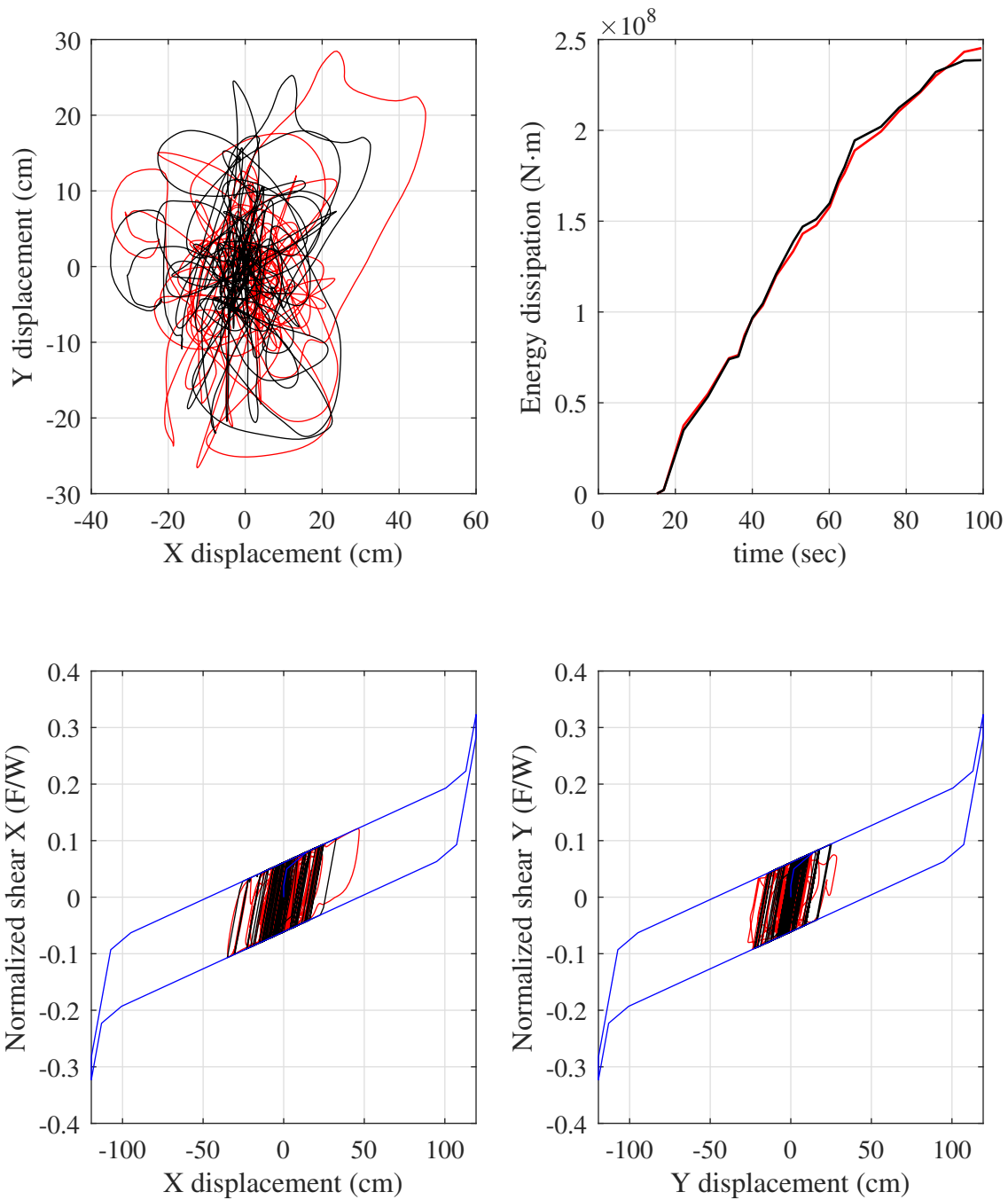


Figure A.4: Displacement orbit of Kobe @ Abeno earthquake (a), energy dissipation (b) and hysteresis of the TFP bearings (c)(d).

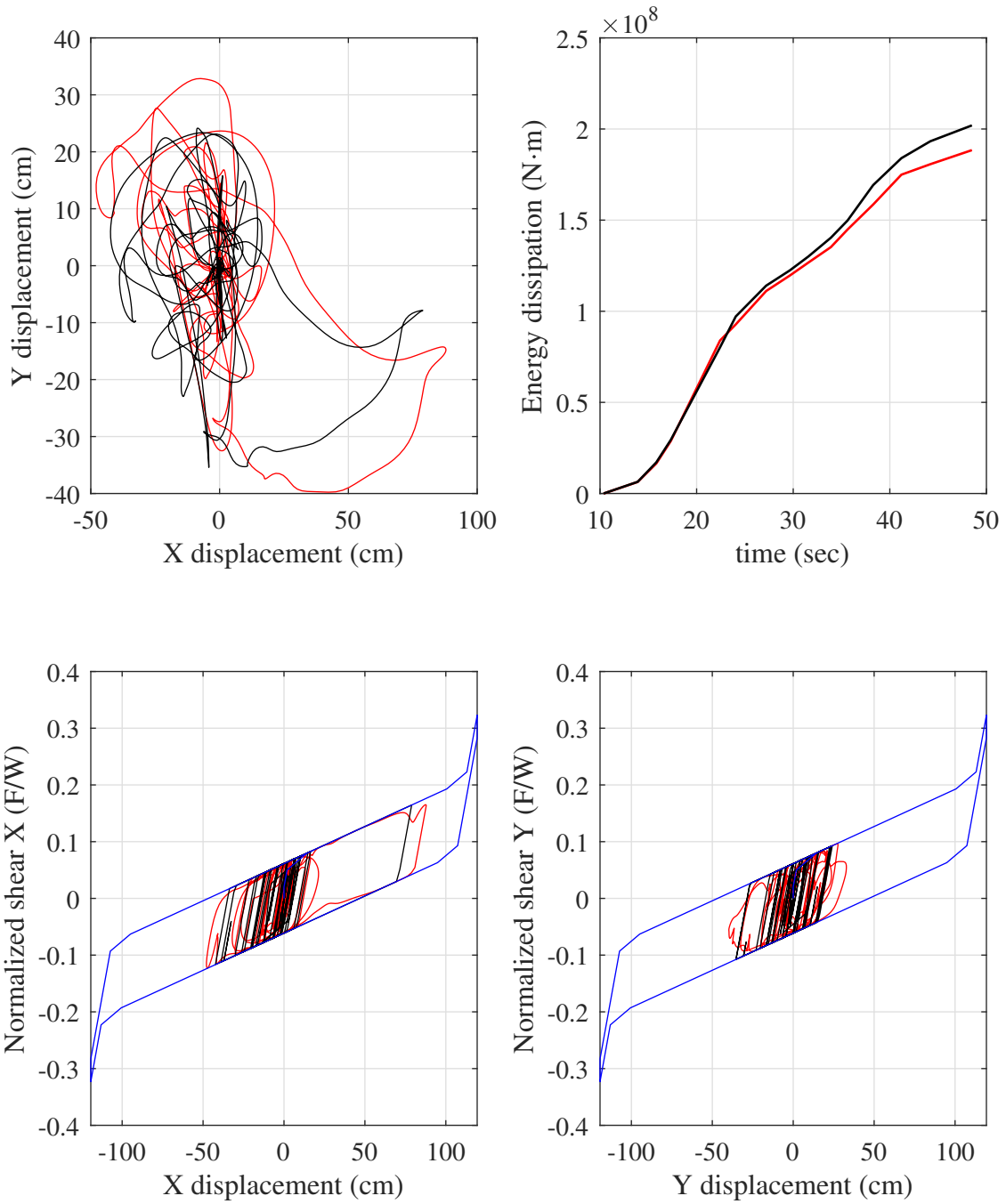


Figure A.5: Displacement orbit of Landers @ Yermo Fire Station earthquake (a), energy dissipation (b) and hysteresis of the TFP bearings (c)(d).

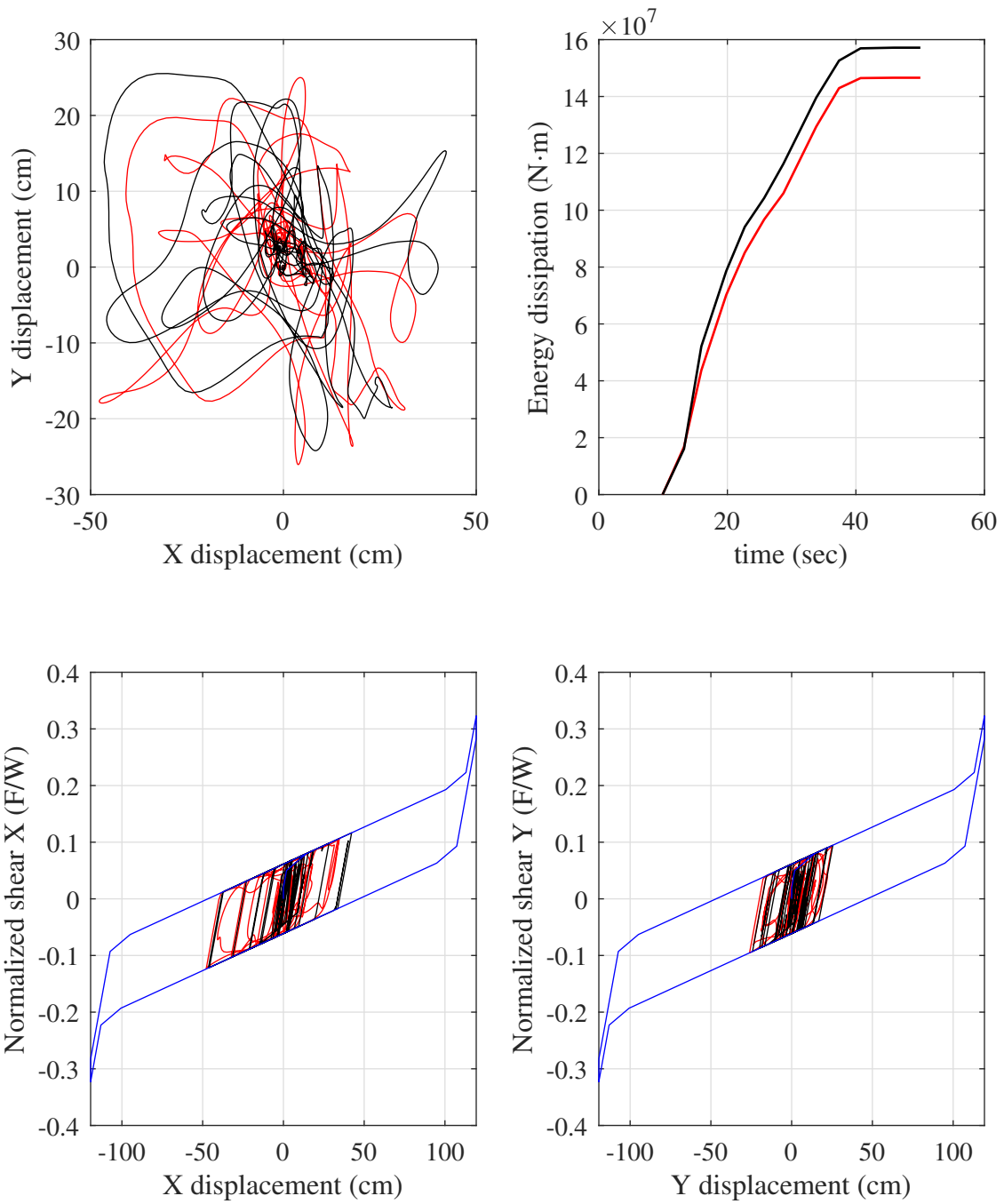


Figure A.6: Displacement orbit of Superstition Hills @ EI Centro earthquake (a), energy dissipation (b) and hysteresis of the TFP bearings (c)(d).

APPENDIX B

The Vertical Response Spectra of the Building under 3D Earthquake Excitations

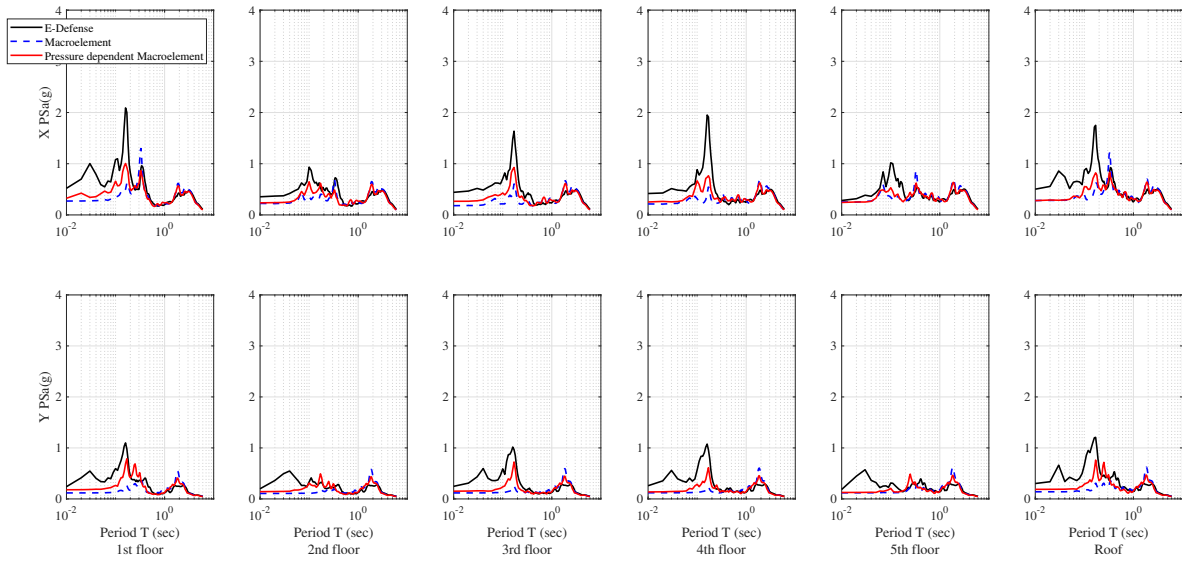


Figure B.1: The horizontal response spectra of the building under Loma Prieta @ Los Gatos Pres. Ctr. earthquake (Northwest).

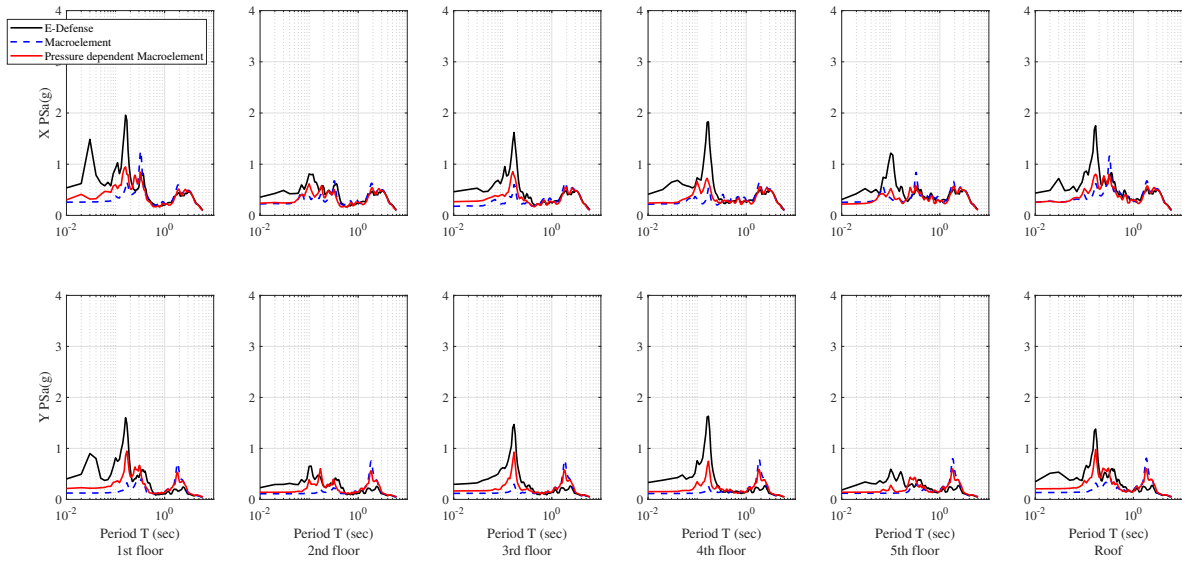


Figure B.2: The horizontal response spectra of the building under Loma Prieta @ Los Gatos Pres. Ctr. earthquake (Southeast).

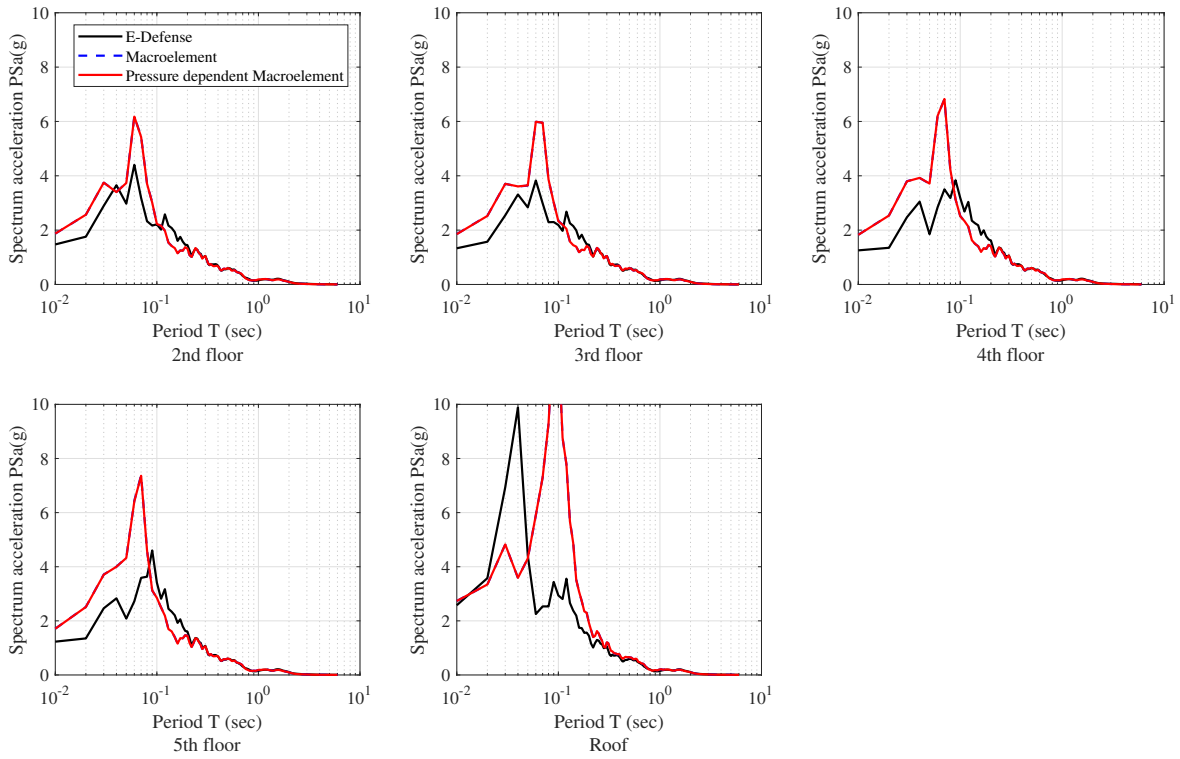


Figure B.3: The vertical response spectra of the building under Loma Prieta @ Los Gatos Pres. Ctr. earthquake (Northwest).

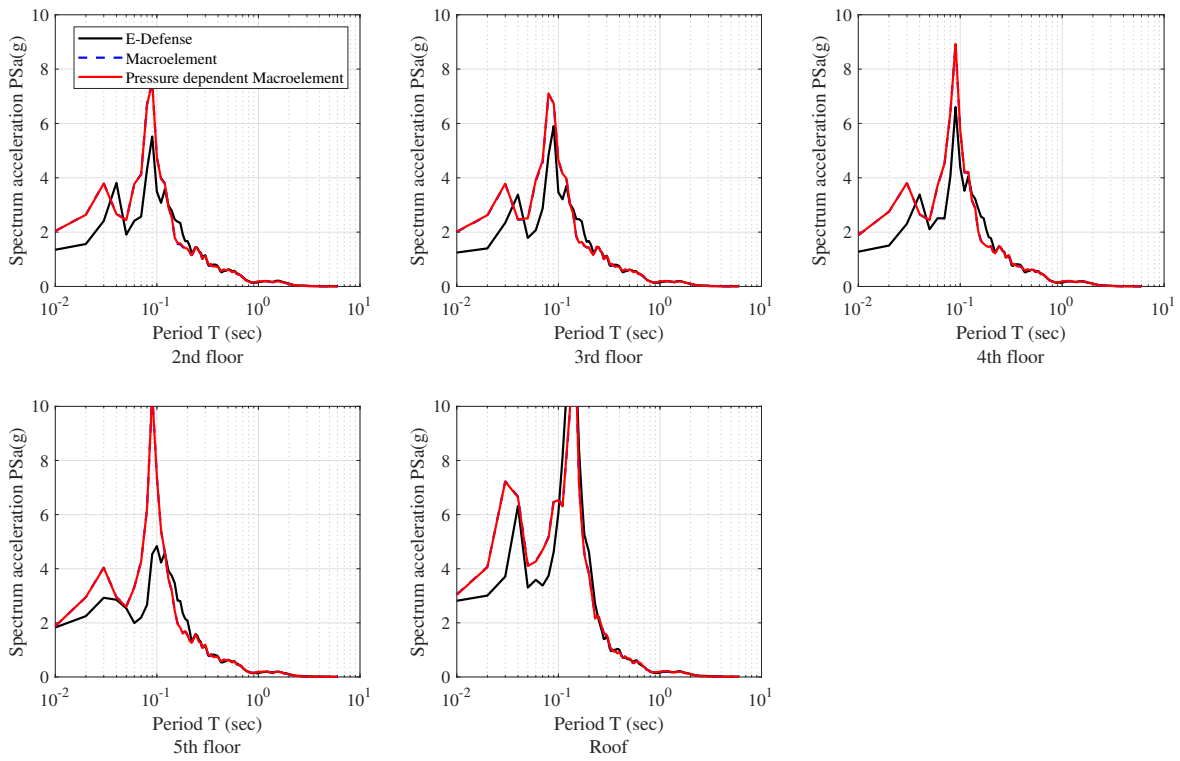


Figure B.4: The vertical response spectra of the building under Loma Prieta @ Los Gatos Pres. Ctr. earthquake (Northeast).

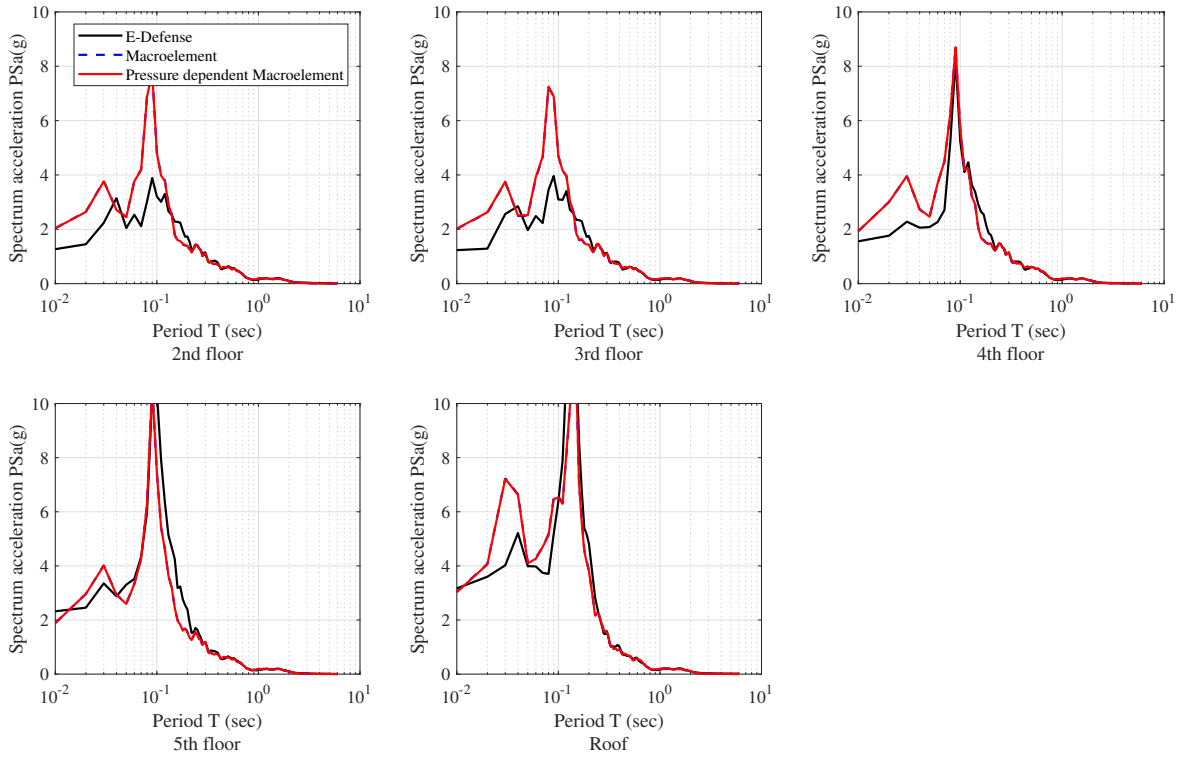


Figure B.5: The vertical response spectra of the building under Loma Prieta @ Los Gatos Pres. Ctr. earthquake (Southeast).

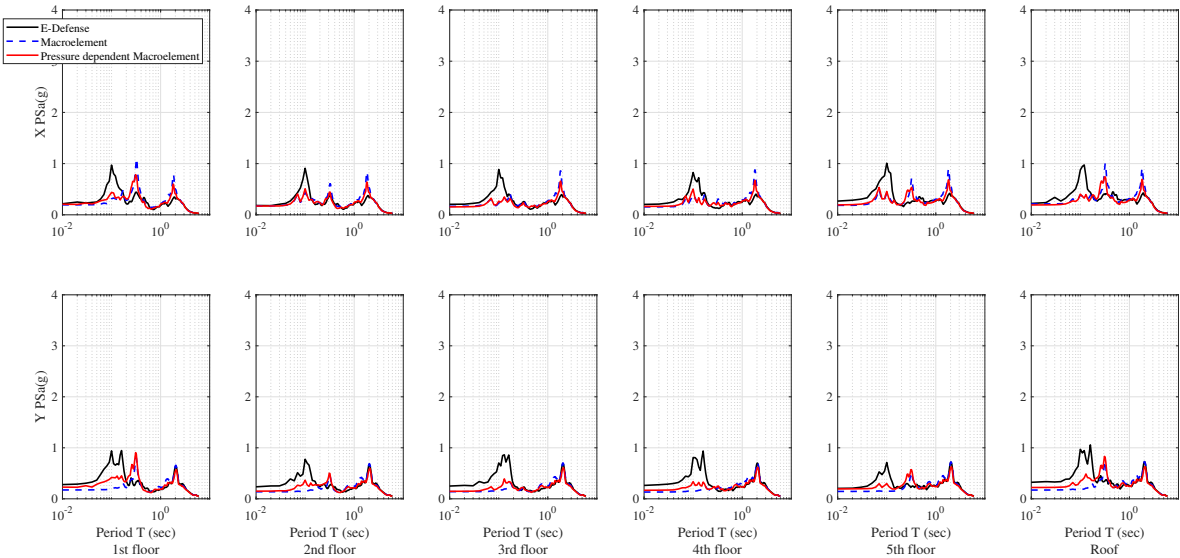


Figure B.6: The horizontal response spectra of the building under Imperial Valley @ Westmorland earthquake (Northwest).

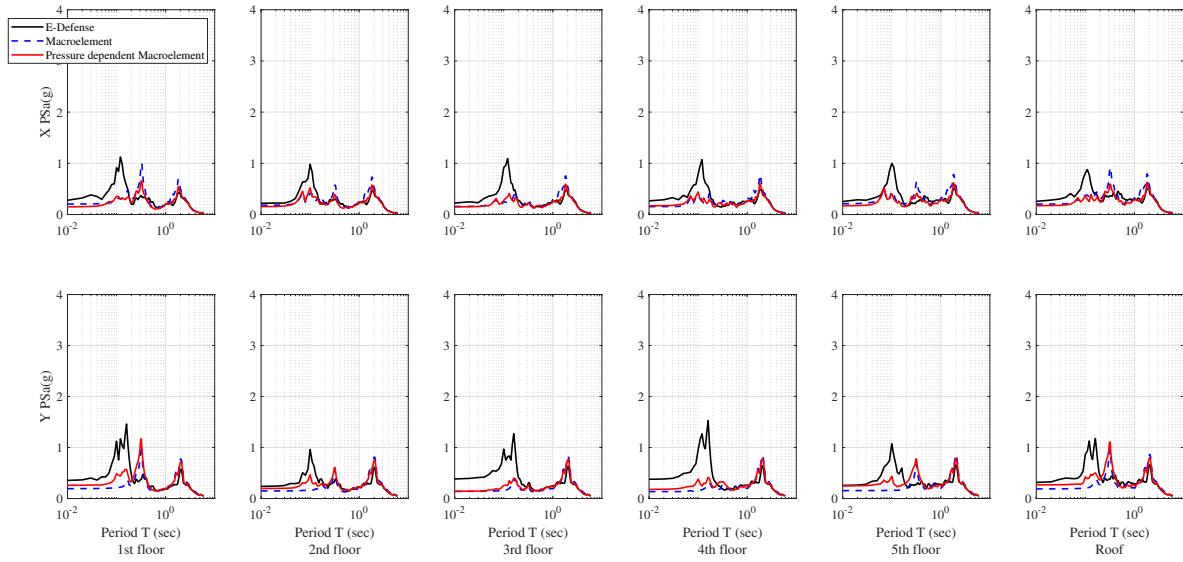


Figure B.7: The horizontal response spectra of the building under Imperial Valley @ Westmorland earthquake (Southeast).

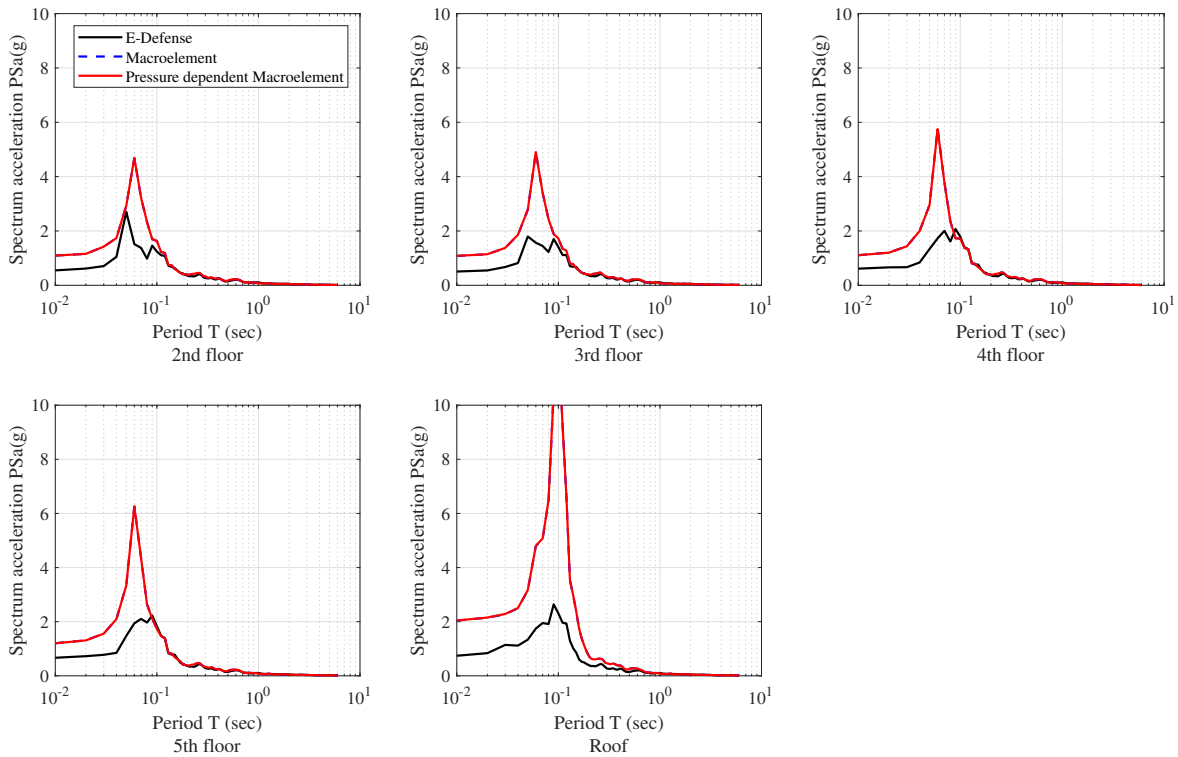


Figure B.8: The vertical response spectra of the building under Imperial Valley @ Westmorland earthquake (Northwest).

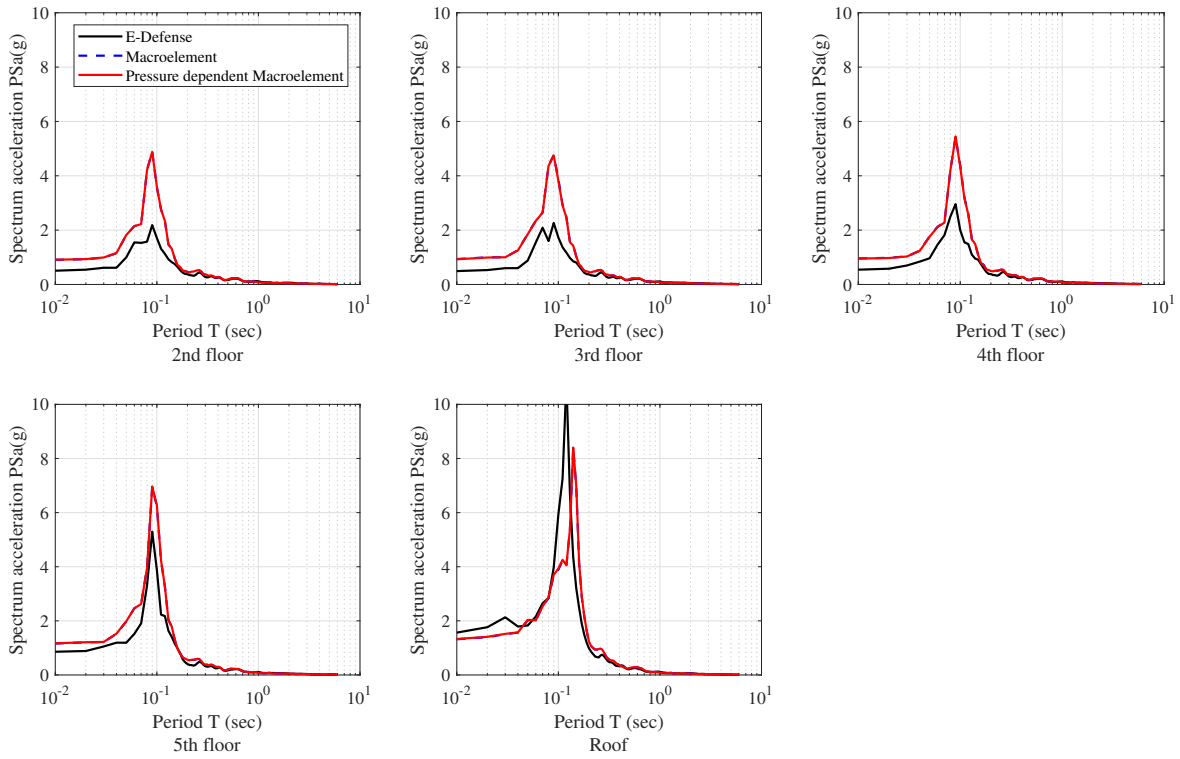


Figure B.9: The vertical response spectra of the building under Imperial Valley @ Westmorland earthquake (Northeast).

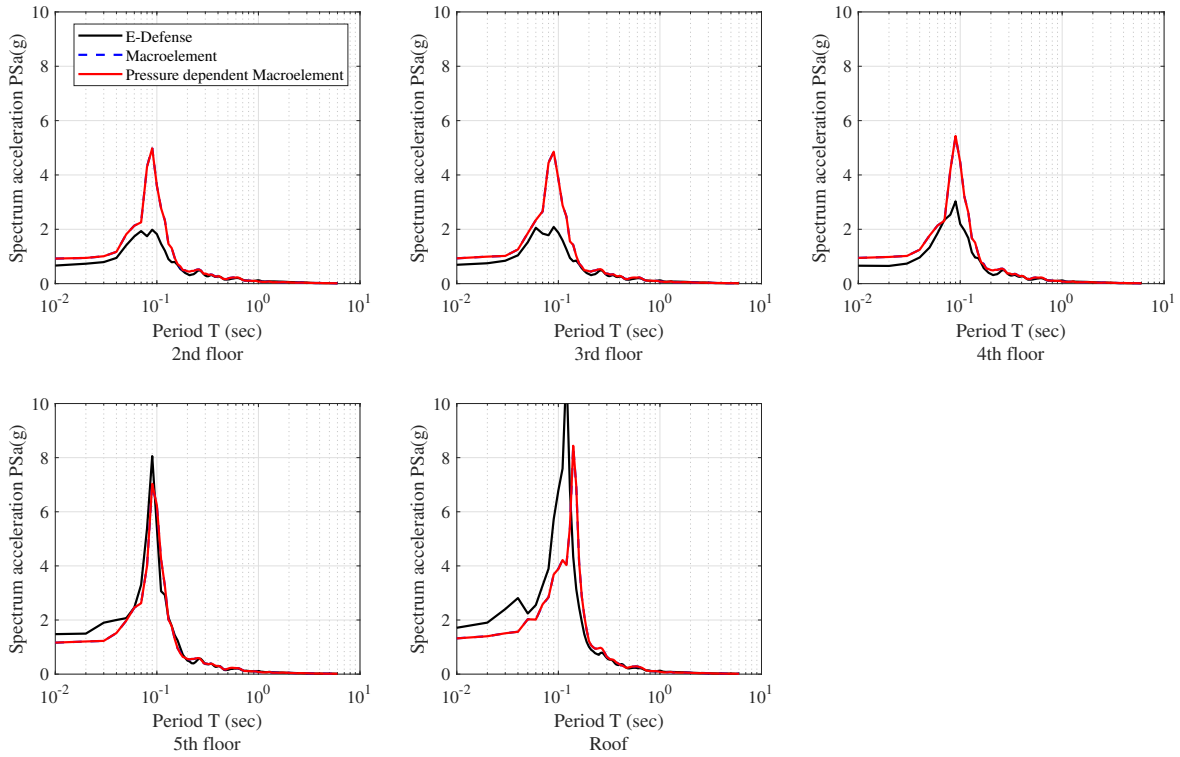


Figure B.10: The vertical response spectra of the building under Imperial Valley @ Westmorland earthquake (Southeast).

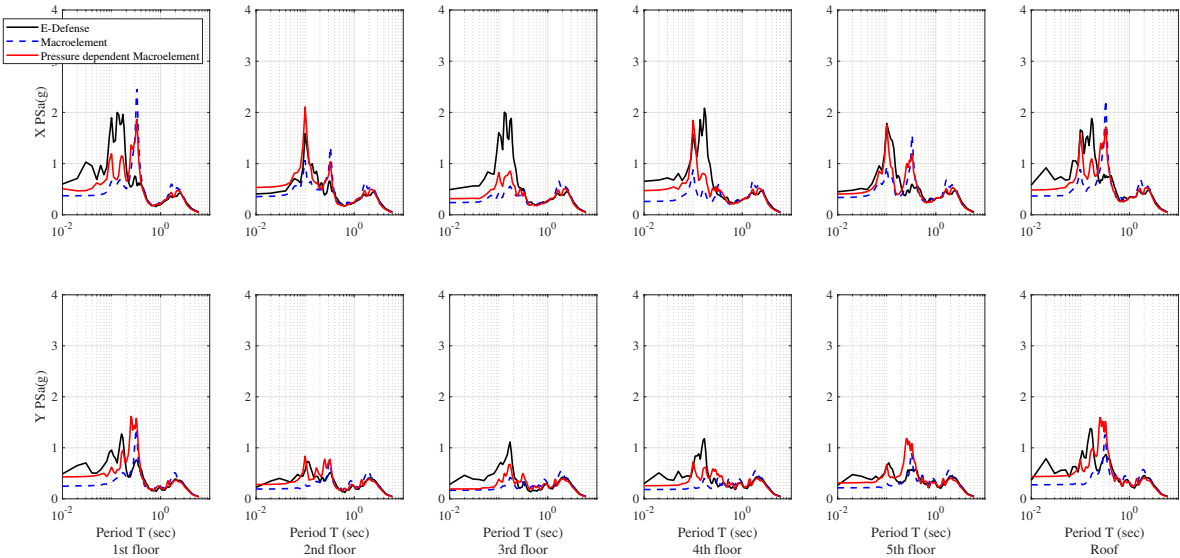


Figure B.11: The horizontal response spectra of the building under Kobe @ Takatori earthquake (Northwest).

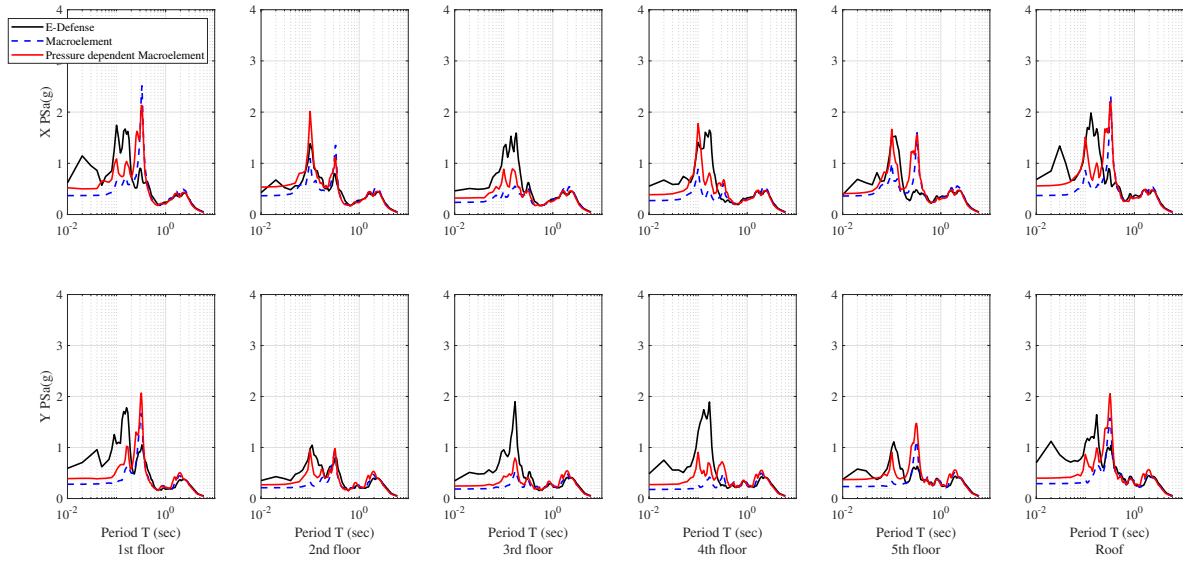


Figure B.12: The horizontal response spectra of the building under Kobe @ Takatori earthquake (Southeast).

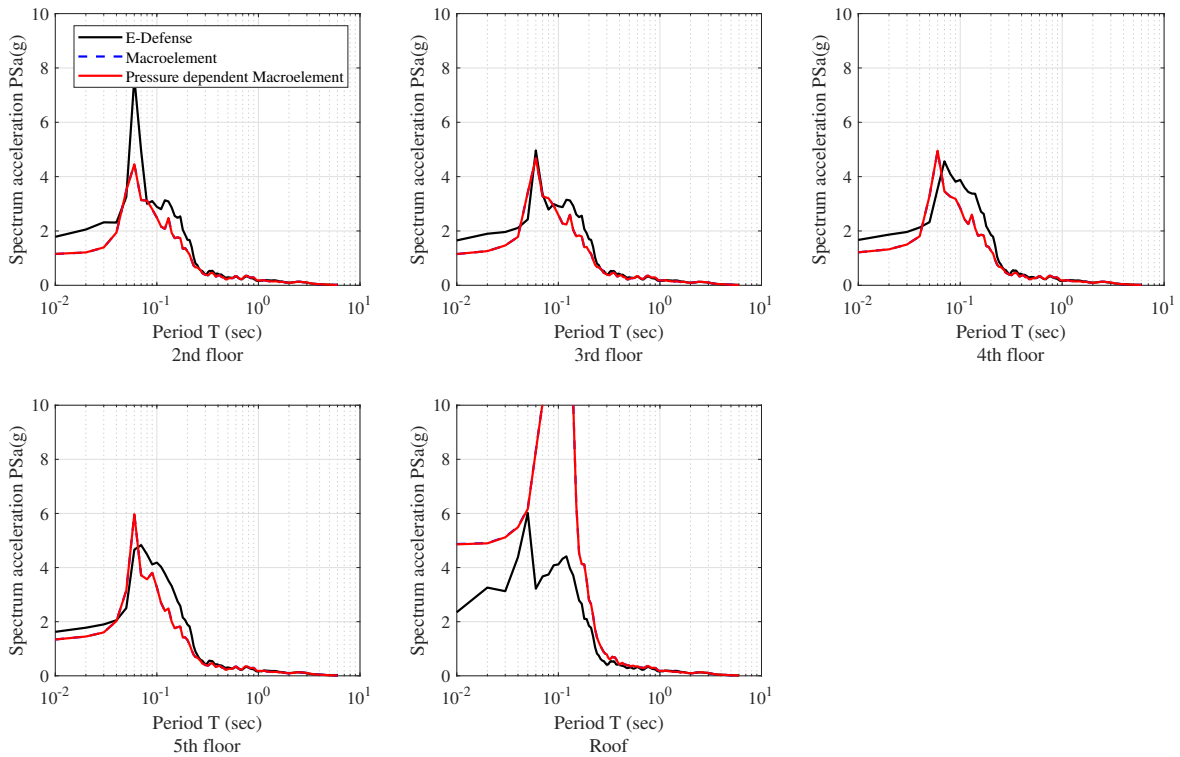


Figure B.13: The vertical response spectra of the building under Kobe @ Takatori earthquake (Northwest).

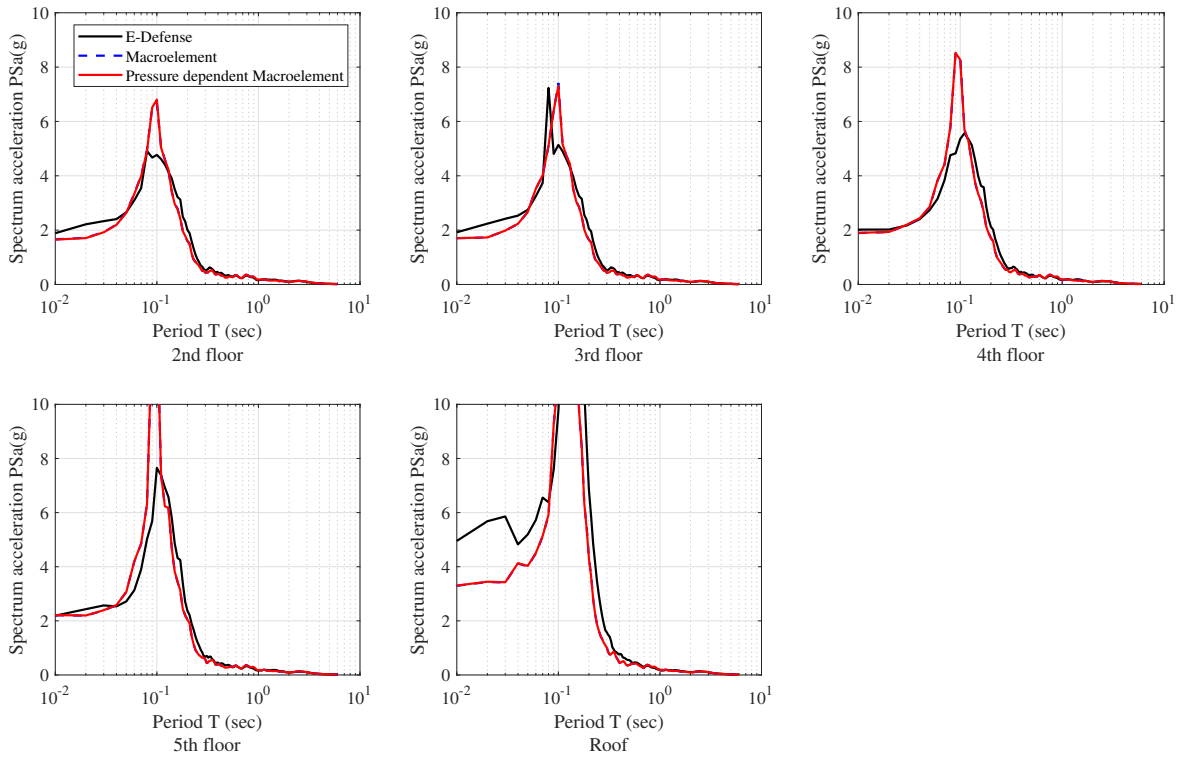


Figure B.14: The vertical response spectra of the building under Kobe @ Takatori earthquake (Northeast).

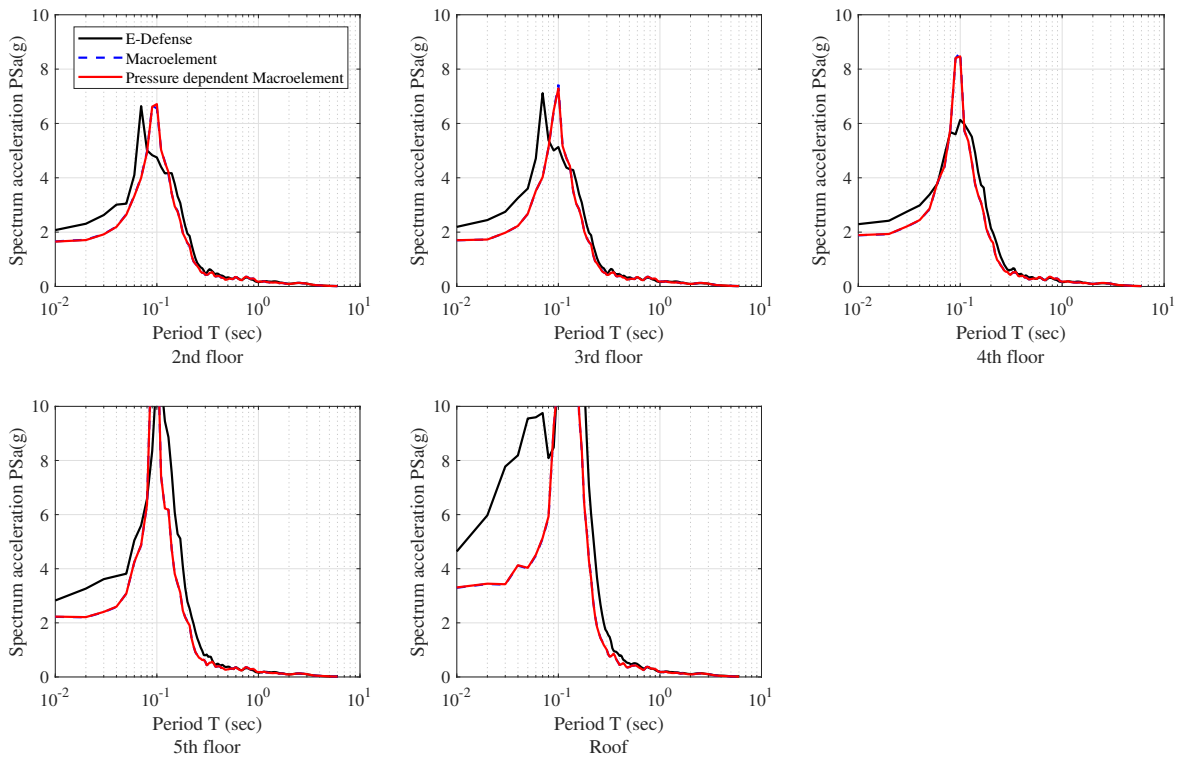


Figure B.15: The vertical response spectra of the building under Kobe @ Takatori earthquake (Southeast).

APPENDIX C

The Hysteresis of TFP Bearings, the Peak Inter-story Drift Ratio and the Maximum Floor Acceleration of E-Defense Building under Earthquakes.

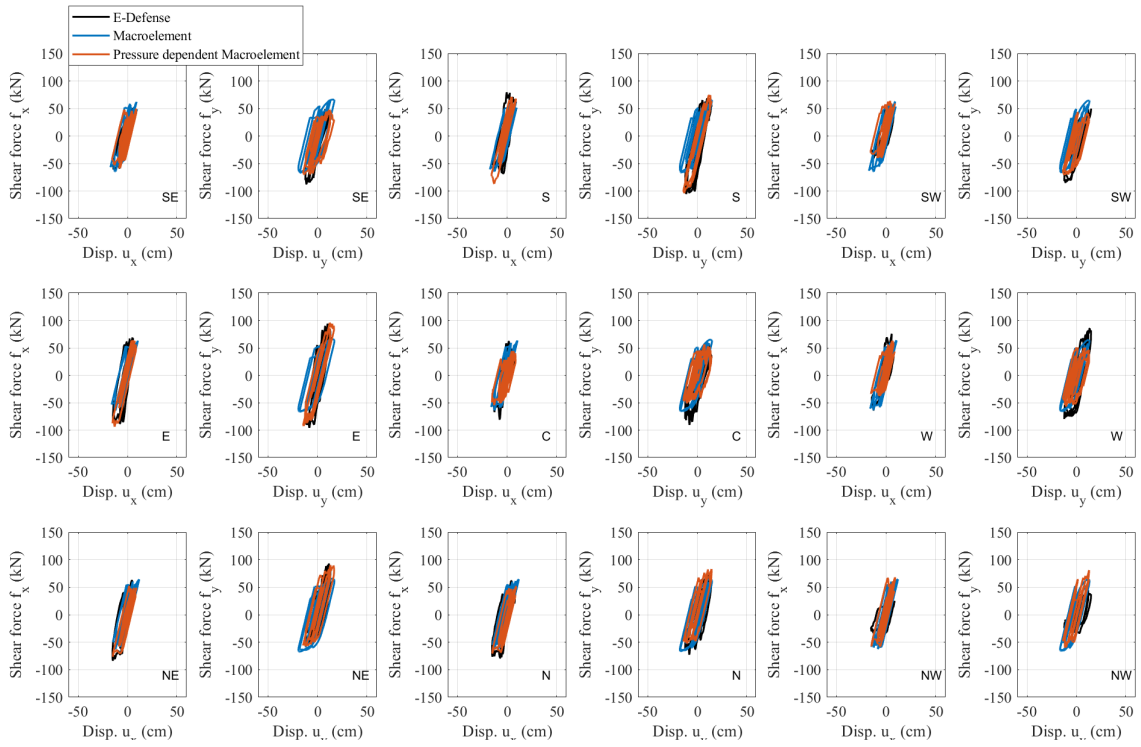


Figure C.1: The hysteresis of TFP bearings under Imperial Valley @ Westmorland earthquake.

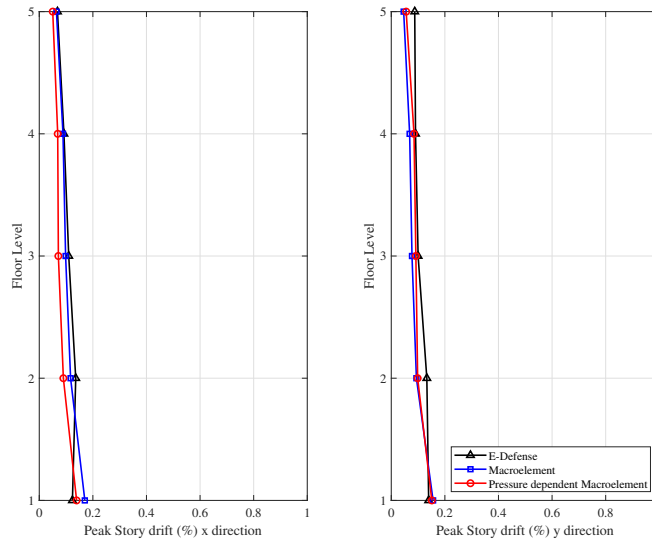


Figure C.2: The peak inner-story drift ratio of E-Defense building under Imperial Valley @ Westmorland earthquake.

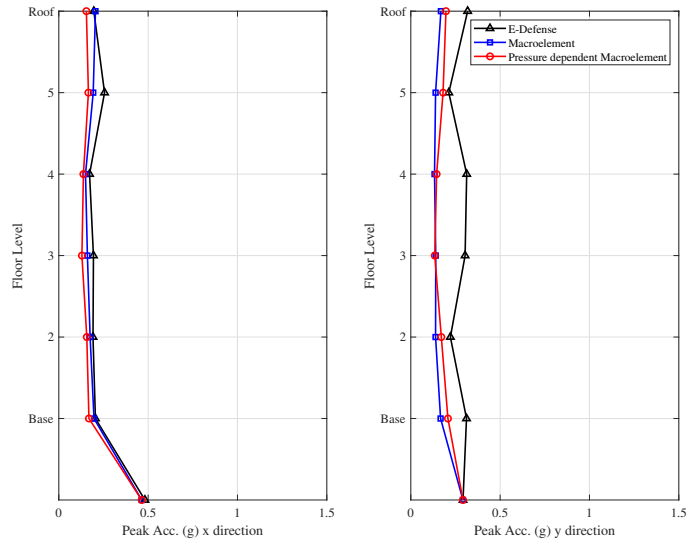


Figure C.3: The peak floor acceleration of E-Defense building under Imperial Valley @ Westmorland earthquake.

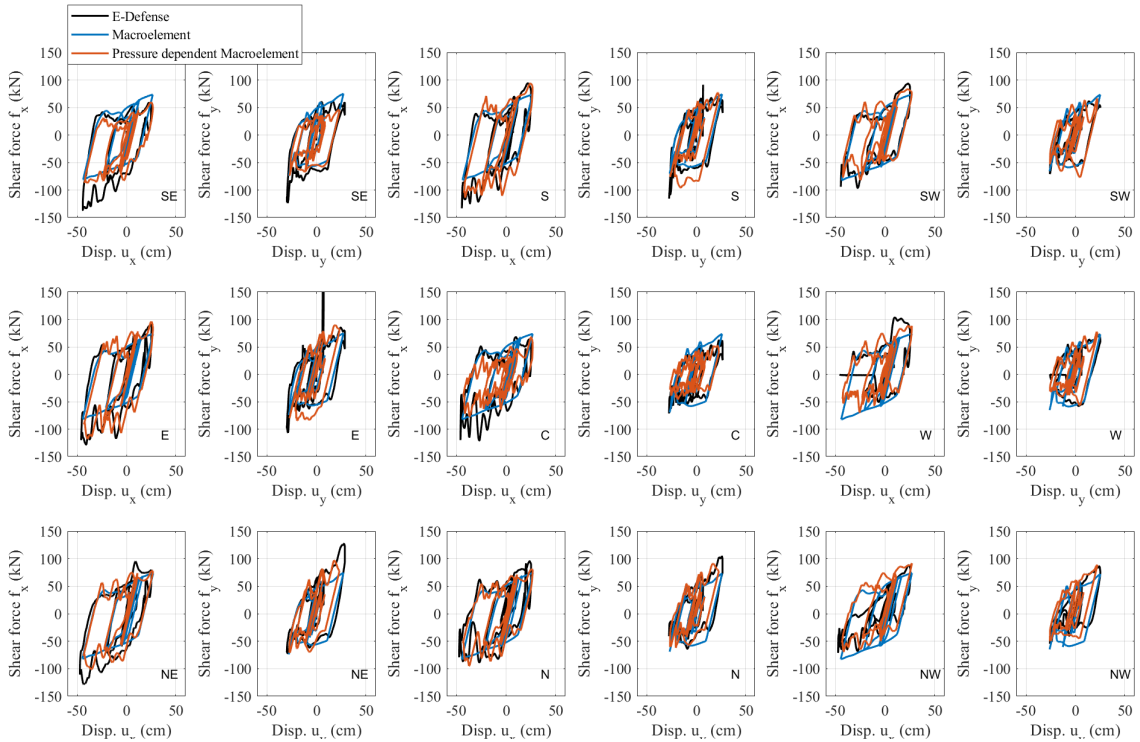


Figure C.4: The hysteresis of TFP bearings under Northridge @ Sylmar earthquake.

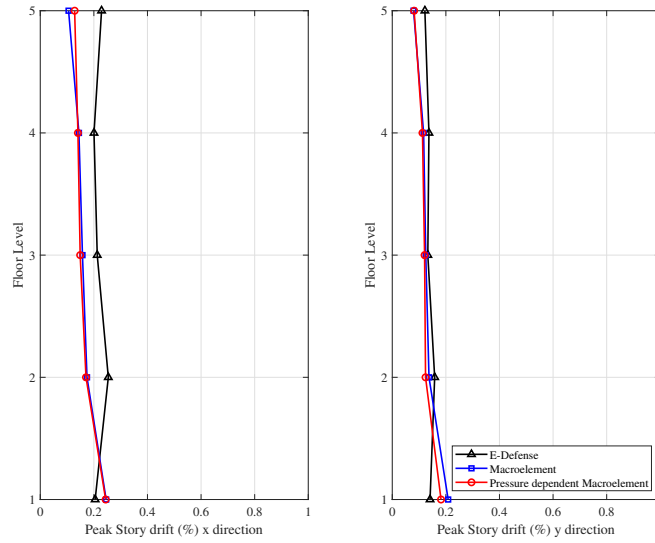


Figure C.5: The peak inner-story drift ratio of E-Defense building under Northridge @ Sylmar earthquake.

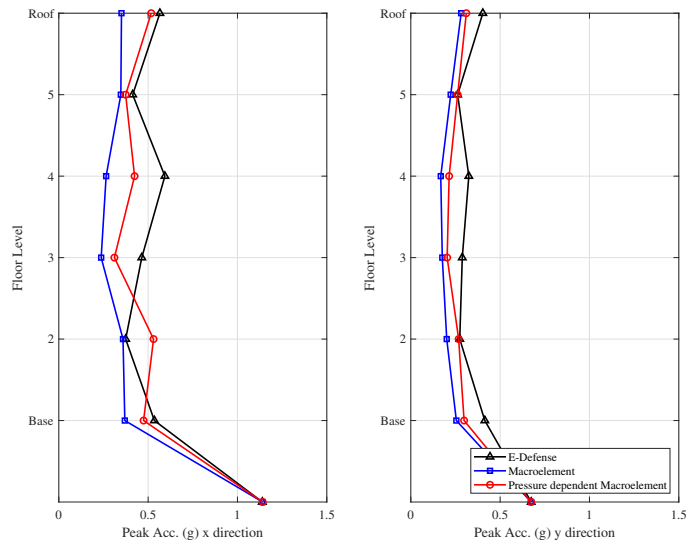


Figure C.6: The peak floor acceleration of E-Defense building under Northridge @ Sylmar earthquake.

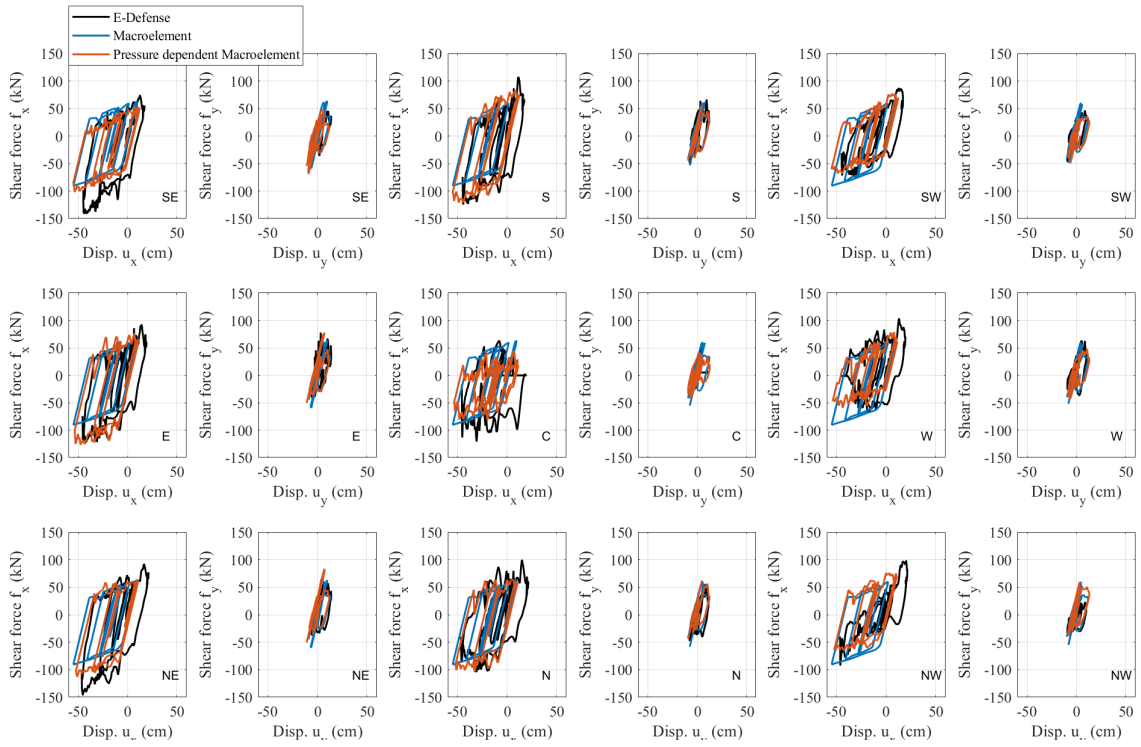


Figure C.7: The hysteresis of TFP bearings under Loma Prieta @ Los Gatos Pres. Ctr. earthquake.

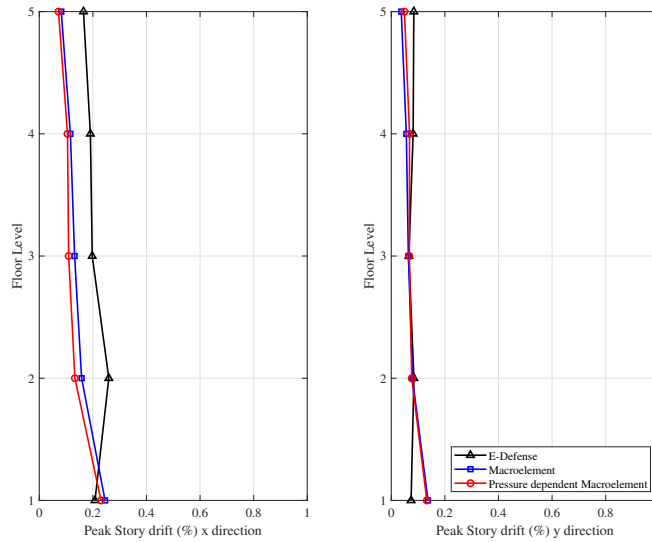


Figure C.8: The peak inner-story drift ratio of E-Defense building under Loma Prieta @ Los Gatos Pres. Ctr. earthquake.

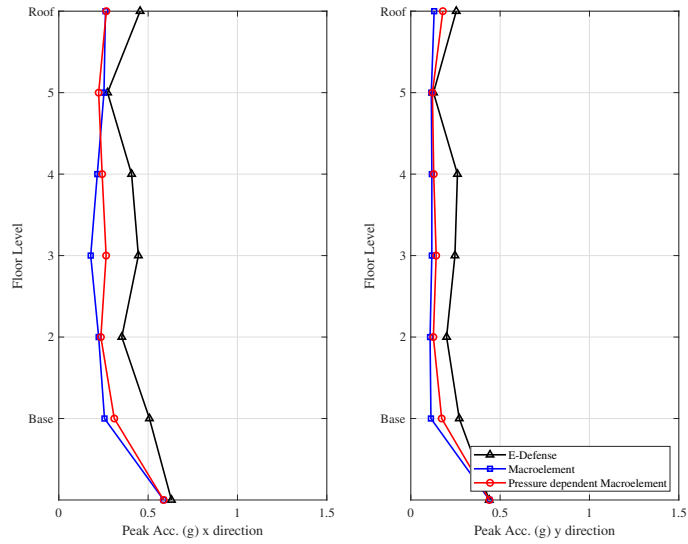


Figure C.9: The peak floor acceleration of E-Defense building under Loma Prieta @ Los Gatos Pres. Ctr. earthquake.

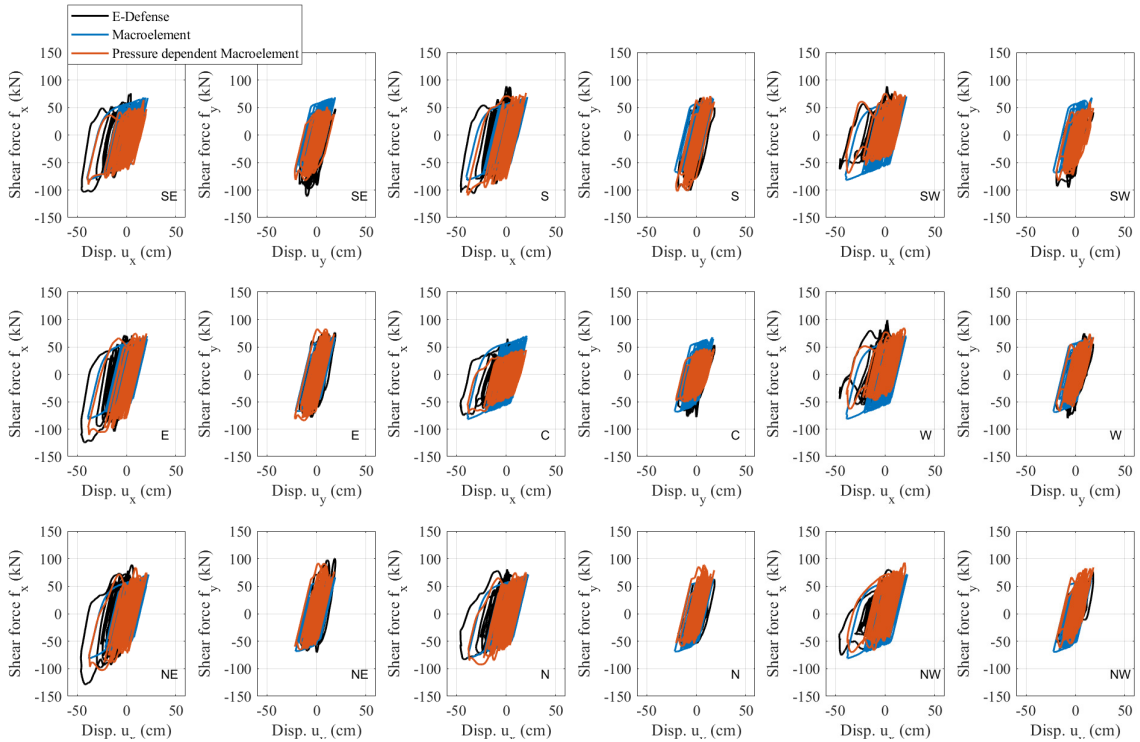


Figure C.10: The hysteresis of TFP bearings under Tohoku @ Iwanuma earthquake.

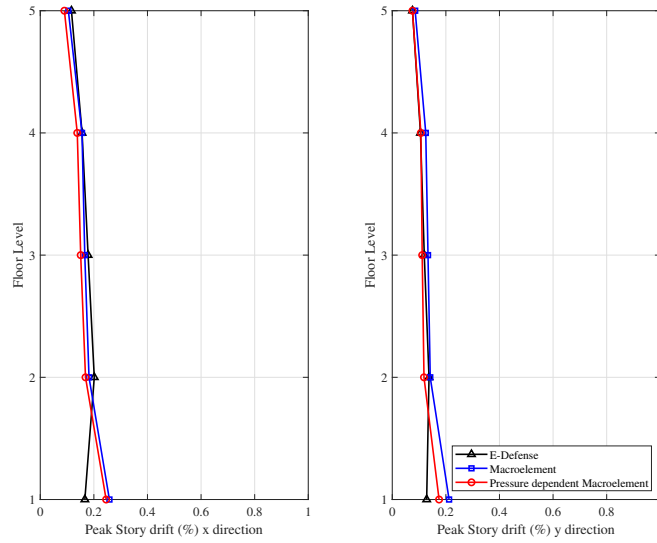


Figure C.11: The peak inner-story drift ratio of E-Defense building under Tohoku @ Iwanuma earthquake.

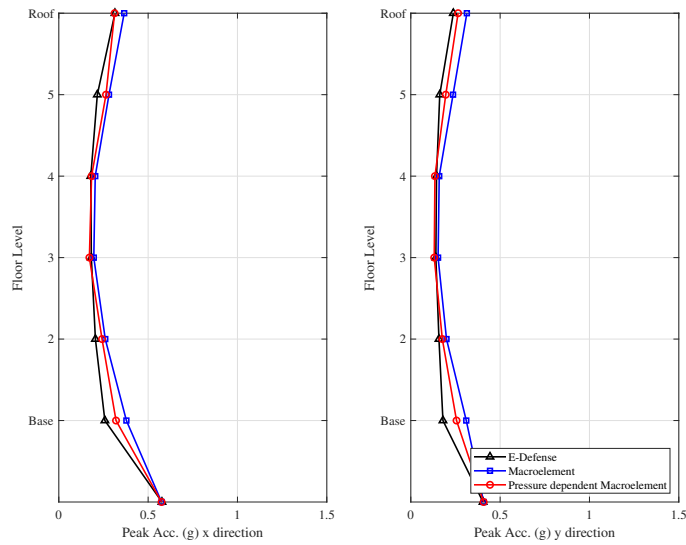


Figure C.12: The peak floor acceleration of E-Defense building under Tohoku @ Iwanuma earthquake.

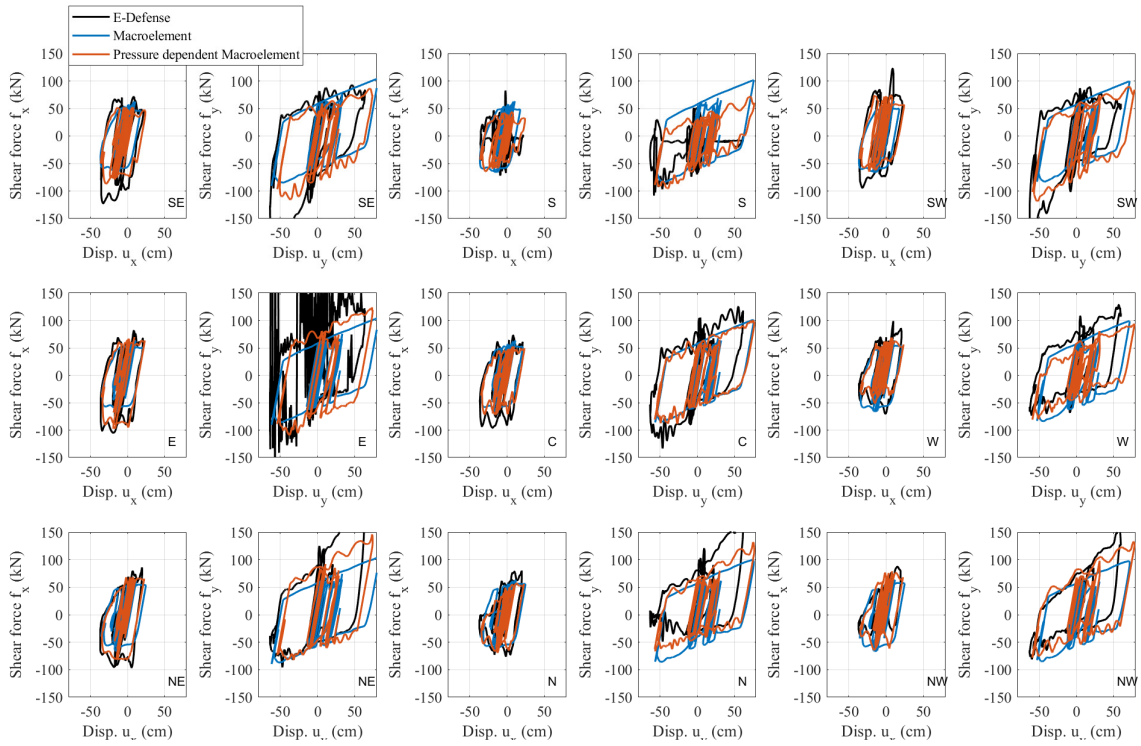


Figure C.13: The hysteresis of TFP bearings under Tabas @ Tabas earthquake.

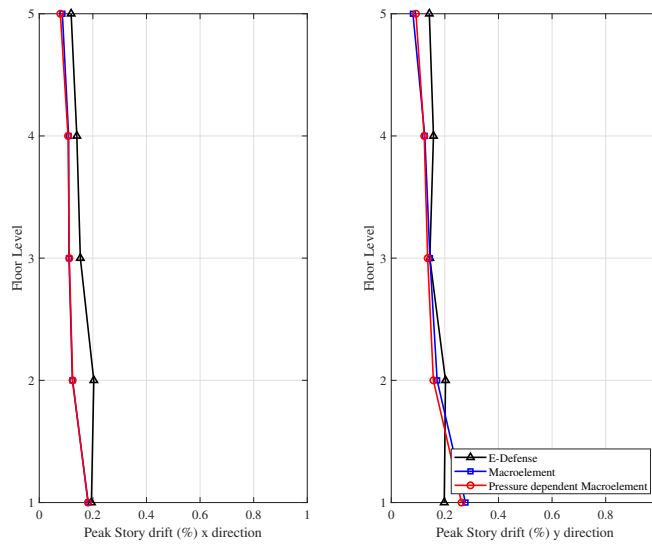


Figure C.14: The peak inner-story drift ratio of E-Defense building under Tabas @ Tabas earthquake.

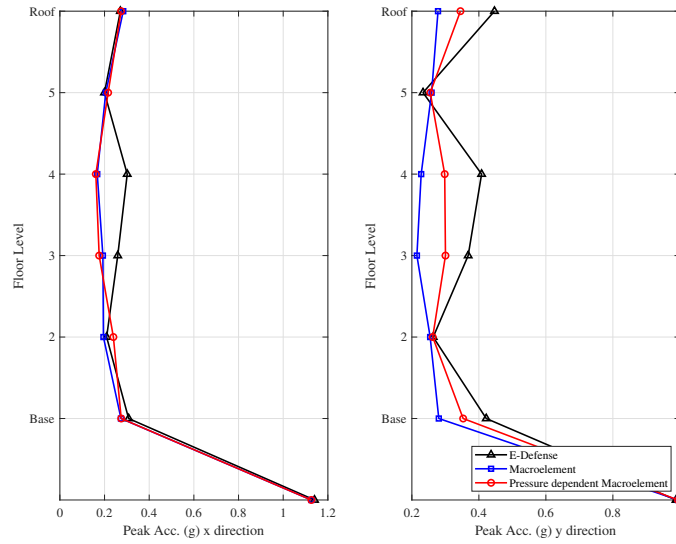


Figure C.15: The peak floor acceleration of E-Defense building under Tabas @ Tabas earthquake.

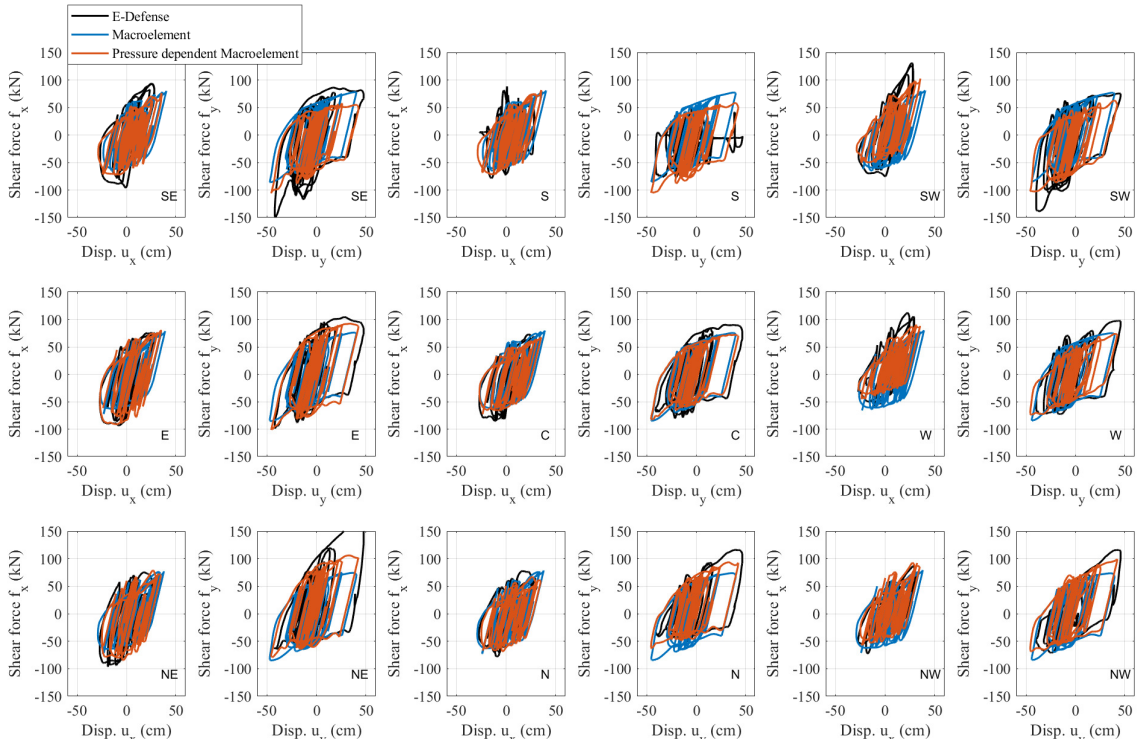


Figure C.16: The hysteresis of TFP bearings under Chi-Chi @ TCU065 earthquake.

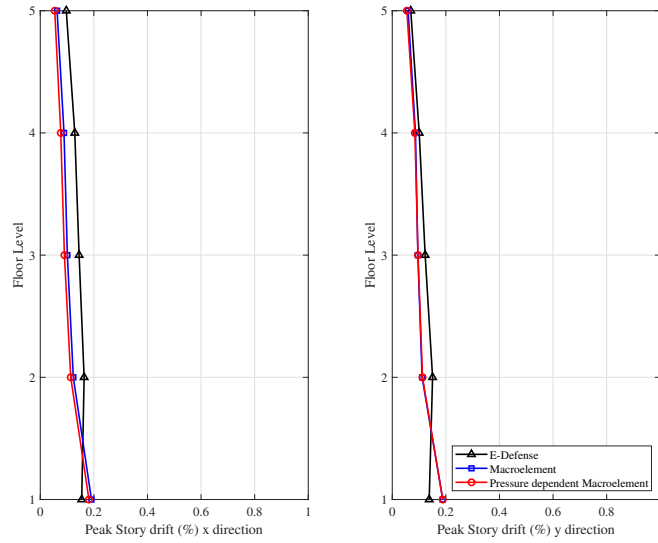


Figure C.17: The peak inner-story drift ratio of E-Defense building under Chi-Chi @ TCU065 earthquake.

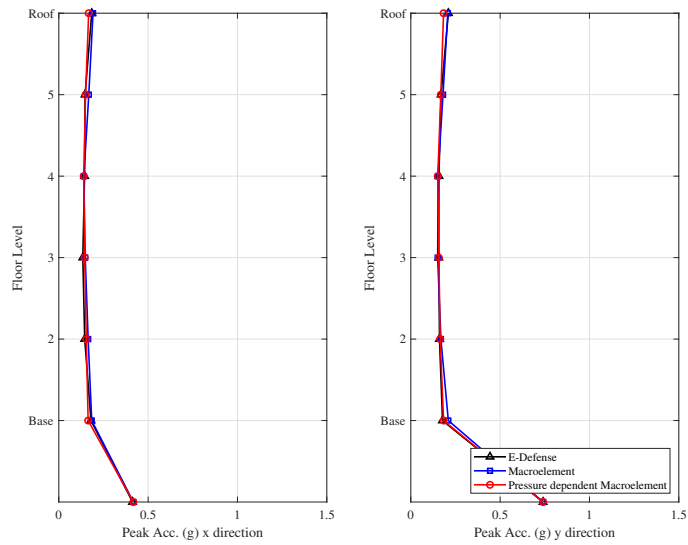


Figure C.18: The peak floor acceleration of E-Defense building under Chi-Chi @ TCU065 earthquake.

APPENDIX D

**The Distribution of the Peak Floor Accelerations and
the Inter-story Drift Ratio for Three Models.**

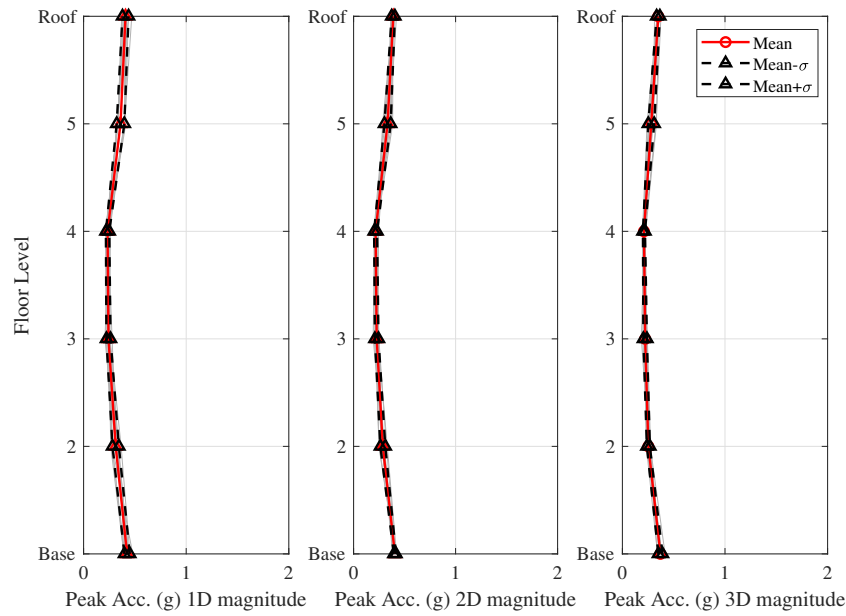


Figure D.1: The distribution of the peak floor accelerations for three models under Chuetsu-Oki @ Yan Sakuramachi City watershed earthquake with different earthquake orientation.

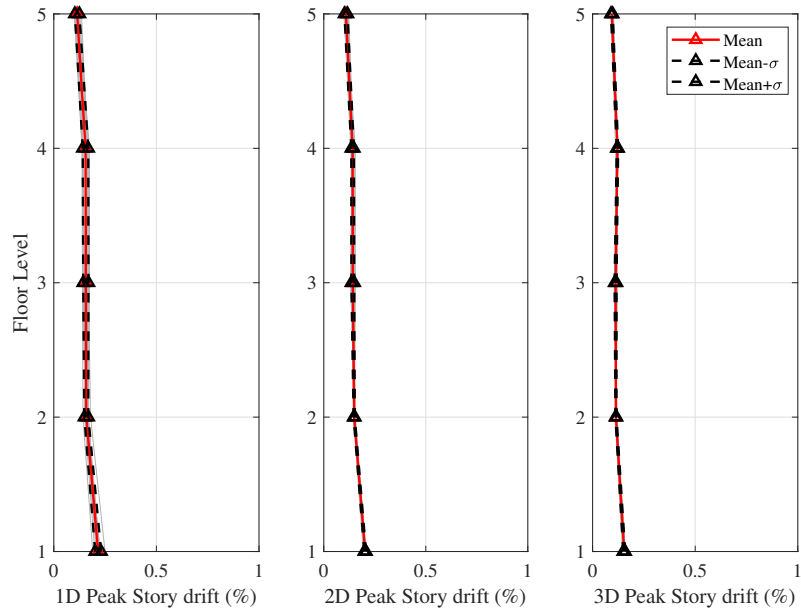


Figure D.2: The distribution of the inter-story drift ratio for three models under Chuetsu-Oki @ Yan Sakuramachi City watershed earthquake with different earthquake orientation.

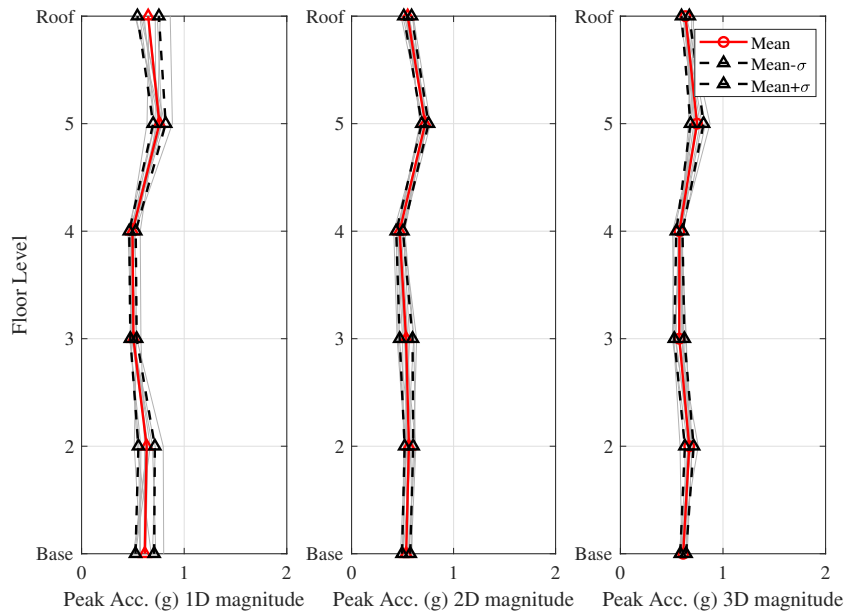


Figure D.3: The distribution of the peak floor accelerations for three models under Landers @ North Palm Springs Fire Sta #36 earthquake with difference earthquake orientation.

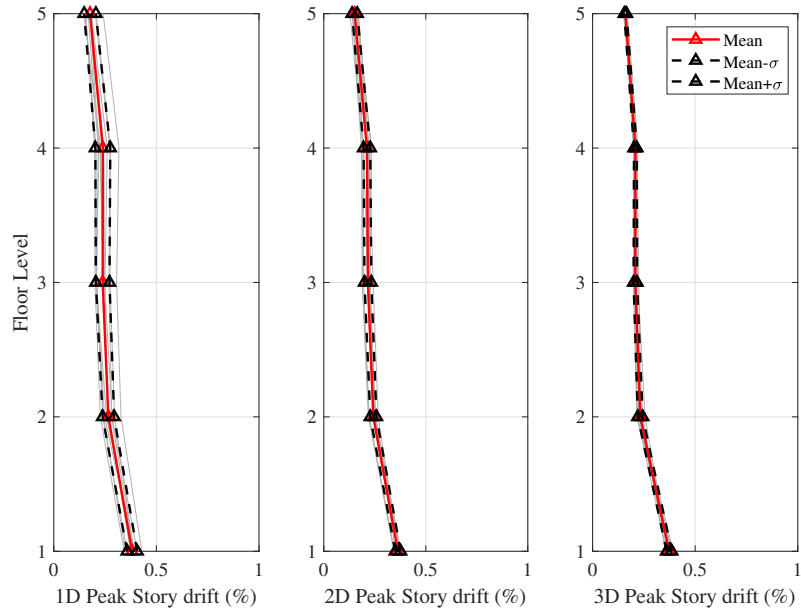


Figure D.4: The distribution of the inter-story drift ratio for three models under Landers @ North Palm Springs Fire Sta #36 earthquake with difference earthquake orientation.

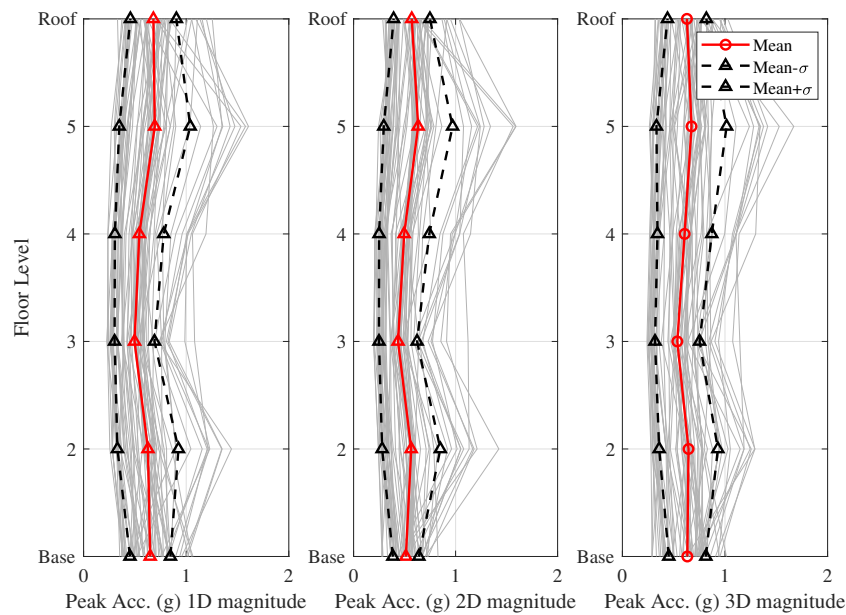


Figure D.5: The distribution of the peak floor accelerations for three models.

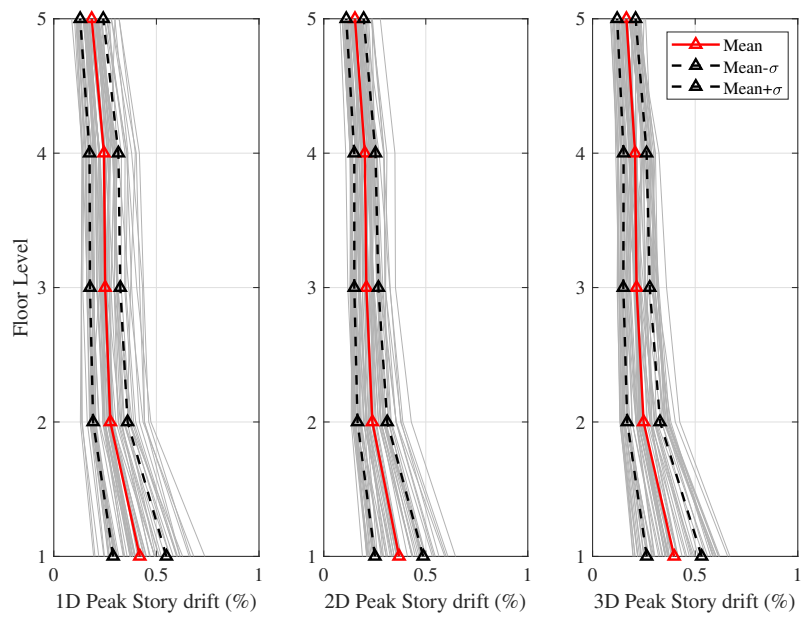


Figure D.6: The distribution of the inter-story drift ratio for three models.

APPENDIX E

Regression Analyses of PSDM

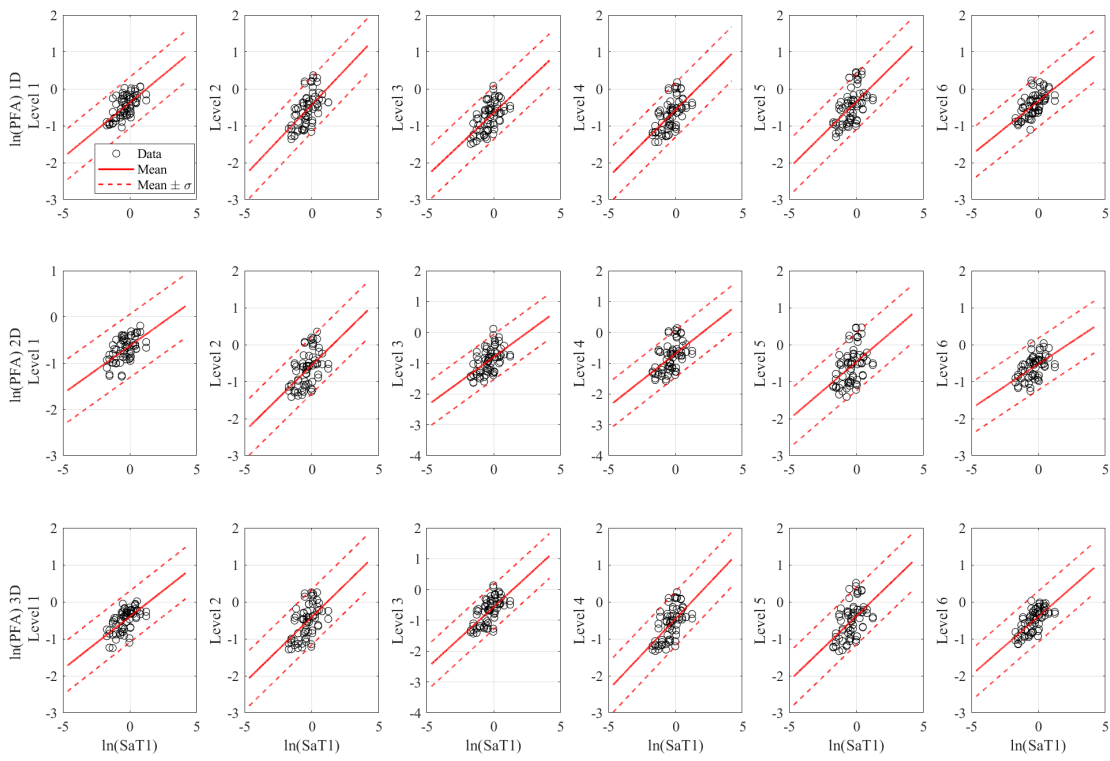


Figure E.1: Regression analyses of SaT1 v.s. PFA

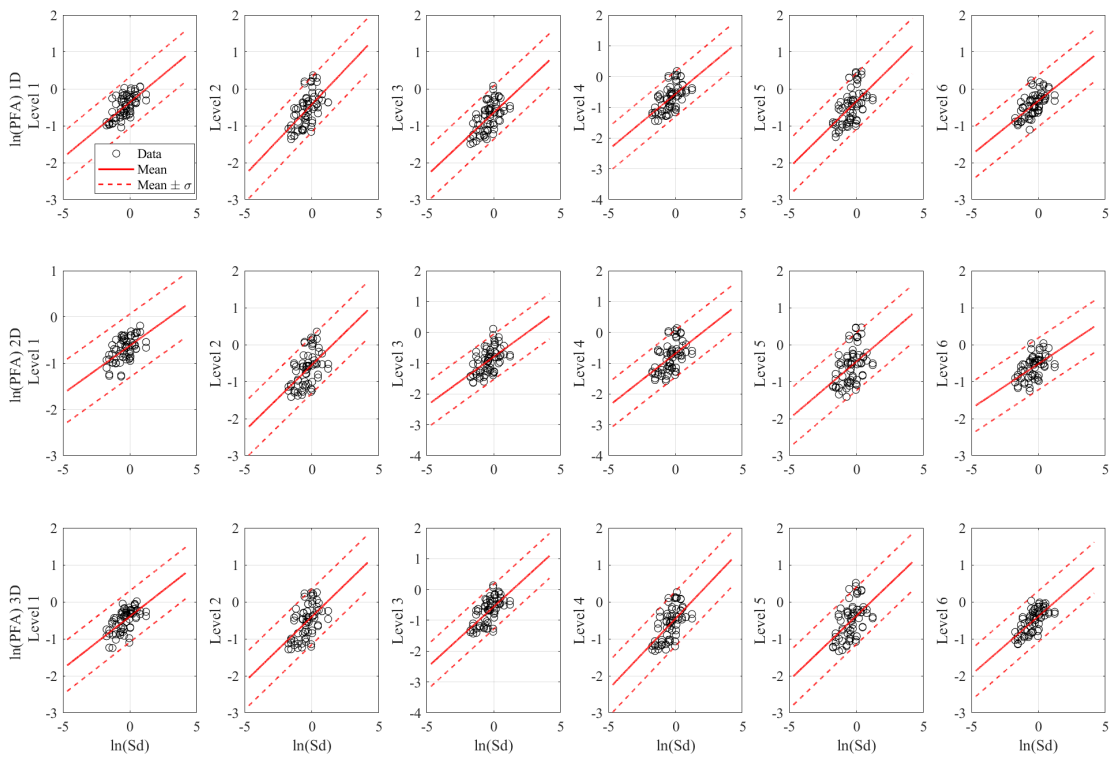


Figure E.2: Regression analyses of Sd v.s. PFA

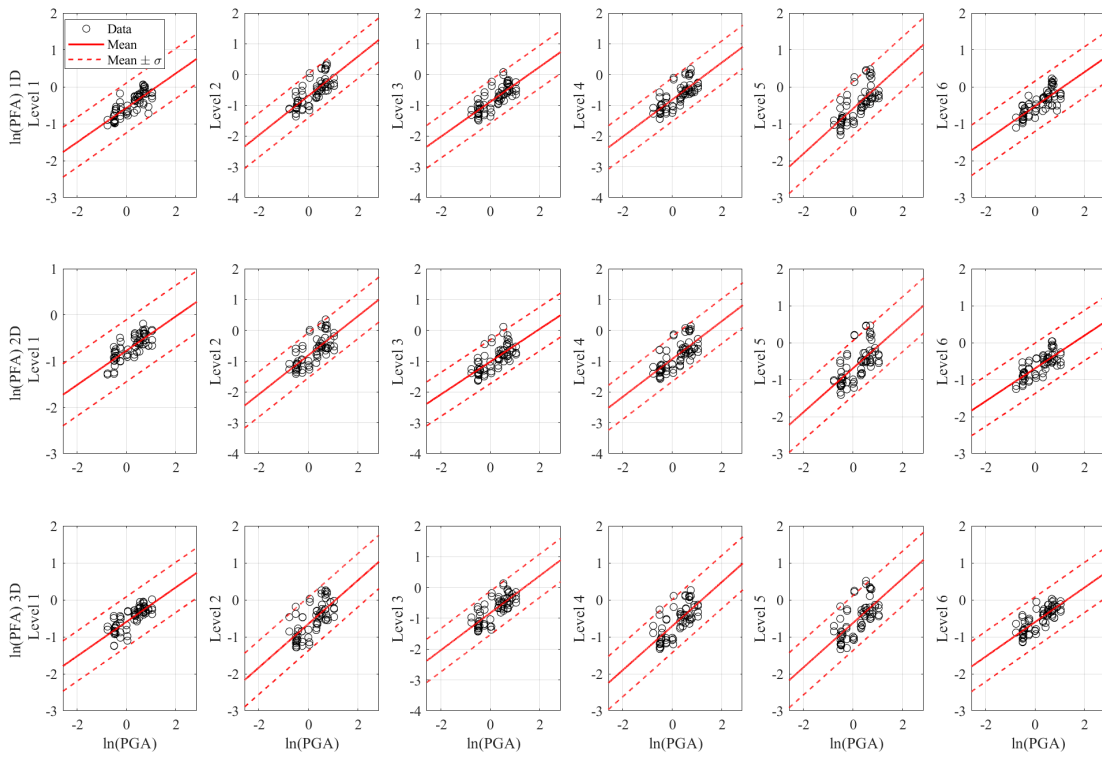


Figure E.3: Regression analyses of PGA v.s. PFA

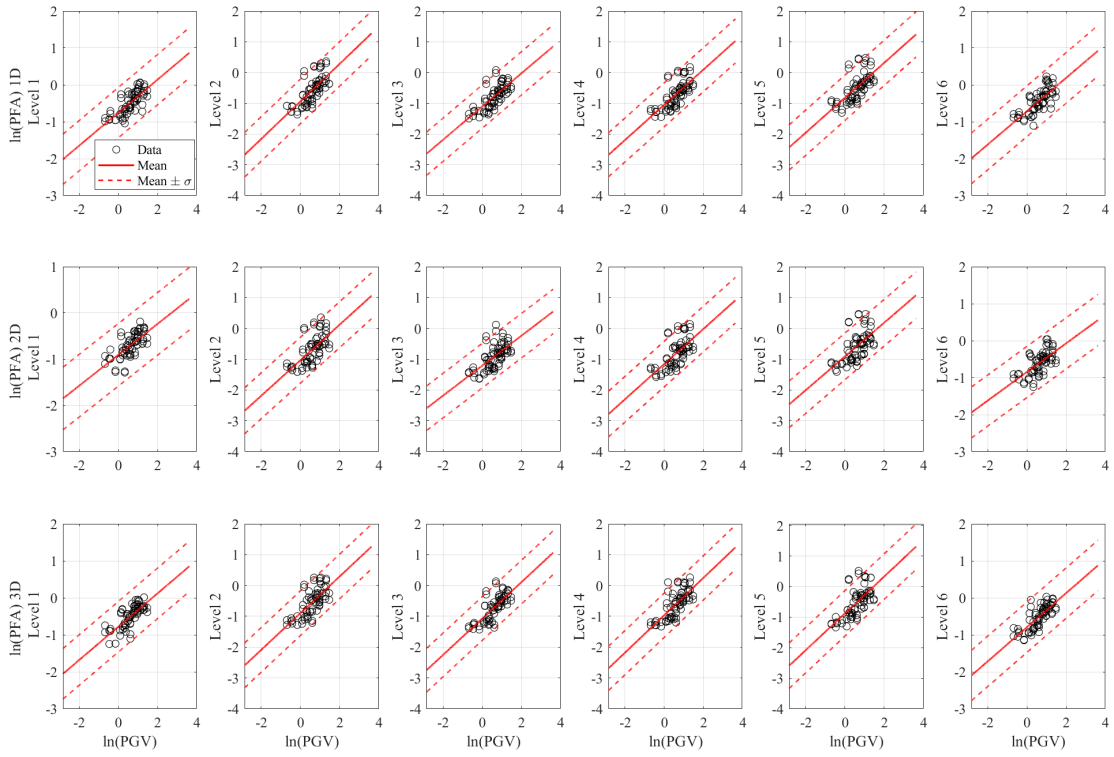


Figure E.4: Regression analyses of PGV v.s. PFA

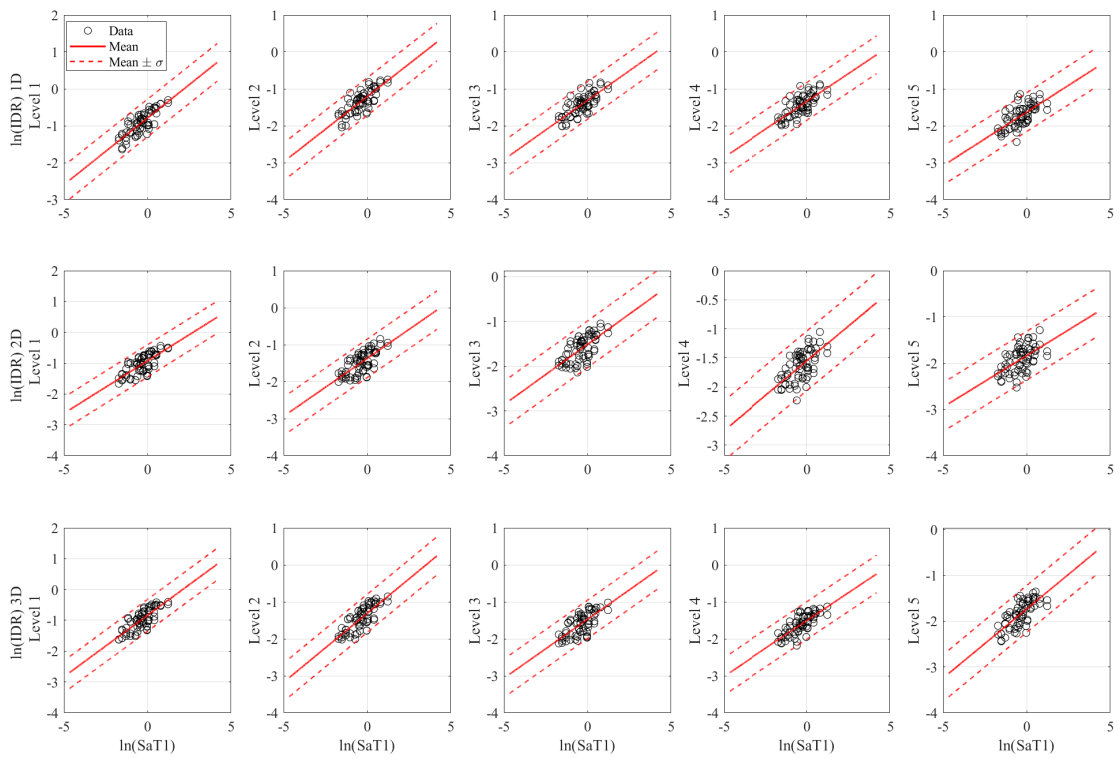


Figure E.5: Regression analyses of SaT1 v.s. IDR

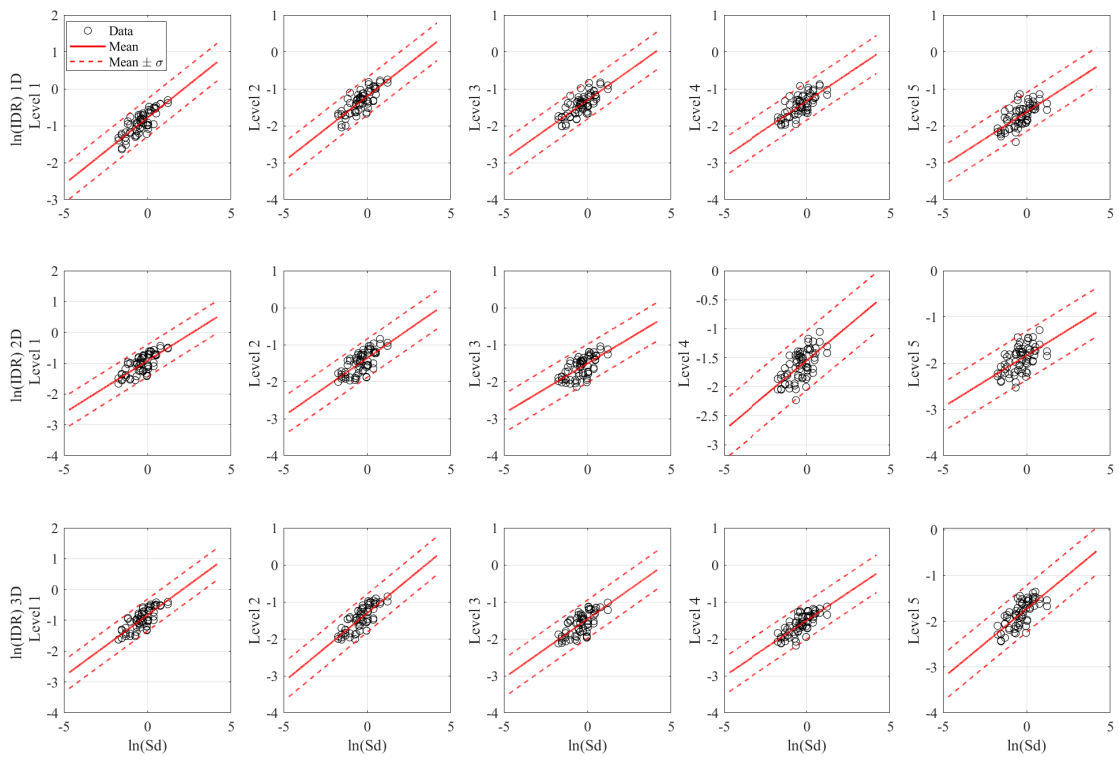


Figure E.6: Regression analyses of Sd v.s. IDR

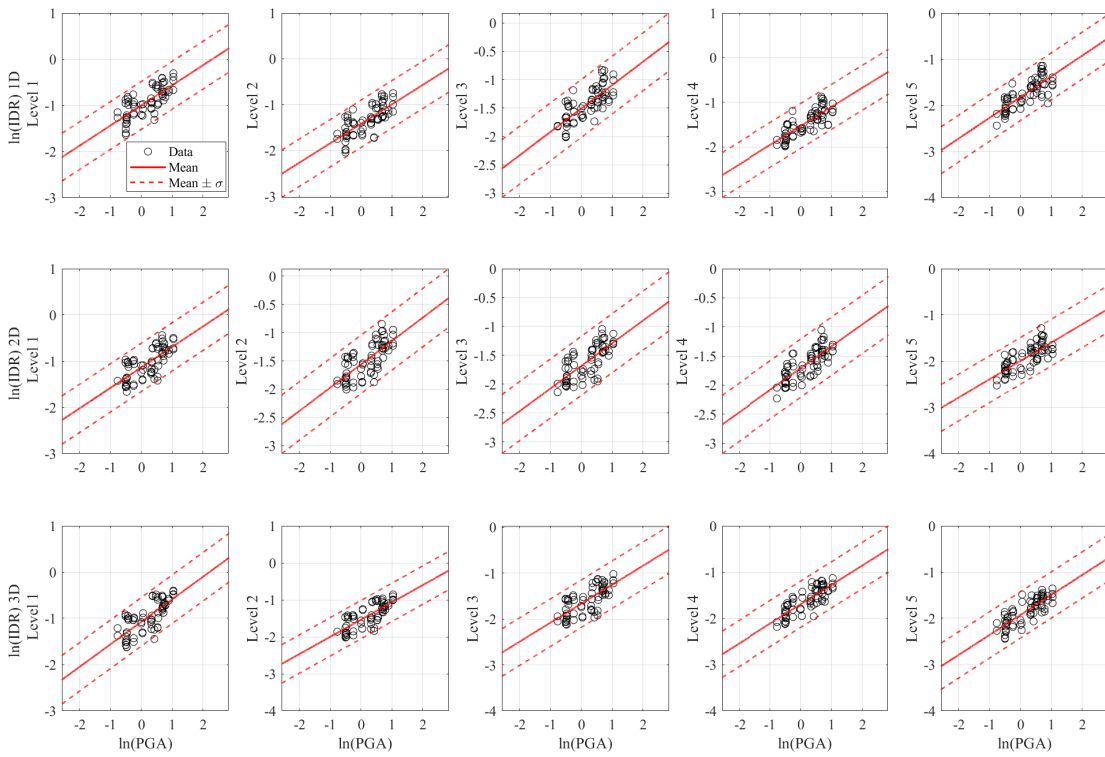


Figure E.7: Regression analyses of PGA v.s. IDR

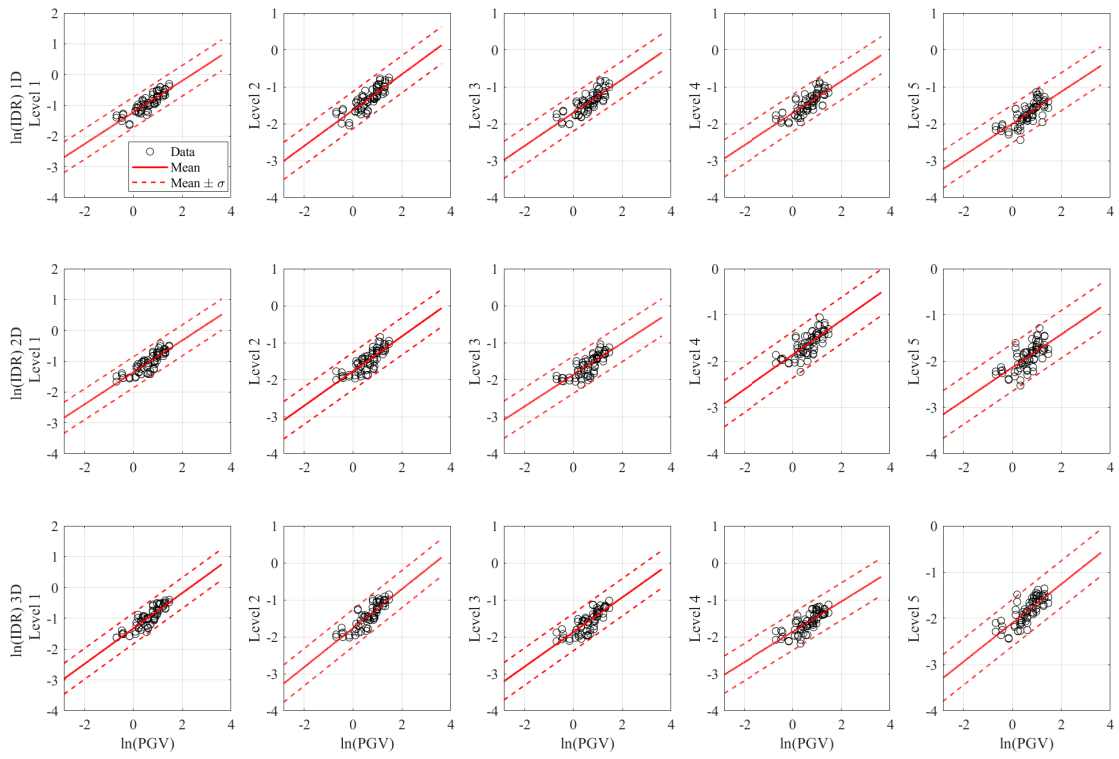


Figure E.8: Regression analyses of PGV v.s. IDR

REFERENCES

- [1] Adam Zsarnoczay, Frank McKenna, Charles Wang, Wael Elhaddad, Michael Gardner (2019, October 15). NHERI-SimCenter/PBE: Release v2.0.0. <http://doi.org/10.5281/zenodo.3491145>.
- [2] American Society of Civil Engineers. *Minimum Design Loads for Buildings and Other Structures*, 2016.
- [3] Jack W Baker and C Allin Cornell. Spectral shape, epsilon and record selection. *Earthquake Engineering & Structural Dynamics*, 35(9):1077–1095, 2006.
- [4] M Baradaran Shoraka and KJ Elwood. Mechanical model for non ductile reinforced concrete columns. *Journal of Earthquake Engineering*, 17(7):937–957, 2013.
- [5] Tracy C Becker and Stephen A Mahin. Experimental and analytical study of the bi-directional behavior of the triple friction pendulum isolator. *Earthquake Engineering & Structural Dynamics*, 41(3):355–373, 2012.
- [6] David M Boore, Jennie Watson-Lamprey, and Norman A Abrahamson. Orientation-independent measures of ground motion. *Bulletin of the seismological Society of America*, 96(4A):1502–1511, 2006.
- [7] Rubén Boroschek, Rodrigo Retamales, and WHO Collaborating Center. Base isolation in hospitals. In *Proceedings, Seminar on Design of Health Facilities to Resist Natural Hazards*, 2002.
- [8] R Bouc. Forced vibrations of mechanical systems with hysteresis. In *Proc. of the Fourth Conference on Nonlinear Oscillations, Prague, 1967*, 1967.
- [9] Yousef Bozorgnia and Kenneth W Campbell. The vertical-to-horizontal response spectral ratio and tentative procedures for developing simplified v/h and vertical design spectra. *Journal of Earthquake Engineering*, 8(02):175–207, 2004.
- [10] Brendon A Bradley. A critical examination of seismic response uncertainty analysis in earthquake engineering. *Earthquake engineering & structural dynamics*, 42(11):1717–1729, 2013.
- [11] Gian Michele Calvi, Paola Ceresa, Chiara Casarotti, Davide Bolognini, and Ferdinando Auricchio. Effects of axial force variation in the seismic response of bridges isolated with friction pendulum systems. *Journal of Earthquake Engineering*, 8(spec01):187–224, 2004.
- [12] Miguel Ángel Caminero and Francisco Javier Montáns. An enhanced algorithm for nested surfaces plasticity using the implicit mróz translation rule. *Computers & Structures*, 84(26-27):1684–1695, 2006.

- [13] Ozan Cem Celik and Bruce R Ellingwood. Seismic fragilities for non-ductile reinforced concrete frames—role of aleatoric and epistemic uncertainties. *Structural Safety*, 32(1):1–12, 2010.
- [14] Peng-Yu Chen. *A Data-Driven Framework for Regional Assessment of Seismically Vulnerable Buildings*. PhD thesis, UCLA, 2021.
- [15] Anil K Chopra. *Dynamics of structures*. Pearson Education India, 2007.
- [16] Woo-Jung Chung, Chung-Bang Yun, Nam-Sik Kim, and Ju-Won Seo. Shaking table and pseudodynamic tests for the evaluation of the seismic performance of base-isolated structures. *Engineering Structures*, 21(4):365–379, 1999.
- [17] CivilDigital. Elastomeric rubber bearings. <https://civildigital.com/base-isolation-system-outline-on-principles-types-advantages-applications/elastomeric-rubber-bearings/>, 2021. [Online; accessed 15-July-2021].
- [18] CivilDigital. Spring isolators. <https://civildigital.com/base-isolation-system-outline-on-principles-types-advantages-applications/spring-isolators/>, 2021. [Online; accessed 15-July-2021].
- [19] Michael C Constantinou and Ani Natali Sigaher. Energy dissipation system configurations for improved performance. In *Advanced Technology in Structural Engineering*, pages 1–8. Advanced Technology in Structural Engineering, 2000.
- [20] Michalakis Constantinou, Anoop Mokha, and Andrei Reinhorn. Teflon bearings in base isolation ii: Modeling. *Journal of Structural Engineering*, 116(2):455–474, 1990.
- [21] C Allin Cornell, Fatemeh Jalayer, Ronald O Hamburger, and Douglas A Foutch. Probabilistic basis for 2000 sac federal emergency management agency steel moment frame guidelines. *Journal of structural engineering*, 128(4):526–533, 2002.
- [22] Nhan D Dao. *Seismic response of a full-scale 5-story steel frame building isolated by triple pendulum bearings under 3D excitations*. PhD thesis, University of Nevada, Reno, 2012.
- [23] Nhan D Dao, Keri L Ryan, Eiji Sato, and Tomohiro Sasaki. Predicting the displacement of triple pendulum™ bearings in a full-scale shaking experiment using a three-dimensional element. *Earthquake Engineering & Structural Dynamics*, 42(11):1677–1695, 2013.
- [24] Matjaz Dolsek. Incremental dynamic analysis with consideration of modeling uncertainties. *Earthquake Engineering & Structural Dynamics*, 38(6):805–825, 2009.
- [25] Paul L. Drazin and Sanjay Govindjee. A nonlinear kinetic model for multi-stage friction pendulum systems. PEER Report No. 2017/07, Department of Civil and Environmental Engineering, University of California, Berkeley, 2017.

- [26] Murat Eröz and Reginald DesRoches. Bridge seismic response as a function of the friction pendulum system (fps) modeling assumptions. *Engineering Structures*, 30(11):3204–3212, 2008.
- [27] Daniel M Fenz and Michael C Constantinou. Spherical sliding isolation bearings with adaptive behavior: Experimental verification. *Earthquake engineering & structural dynamics*, 37(2):185–205, 2008.
- [28] G Fernández-Dávila and Cominetti CC VI. S., cruz z., ef (2000) considering the bi-directional effects and the seismic angle variations in building design. In *12th World Conference in Earthquake Engineering, Auckland, New Zealand. January, 2000*.
- [29] Paolo Gardoni, Khalid M Mosalam, and Armen Der Kiureghian. Probabilistic seismic demand models and fragility estimates for rc bridges. *Journal of earthquake engineering*, 7(spec01):79–106, 2003.
- [30] GR Gillich, V Iancu, N Gillich, ZI Korca, CP Chioncel, and C Hatiegan. Decoupling the structure from the ground motion during earthquakes by employing friction pendulums. In *IOP Conference Series: Materials Science and Engineering*, volume 294, page 012025. IOP Publishing, 2018.
- [31] Damian N Grant, Diego Padilla, and Paul D Greening. Orientation dependence of earthquake ground motion and structural response. In *Protection of Built Environment Against Earthquakes*, pages 57–73. Springer, 2011.
- [32] Norman B Green. Flexible first-story construction for earthquake resistance. *Transactions of the American Society of Civil Engineers*, 100(1):645–652, 1935.
- [33] Jean C Guzman Pujols and Keri L Ryan. Computational simulation of slab vibration and horizontal-vertical coupling in a full-scale test bed subjected to 3d shaking at e-defense. *Earthquake Engineering & Structural Dynamics*, 47(2):438–459, 2018.
- [34] Hazus-MH FEMA. *Multi-hazard loss estimation methodology earthquake model*, 2003.
- [35] HP Hong and K Goda. Orientation-dependent ground-motion measure for seismic-hazard assessment. *Bulletin of the Seismological Society of America*, 97(5):1525–1538, 2007.
- [36] Lydik S Jacobsen and Robert S Ayre. Experimentally determined dynamic shears in a sixteen-story model. *Bulletin of the seismological society of America*, 28(4):269–311, 1938.
- [37] Nirmal Jayaram, Ting Lin, and Jack W Baker. A computationally efficient ground-motion selection algorithm for matching a target response spectrum mean and variance. *Earthquake Spectra*, 27(3):797–815, 2011.

- [38] Jong-Su Jeon, Laura N Lowes, Reginald DesRoches, and Ioannis Brilakis. Fragility curves for non-ductile reinforced concrete frames that exhibit different component response mechanisms. *Engineering Structures*, 85:127–143, 2015.
- [39] Lee H Johnson, Edward J Bednarski, Merit P White, Paul L Kartzke, Howard G Smits, and HA Williams. Discussion of “johnson on flexible first-story construction”. *Transactions of the American Society of Civil Engineers*, 100(1):653–669, 1935.
- [40] Andreas J Kappos, Georgios Panagopoulos, Christos Panagiotopoulos, and Gregorios Penelis. A hybrid method for the vulnerability assessment of r/c and urm buildings. *Bulletin of Earthquake Engineering*, 4(4):391–413, 2006.
- [41] James M Kelly and Karl E Beucke. A friction damped base isolation system with fail-safe characteristics. *Earthquake Engineering & Structural Dynamics*, 11(1):33–56, 1983.
- [42] Jalal Kiani and Mohammad Khanmohammadi. New approach for selection of real input ground motion records for incremental dynamic analysis (ida). *Journal of Earthquake Engineering*, 19(4):592–623, 2015.
- [43] Manish Kumar, Andrew S Whittaker, and Michael C Constantinou. Characterizing friction in sliding isolation bearings. *Earthquake Engineering & Structural Dynamics*, 44(9):1409–1425, 2015.
- [44] Gang Li, Di-xiong Yang, and Geng-dong Cheng. Performance-based dynamic optimum design for isolated structures. *JOURNAL-DALIAN UNIVERSITY OF TECHNOLOGY*, 46(2):160, 2006.
- [45] BC Lin and I Tadjbakhsh. Effect of vertical motion on friction-driven isolation systems. *Earthquake engineering & structural dynamics*, 14(4):609–622, 1986.
- [46] Ting Lin and Jack W Baker. Introducing adaptive incremental dynamic analysis: a new tool for linking ground motion selection and structural response assessment. In *Proceedings, 11th International Conference on Structural Safety and Reliability*, 2013.
- [47] Nicolas Luco and C. Allin Cornell. Structure-specific scalar intensity measures for near-source and ordinary earthquake ground motions. *Earthquake Spectra*, 23(2):357–392, 2007.
- [48] Kevin Mackie and Božidar Stojadinović. Probabilistic seismic demand model for california highway bridges. *Journal of Bridge Engineering*, 6(6):468–481, 2001.
- [49] H Mao, H Darama, and E Taciroglu. A consistent omnidirectional nonlinear hysteretic response model for triple friction pendulum bearings. In *Proceedings of the 17th World Conference on Earthquake Engineering*, Sendai International Center, Sendai, Japan, 2020.

- [50] H Mao, Z Ni, H Darama, and E Taciroglu. Consistent omnidirectional extension of uniaxial nonlinear hysteretic response models. In *Proceedings of the 11th National Conference on Earthquake Engineering*, Sendai International Center, Los Angeles, California, 2018.
- [51] Julius Marko, David Thambiratnam, and Nimal Perera. Influence of damping systems on building structures subject to seismic effects. *Engineering Structures*, 26(13):1939–1956, 2004.
- [52] RR Martel. The effects of earthquakes on buildings with a flexible first story. *Bulletin of the Seismological Society of America*, 19(3):167–178, 1929.
- [53] Frank McKenna. Opensees: a framework for earthquake engineering simulation. *Computing in Science & Engineering*, 13(4):58–66, 2011.
- [54] Francisco J Montáns and Ronaldo I Borja. Implicit j2-bounding surface plasticity using prager’s translation rule. *International journal for numerical methods in engineering*, 55(10):1129–1166, 2002.
- [55] Francisco J Montáns and Miguel A Caminero. On the consistency of nested surfaces models and their kinematic hardening rules. *International journal of solids and structures*, 44(14-15):5027–5042, 2007.
- [56] Francisco-Javier Montáns. Implicit algorithms for multilayer j2-plasticity. *Computer methods in applied mechanics and engineering*, 189(2):673–700, 2000.
- [57] Francisco Javier Montáns. Implicit multilayer j2-plasticity using prager’s translation rule. *International Journal for Numerical Methods in Engineering*, 50(2):347–375, 2001.
- [58] Giorgio Monti and Floriana Petrone. Analytical thermo-mechanics 3d model of friction pendulum bearings. *Earthquake Engineering & Structural Dynamics*, 45(6):957–977, 2016.
- [59] Troy A Morgan and Stephen A Mahin. The optimization of multi-stage friction pendulum isolators for loss mitigation considering a range of seismic hazard. In *The 14th World Conference on Earthquake Engineering*, pages 11–0070. Citeseer, 2008.
- [60] Troy A Morgan and Stephen A Mahin. Performance-based design of seismic isolated buildings considering multiple performance objectives. *Smart Struct. Syst*, 4(5):655–666, 2008.
- [61] Troy A Morgan and Stephen A Mahin. Achieving reliable seismic performance enhancement using multi-stage friction pendulum isolators. *Earthquake Engineering & Structural Dynamics*, 39(13):1443–1461, 2010.

- [62] Gilberto Mosqueda, Andrew S Whittaker, and Gregory L Fenves. Characterization and modeling of friction pendulum bearings subjected to multiple components of excitation. *Journal of Structural Engineering*, 130(3):433–442, 2004.
- [63] Zi Mroz. On the description of anisotropic workhardening. *Journal of the Mechanics and Physics of Solids*, 15(3):163–175, 1967.
- [64] AM Nacamuli. Seismic protection of data centers using ball-n-cone base isolation. In *Structures Congress 2012*, pages 1373–1384, 2012.
- [65] University of Southern California. Keck hospital of usc. <https://www.keckmedicine.org/>, 2021. [Online; accessed 15-July-2021].
- [66] VR Panchal, RS Jangid, DP Soni, and BB Mistry. Response of the double variable frequency pendulum isolator under triaxial ground excitations. *Journal of Earthquake Engineering*, 14(4):527–558, 2010.
- [67] YJ Park, YK Wen, and A H-S Ang. Random vibration of hysteretic systems under bi-directional ground motions. *Earthquake engineering & structural dynamics*, 14(4):543–557, 1986.
- [68] Peer. Peer strong motion database, 2011.
- [69] A. L. K. Penkuhn. Three point foundation for building structures, 1967. US Patent No. 3347002.
- [70] Montazar Rabiei and Faramarz Khoshnoudian. Response of multistory friction pendulum base-isolated buildings including the vertical component of earthquakes. *Canadian Journal of Civil Engineering*, 38(10):1045–1059, 2011.
- [71] Pathmanathan Rajeev and S Tesfamariam. Seismic fragilities of non-ductile reinforced concrete frames with consideration of soil structure interaction. *Soil Dynamics and Earthquake Engineering*, 40:78–86, 2012.
- [72] Juan C Reyes and Erol Kalkan. Significance of rotating ground motions on nonlinear behavior of symmetric and asymmetric buildings in near fault sites. In *Proceedings of the 9th International Conference on Urban Earthquake Engineering/4th Asia Conference on Earthquake Engineering*, pages 6–8, 2012.
- [73] Antonio B Rigato and Ricardo A Medina. Influence of angle of incidence on seismic demands for inelastic single-storey structures subjected to bi-directional ground motions. *Engineering Structures*, 29(10):2593–2601, 2007.
- [74] Keri L Ryan and Nhan D Dao. Influence of vertical ground shaking on horizontal response of seismically isolated buildings with friction bearings. *Journal of Structural Engineering*, 142(1):04015089, 2016.

- [75] Fahim Sadek, Fahim Sadek, Andrew W Taylor, and Riley M Chung. *Passive energy dissipation devices for seismic applications*. US Department of Commerce, National Institute of Standards and Technology, 1996.
- [76] Apostolos A Sarlis, Dharma Theja R Pasala, MC Constantinou, AM Reinhorn, Satish Nagarajaiah, and DP Taylor. Negative stiffness device for seismic protection of structures. *Journal of Structural Engineering*, 139(7):1124–1133, 2013.
- [77] Tomohiro Sasaki, Eiji Sato, Keri L Ryan, Taichiro Okazaki, Stephen A Mahin, and Koichi Kajiwara. Nees/e-defense base-isolation tests: effectiveness of friction pendulum and lead-rubber bearing systems. In *Proceedings of the 15th World Conference of Earthquake Engineering*, 2012.
- [78] H Shakib and A Fuladgar. Effect of vertical component of earthquake on the response of pure-friction base-isolated asymmetric buildings. *Engineering structures*, 25(14):1841–1850, 2003.
- [79] Benshun Shao and Stephen A Mahin. A probabilistic design method to achieve targeted levels of reliability for seismically isolated structures. *Earthquake Spectra*, 36(2):741–766, 2020.
- [80] Masanobu Shinozuka, Stephanie E Chang, Ronald T Eguchi, Daniel P Abrams, Howard HM Hwang, and Adam Rose. Advances in earthquake loss estimation and application to memphis, tennessee. *Earthquake Spectra*, 13(4):739–758, 1997.
- [81] Nilesh Shome. *Probabilistic seismic demand analysis of nonlinear structures*. Stanford University, 1999.
- [82] Juan C Simo and Thomas JR Hughes. *Computational inelasticity*, volume 7. Springer Science & Business Media, 2006.
- [83] RI Skinner. Base isolation provides a large building with increased earthquake resistance: Development, design and construction. In *Proceedings of the International Conference on Natural Rubber Fr Earthquake Protection of Buildings and Vibration Isolation*, 1982.
- [84] RI Skinner, GN Bycroft, and GH McVerry. A practical system for isolating nuclear power plants from earthquake attack. *Nuclear Engineering and Design*, 36(2):287–297, 1976.
- [85] RI Skinner and GH McVerry. Base isolation for increased earthquake resistance of buildings. *Bulletin of the New Zealand Society for Earthquake Engineering*, 8(2):93–101, 1975.

- [86] Michael D Symans and Michael C Constantinou. Semi-active control systems for seismic protection of structures: a state-of-the-art review. *Engineering structures*, 21(6):469–487, 1999.
- [87] Dassault Systèmes. *ABAQUS*. Cambridge, MA, 1985.
- [88] Earthquake Protection Systems. Earthquake protection systems (eps) qualifications. <http://www.ci.vallejo.ca.us/common/pages/DisplayFile.aspx?itemId=120632>, 10 2014. [Online; accessed 15-July-2021].
- [89] Earthquake Protection Systems. Friction pendulum bearings. <https://www.earthquakeprotection.com/products>, 2020. [Online; accessed 15-July-2021].
- [90] Andrew Tarantola. How buildings stay up when the earth shakes. <https://www.gizmodo.com.au/2011/08/how-buildings-stay-up-when-the-earth-shakes/>, 8 2011. [Online; accessed 10-July-2021].
- [91] P Tomek, H Darama, R Sturt, and Y Huang. Modelling rim impact and ultimate behaviour of triple friction pendulum bearings. In *Proceedings of the 17th World Conference on Earthquake Engineering*, Sendai International Center, Sendai, Japan, 2020.
- [92] Dimitrios Vamvatsikos. *Seismic performance, capacity and reliability of structures as seen through incremental dynamic analysis*. Stanford University, 2002.
- [93] Dimitrios Vamvatsikos and C Allin Cornell. Incremental dynamic analysis. *Earthquake engineering & structural dynamics*, 31(3):491–514, 2002.
- [94] Dimitrios Vamvatsikos and C Allin Cornell. Applied incremental dynamic analysis. *Earthquake spectra*, 20(2):523–553, 2004.
- [95] Dimitrios Vamvatsikos and Michalis Fragiadakis. Incremental dynamic analysis for estimating seismic performance sensitivity and uncertainty. *Earthquake engineering & structural dynamics*, 39(2):141–163, 2010.
- [96] D Veneziano, JM Sussman, U Gupta, and SM Kunnumkal. Earthquake loss under limited transportation capacity: Assessment, sensitivity and remediation. In *Proceedings of the Seventh US National Conference on Earthquake Engineering, Boston, USA (on CD)*, 2002.
- [97] Gordon P Warn and Keri L Ryan. A review of seismic isolation for buildings: historical development and research needs. *Buildings*, 2(3):300–325, 2012.
- [98] Yi-Kwei Wen. Method for random vibration of hysteretic systems. *Journal of the engineering mechanics division*, 102(2):249–263, 1976.

- [99] Yazhou Xie and Jian Zhang. Evaluating the effectiveness and optimal design of isolation bearings and fluid dampers for a highway bridge using a fragility function method and genetic optimization. In *Geotechnical and Structural Engineering Congress 2016*, pages 1317–1330, 2016.
- [100] Yazhou Xie and Jian Zhang. Design and optimization of seismic isolation and damping devices for highway bridges based on probabilistic repair cost ratio. *Journal of Structural Engineering*, 144(8):04018125, 2018.
- [101] Mahin Zayas. Continued functionality standard seismic isolator standard. <https://www.earthquakeprotection.com/standards>, 2 2021. [Online; accessed 15-July-2021].
- [102] VA Zayas, SS Low, and SA Mahin. The fps earthquake resisting system. experimental report no. ucb/eerc 87/01, eerc. *University of California, Berkeley*, 1987.
- [103] J Zhang and Y Huo. Optimum isolation design for highway bridges using fragility function method. In *The 14th World Conference on Earthquake Engineering (WCEE), Beijing, China: hlm.-, Oktober 12*, volume 17, page 2008, 2008.
- [104] Jian Zhang and Yili Huo. Evaluating effectiveness and optimum design of isolation devices for highway bridges using the fragility function method. *Engineering Structures*, 31(8):1648–1660, 2009.
- [105] W Zhang, M Shokrabadi, Y Bozorgnia, and E Taciroglu. A methodology for fragility analysis of buried water pipes considering coupled horizontal and vertical ground motions. *Computers and Geotechnics*, 126:103709, 2020.
- [106] Shuang Zou, Wenliuhan Heisha, and Ping Tan. Performance-based dynamic optimal design for isolated structures with multiple-coupling friction dampers. *Advances in Structural Engineering*, 23(10):2149–2162, 2020.